AN INVESTIGATION INTO THE PERFORMANCE OF A FLUX CONCENTRATION
MAGNETIC GEARBOX AND MAGNETICALLY GEARED MOTORS

by

Debarupa Som

A dissertation submitted to the faculty of
The University of North Carolina at Charlotte
in partial fulfillment of the requirements
for the degree of Doctor of Philosophy in
Electrical Engineering

Charlotte

2020

Approved by:

_____
Dr. Jonathan Z. Bird

_____
Dr. Madhav Manjrekar

_____
Dr. Valentina Cecchi

_____
Dr. Wesley B. Williams

ABSTRACT

DEBARUPA SOM. An investigation into the performance of flux concentration magnetic gearbox and magnetically geared motors
(Under the direction of DR. JONATHAN Z. BIRD)

In today's world, renewable energy sources like wind and ocean energy have come more into prominence as a source of sustainable energy. The energy conversion devices used in these cases, utilize mechanical gearboxes to match the speed of the input shaft to that of the electromagnetic generators. The mechanical gearbox however, has certain disadvantages such as wear and tear, vibration and noise, need for lubrication and no overload protection. In order to mitigate these issues, direct drive generators were used wherein, the gearboxes were removed and the input shaft was directly connected to the synchronous generators. If the input speed on the generator shaft is low, a high torque would be required to generate the power. To generate this high torque, the synchronous generator should be of significantly larger in size. An alternative approach is to replace mechanical gearboxes with magnetic gears. The magnetic gears being contactless mechanisms reduce wear and tear, vibration and require less maintenance. They also have inherent overload protection which makes them highly reliable. However, when compared to its mechanical counterparts, magnetic gears have low torque densities. Although significant progress has been made to improve the torque densities, the torque densities achieved in magnetic gears are quite low compared to mechanical gears.

This research is focused on studying and comparing different typologies of coaxial magnetic gears designed to enhance the torque densities. Three main typologies - the idealized design with the cage rotor between the inner and the outer rotor, an outer cage rotor design and a design with consequent poles on the outer rotor were studied. A

parametric sweep analysis of the geometric parameters was conducted to maximize the volumetric torque densities in each case. This was done using finite element analysis. The highest torque density of about 336 Nm/L is obtained with the idealized design and was considered for further designing magnetically geared motors.

A magnetic gear with flux concentration Halbach rotor was designed, simulated and experimentally tested. The design used ferromagnetic pole pieces acting as retaining sleeves to hold the radially directed magnets. The design produced a torque density of 185 Nm/L when simulated using 2D finite element analysis. However, owing to the complicated assembly process, a measured torque density of 112 Nm/L is obtained when tested experimentally.

A Magnetically geared motor achieved by integrating a magnetic gear with an electrical machine was analyzed. At first an internal stator machine was studied with both integral slot and fractional slot winding designs. Halbach magnets were used to increase the torque densities of these machines. However, torque ripple generated was quite high making these machines less viable. In order to reduce the torque ripple, a two layer winding distribution approach with each phase winding shifted by one slot was considered. This approach however reduced the torque density of the machine.

An outer stator magnetically geared motor with integral slot winding design has also been studied. Two different cage rotor designs – the rectangular modulator lamination supports with bridge connection and circular modulator lamination support were analyzed and simulated using 2D finite element analysis method. Both the designs used Halbach magnets on the inner and outer rotor. The machine designs were conceived to achieve a zero torque on the inner rotor. The design with rectangular cage rotor produced a torque density of 130 Nm/L with considerably low torque ripple values of

about 1% of the steady state value whereas, the other design with circular cage rotor produced a torque density of 117 Nm/L and a torque ripple of about 2% of the steady state value.

ACKNOWLEDGEMENTS

TABLE OF CONTENTS

LIST OF FIGURES

LIST OF TABLES

LIST OF ABBREVIATIONS

MHK	Marine Hydro Kinetic
DD	Direct Drive
SG	Synchronous Generator
PM	Permanent Magnet
MG	Magnetic Gear
MGM	Magnetically Geared Motor
CVMG	Continuously Variable Magnetic Gear
FEA	Finite Element Analysis
PMBLDC	Permanent Magnet Brushless DC
MPG-PMBL	Magnetic Planetary Gear Permanent Magnet Brushless
CVT	Continuous Variable Transmission
MIPG	Motor Integrated Permanent Magnetic Gear
FM	Flux Modulated
MGIS	Magnetically Geared Inner Stator
MGOS	Magnetically Geared Outer Stator
FS	Fractional Slot
HS	High Speed
LS	Low Speed

1 LITERATURE REVIEW AND INTRODUCTION

1.1 Introduction

The world's increasing human population, along with rapid industrialization, has led to serious environmental effect like climate change. In order to reduce the impact of climate change, most countries are increasing their use of clean and sustainable energy. Renewable energy provides alternative sources for power generation and may emerge as the only option for achieving a sustainable energy supply in the future. Energy sources like wind is among the fastest growing renewable energy technologies worldwide [1]. Typically in a wind turbine, power generated from the rotation of the turbine rotor is transferred to the generator via a main shaft and a mechanical gearbox; such a configuration is shown in Figure 1-1. The mechanical gearbox is used to increase the speed and decrease the torque from the input shaft to enable power to be economically generated.
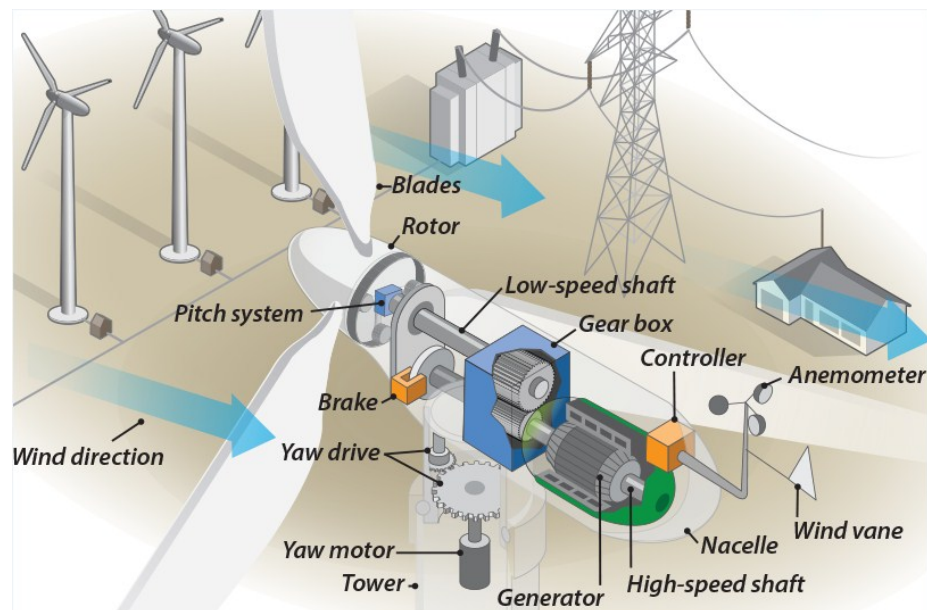
Figure 1-1: Typical wind turbine configuration [2]

However, the mechanical gearbox has certain disadvantages. For instance, the load applied to the gearbox [3] changes frequently when the wind speed changes. This creates a lot of stress on the gearbox teeth and can result in the failure of the mechanical gearbox [4]. It was reported in [5] that gearboxes designed to last for 20 years were failing after only 12 years. The frequent failures of the wind turbine mechanical gearbox increases the maintenance cost, thereby increasing the levelized cost of power generation.

In order improve the reliability of the wind turbines, an alternate technology in use is the direct drive (DD) generator technology, in which the gearbox is removed and the shaft of the wind turbine is directly connected to the synchronous generator (SG). The rotor of the SG can be either electrically excited or be composed of permanent magnets (PM). A PM direct-drive wind turbine generator is shown in Figure 1-2. Since the input speed to the generator fed from the wind turbine blades is low, the torque must be high in order to generate the required power [6]. Since traditional electrical machines have very low torque density relative to mechanical gearboxes, the DD generator must be larger in size; furthermore since the generator is directly connected to the shaft, a converter has to
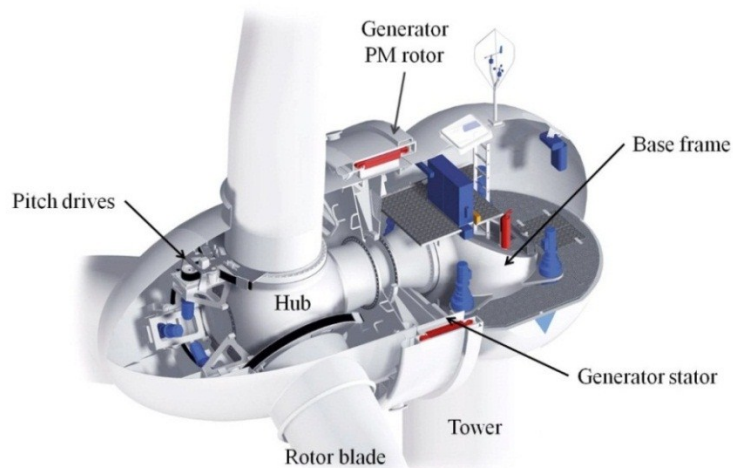
Figure 1-2: Direct-drive generator by Goldwind, China [7]

be designed for full rated power and hence the power electronics will be relatively costly [2]. To reliably convert the low speed motion from renewable energy devices into high speed rotation suitable for power generation, a contactless magnetic gearing (MG) mechanism could be employed. MGs offer many potential advantages over their mechanical geared counterpart. A MG can create torque-speed change without any physical contact and therefore produces no wear and tear and could operate with less vibration. This reduces the maintenance costs compared to mechanical gearboxes. MGs also provide inherent overload protection. This makes the MG potentially highly valuable for wind turbine applications. However, due to the relative complexity of the MG and the shortcomings of earlier PMs, not much attention has been paid to investigating the MG's performance until the turn of the 21st century. With the discovery of new PM materials with high energy densities it has become possible to obtain higher torque densities [8]. Magnetically geared machines (MGMs) have been designed in which a concentric MG is integrated with an electrical machine. Such an approach enables generators to be designed with a significantly higher torque density than conventional machines.

1.2   Literature Review

MGMs as shown in Figure 1-3 are a new class of machines wherein a conventional PM machine is integrated with an MG [9-11]. MGMs offer reduced size and weight compared to DD generators. However, unlike DD machines, they require an additional rotor. The generator and the gear can be combined axially, i.e., they can be coupled on the same shaft or radially [12]. The two radial designs that have received the greatest attention are machines with the stator fitted on the inside of the MG as shown in Figure 1-3(a) and machines with the stator replacing the outer back iron yoke as shown in Figure 1-3(b). MGMs have been studied for use in wind power generators [4, 5, 13],

traction motors [11, 14], marine propulsion systems [15] and for many other industrial applications [8-10, 16, 17]. The following section presents a literature review of several different types of MGM, their different proposed applications and performance potentials.

1.2.1 Magnetically Geared Machine Designs with Outer Rotor Stator

In 2008, Atallah, *et al.* designed and built a coupled outer stator MGM they called a pseudo direct-drive machine [9]. Figure 1-3(b) shows the MGM and Figure 1-4 shows the built prototype and its cross section assembly design. The high speed rotor had $p_1 = 2$ pole pairs and the low speed rotor had $n_2 = 23$ ferromagnetic pole pieces. The stationary outer rotor had $p_3 = 21$ pole pieces. The gear ratio of the MG was 11.25. Atallah showed that with a significantly lower than normal rated current density of 2 A_{rms}/mm^2, a torque density in excess of 60 Nm/L could be achieved from the naturally air cooled machine, while the power factor was in excess of 0.9.
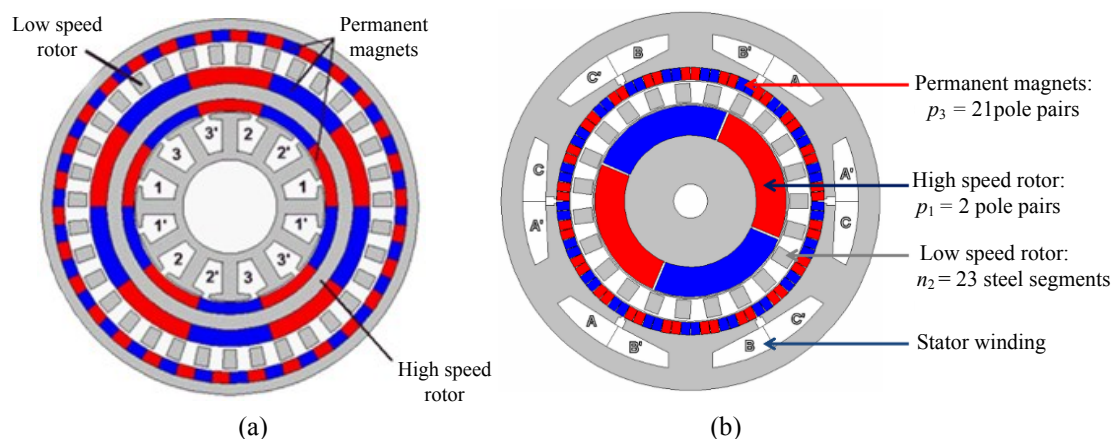
(a)   (b)
Figure 1-3: Topology of a MGM (a) coupled inner stator [18] and (b) coupled outer stator [9]
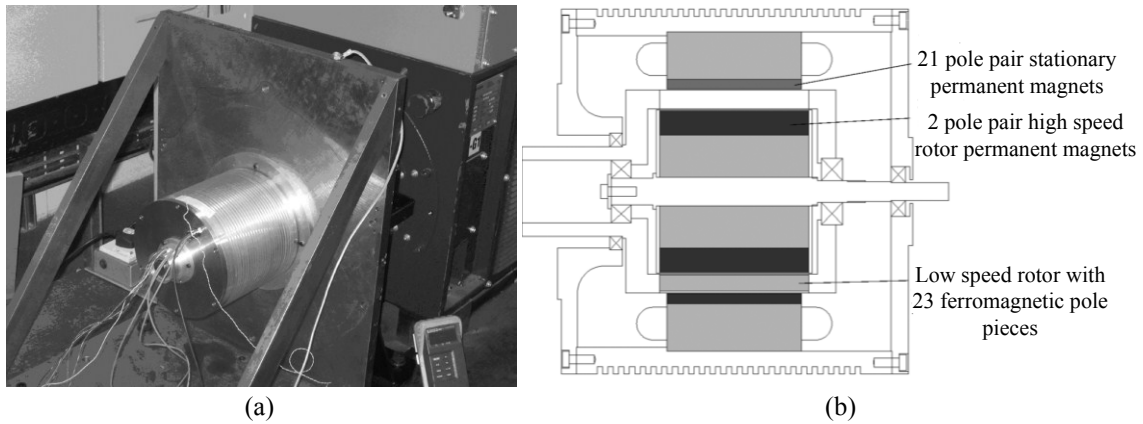
(a) (b)
Figure 1-4.(a) Pseudo direct drive machine on test bed and (b) Axial cross section of a pseudo direct drive machine [9]

The active diameter of the machine was 178 mm and the maximum torque generated by the MGM was limited by the maximum transmission torque between the MG rotors. The MGM proposed by Atallah as shown in Figure 1-3(b) had permanent magnets attached to the tip of the stator which increased the effective air gap flux path for the stator.

Niguchi and Hirata tried to improve the torque density by proposing a new outer stator MGM design in 2013, shown in Figure 1-5. In this design, the permanent magnets were moved from the tip of the stator into the stator slots, as shown in Figure 1-5(a). The number of permanent magnets in the high speed rotor could also be reduced by using a consequent pole high speed rotor, as shown in Figure 1-5(b). The calculated torque densities for the designs, shown in Figure 1-5(a) and Figure 1-5(b), were 63 Nm/L and 56.36 Nm/L respectively. The active diameters of the designs were 80 mm.

In 2014, an MGM proposed by Morimoto et al. [19] used a dual stator winding. The proposed MGM is shown in Figure 1-6. The MGM had a gear ratio of 3.4:1 with the number of pole pairs, $p_1 = 5$ on the high speed rotor, $n_2 = 17$ steel pieces on the low speed rotor and 12 stator slots with $p_3 = 6$ pairs of permanent magnets between the teeth. The
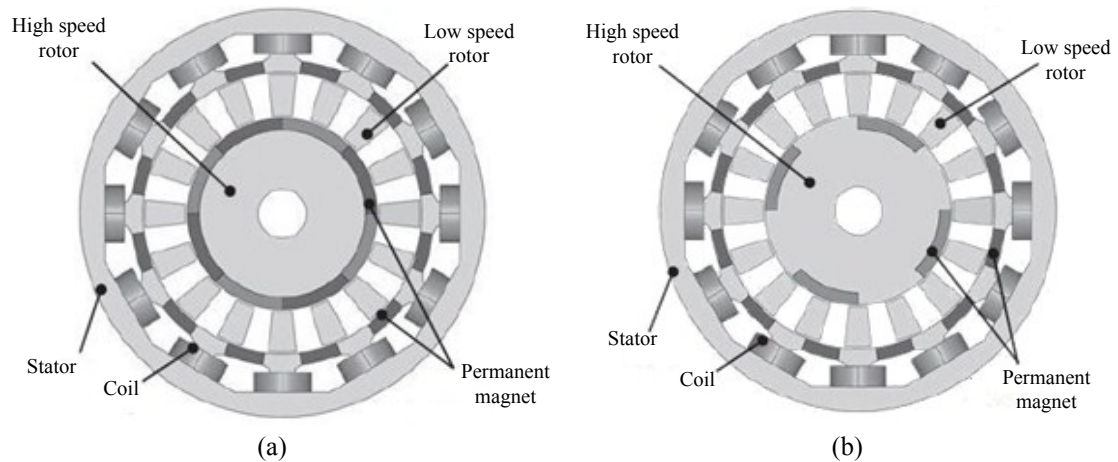
Figure 1-5. Magnetic geared motor (a) with permanent magnets on stator slots,(b)with reduced permanent magnets on high speed rotor [20]

three phase concentrated armature and field windings were actively wound around the same teeth; such a design is shown in Figure 1-6. Morimoto showed that by adding an additional field winding into the stator, the maximum transmission torque could be increased or decreased. Figure 1-7 shows the maximum transmission torque and torque constant variation with field current. The maximum transmission torque without field current is 45.1 Nm giving a torque density of 39.5 Nm/L and that with a field current of 100 A is 59 Nm producing a torque density of 51.7 Nm/L at a diameter of 220 mm. This machine can be used in cases where instantaneous torque, larger than rated torque is required. However, the torque density achieved is no better than some DD motors [21]. For instance, the Prius motor achieves a torque density of 80 Nm/L at peak current value[22].
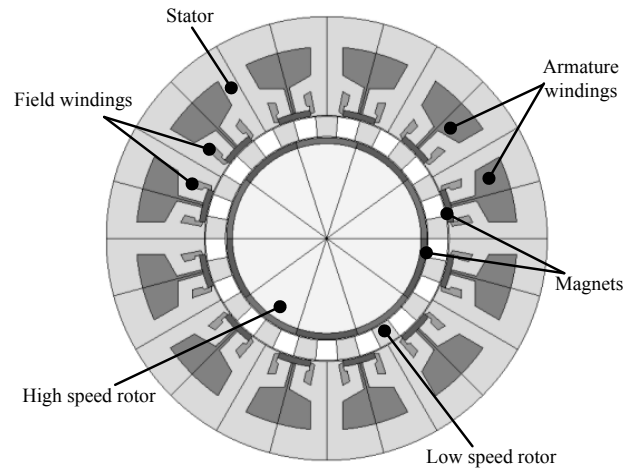
Figure 1-6. Proposed magnetically geared motor [19]
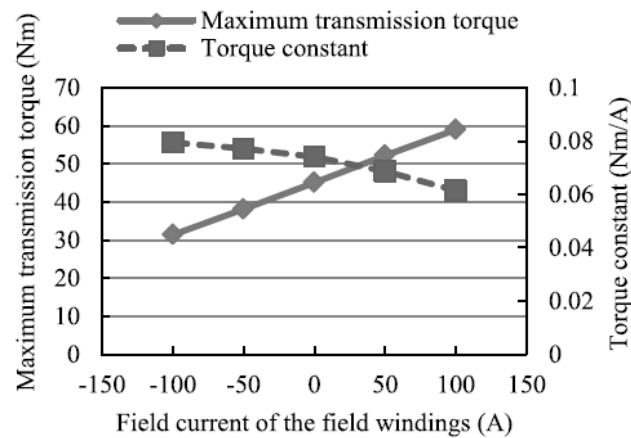
Figure 1-7: Maximum transmission torque and torque constant [19]

1.2.2 Magnetically Geared Machine Designs with Inner Rotor Stator

In 2009 Rasmussen *et al.* presented an inner stator MGM with a wide torque-speed operating range [11]. The mechanical layout of this design is shown in Figure 1-8 and Figure 1-9. The design had p_1 = 6 pole pairs, p_3 = 53 pole pairs with n_2 = 59 steel pieces in between. This gave a gear ratio of 8.67:1. The measured torque density was

130 Nm/L [11]. The MGM was designed for use in an electric vehicle. No liquid cooling system was required for this design.

Figure 1-8: Mechanical Layout of the inner stator MGM design [11]

Figure 1-9: Section view of the inner stator MGM design [23]

In 2013, Rasmussen *et al.* modified the previous version of the inner stator MGM to lower the losses mainly caused by the end plate material assembly, mistakes and a poor starting point for the design. This revised version is shown in Figure 1-10, the cross section and the final assembled design is shown in Figure 1-11. The design had much lower losses. The calculated torque density and the measured torque density of the machine were 113 Nm/L and 92 Nm/L respectively [10]. The MGM had an outer diameter of 268.5 mm and a stack length of 100 mm and was tested in an electric vehicle.

In 2015, Rasmussen *et al.* designed a third MGM for vehicle traction [23]. The exploded view and the section view of the design areas are shown in Figure 1-12. The MGM had $p_1 = 4$ pole pairs, $n_2 = 36$ steel poles and $p_3 = 32$ pole pairs. The pole pair number was reduced so as to reduce the electrical frequency. The measured torque density of the machine was 99.2 Nm/L. The MGM had an outer diameter of 260 mm and a stack length of 195 mm. The refined MGM was tested in an EV converted Audi.
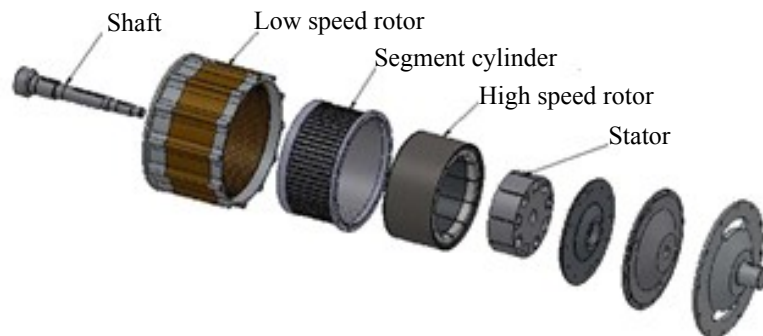
Figure 1-10.Exploded view of MGM [10]

(a)　　　　　　　　　　　　　(b)
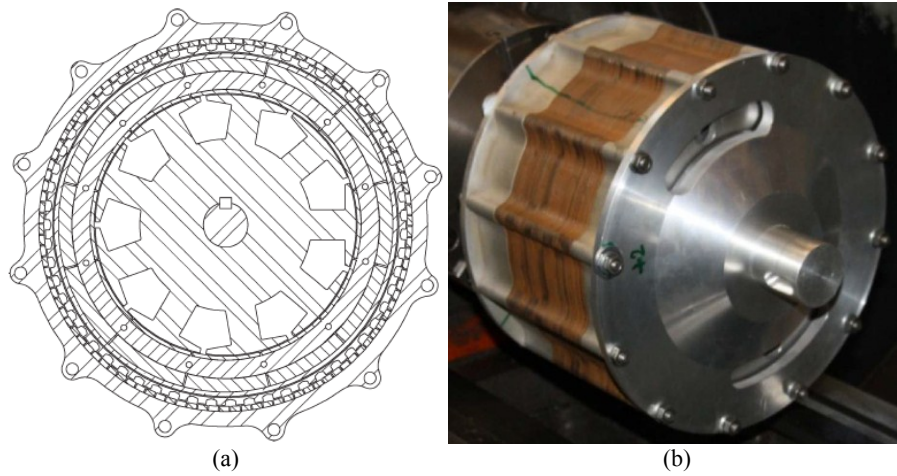
Figure 1-11:(a) The cross section of the MGM and (b) the final assembled design [10]

Resolver　High speed rotor　　　Segment rotor (output/low speed rotor)

LS rotor (fixed)

Drive shaft

Terminal enclosure　　　Stator and shaft

(a)

Shaft

Channels for cooling water

Stator

Motor magnets

Motor and HS gear back iron

High speed gear magnets

Steel segments

Low speed gear magnets

Low speed back iron

Water jacket

(b)
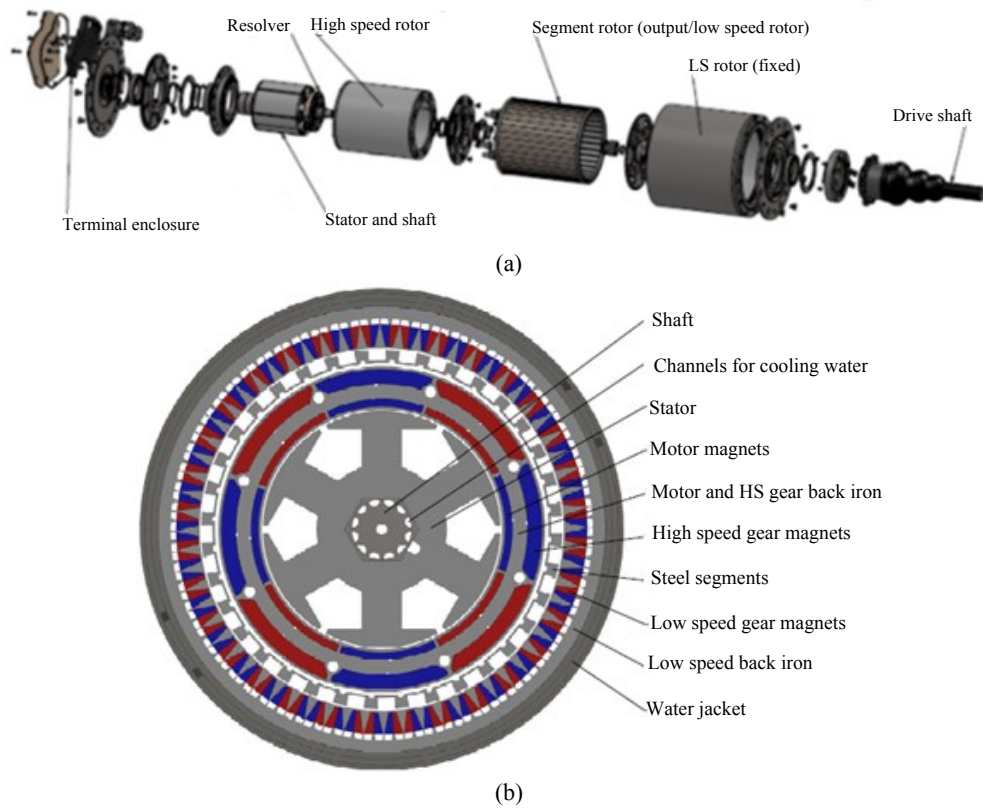
Figure 1-12: (a) Exploded view and (b) Section view of the MGM design [23]

In 2007, Chau *et al.* proposed and designed a 2 kW MGM [24] with an inner stator motor. Figure 1-13 shows the proposed motor design. The inner rotor is shared between the inner stator and outer MG. The design had $p_1 = 3$ pole pairs on the inner rotor, $n_2 = 25$ stationary steel pieces and $p_3 = 22$ pole pairs on the outer rotor. This design was proposed for use in an in-wheel motor for motorcycles and for electric vehicles. The machine was calculated to have a very high efficiency and high power density [24]. The proposed design has a gear ratio of 7.33:1 with a calculated torque density of 84 Nm/L. A fractional slot stator was used so as to reduce the cogging torque.

In 2009, Jian *et al.* proposed using the same type of 7.33:1 ratio MGM with an inner stator [13] in a wind power generator. Figure 1-14 shows the configuration of the proposed design with a gear ratio of 7.33:1. To capture wind power directly, the wind turbine blades could be mounted on the outer rotor. The overall calculated torque density obtained for this machine was 87 Nm/L when the outer diameter was 184 mm.
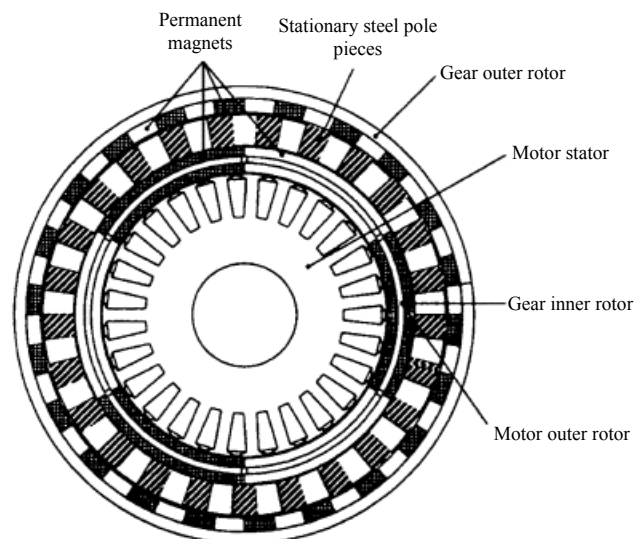
Figure 1-13. Proposed MGM with inner rotor stator [24]
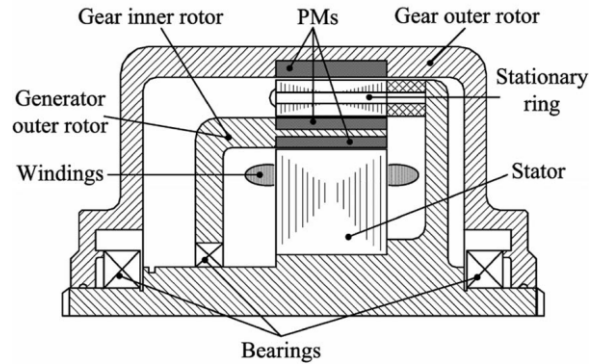
Figure 1-14. Proposed motor configuration [13]

In 2013, Gerber and Wang investigated the performance of a coupled and decoupled MGM with an inner stator [25]. The coupled configuration which is shown in Figure 1-15(a), had a common flux path for both MG and PM machine whereas, the decoupled configuration shown in Figure 1-15(b) splits the machine into a separate MG and PM machine [25]. The coupled and decoupled inner stator MGMs were maximized using the same volumetric dimensions and material properties. The coupled configuration was selected as it achieved the highest torque per active mass of 21.2 Nm/kg compared to 17.9 Nm/kg for the decoupled configuration.

(a)   (b)
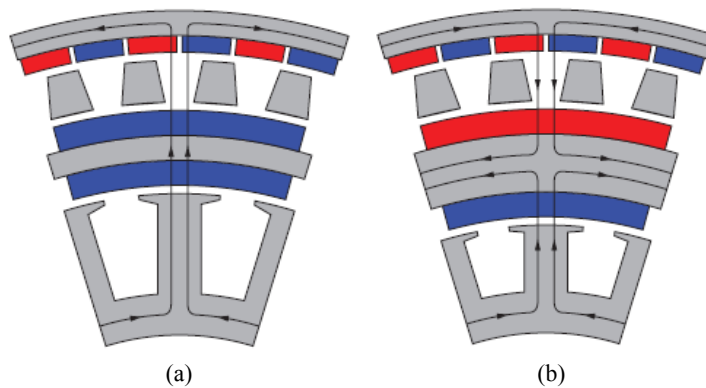
Figure 1-15.(a) Coupled magnetic circuit configuration and (b) decoupled magnetic circuit configuration for geared inner stator machine [25]

The optimal design layouts are shown in Figure 1-16. The final design with coupled configuration was further studied by using 3D FEA. It produced a torque density of 94.5 Nm/L at an outer diameter of 140 mm and stack length of 50 mm [25].

Gerber and Wang also compared the performance of the two different coupled machine typologies, shown in Figure 1-17: one with surface mounted magnets on the high speed rotor and   another where magnets were inserted in a special laminated carrier ring [16]. The 2-D calculated performance of the two maximized designs is presented in Table 1.1.

(a)   (b)
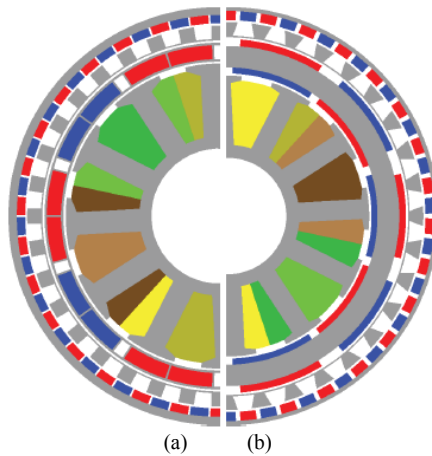
Figure 1-16.(a) Coupled and (b) decoupled magnetic circuit
configuration for GIS [25]

(a)   (b)
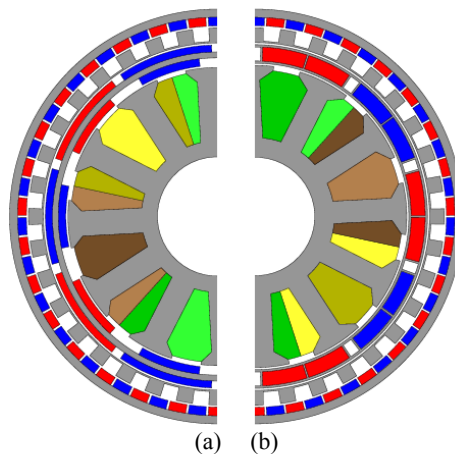
Figure   1-17.(a) Yoke   with   surface   mounted
magnets on both sides   and (b) laminated magnets
in cavities [16]

TABLE 1.1
PERFORMANCE COMPARISON OF TWO INNER STATOR MGM DESIGNS
WITH COUPLED ROTOR [16]

Parameter	Carrier ring magnets	Surface mounted magnets
Inner rotor magnet loss	2.45 W	26.91 W
Inner rotor core loss	3.14 W	1.28 W
Total loss	103.9 W	126.4 W
Calculated stall torque	88.2 Nm	94.4 Nm
Calculated torque density	115 Nm/L	122 Nm/L
Measured stall torque	82 Nm	-
Calculated torque density	107 Nm/L	-

Based on the Table 1.1, the results and other design considerations, the magnet carrier ring design were selected for prototyping. The mechanical design of the prototype is as shown in Figure 1-18. The constructed design is shown in Figure 1-19. The outer diameter and the stack length chosen were 140 mm and 50 mm respectively. The setup to test the prototype is shown in Figure 1-20. The prototype achieved 93% of its calculated stall torque. This corresponded to an active volume torque density of 107 Nm/L.
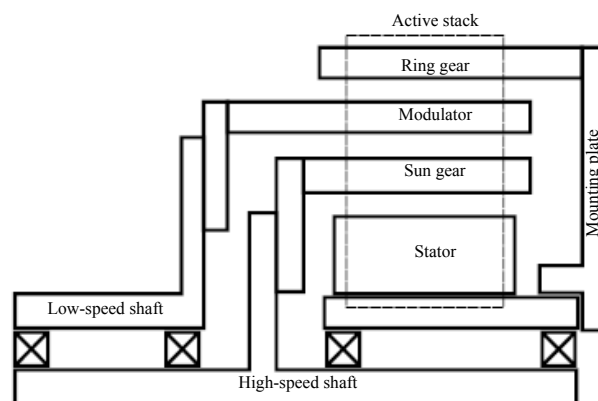
Figure 1-18: Mechanical design of the prototype [16]
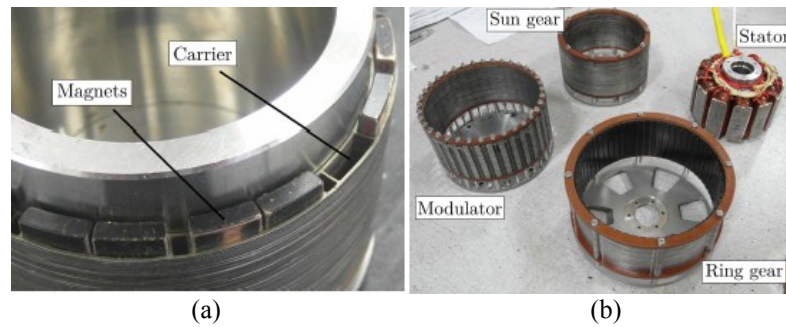
Figure 1-19 (a)Magnets in laminated carriers in the inner rotor and (b) different components used for assembly [16]
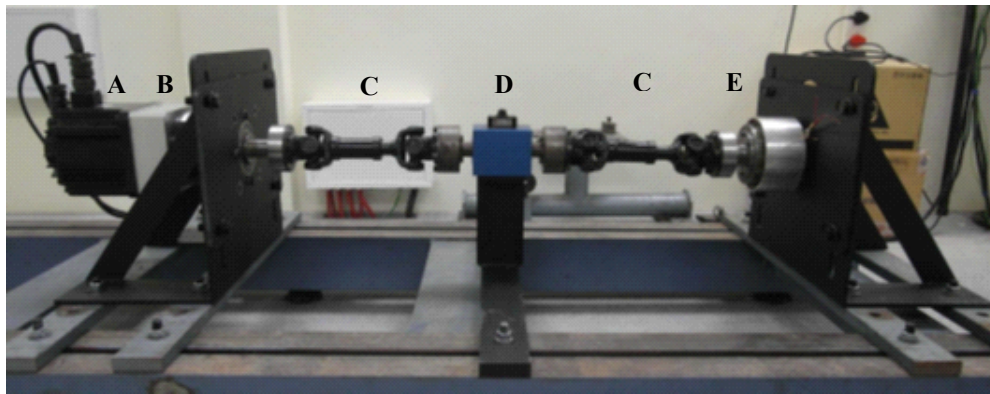
Figure 1-20: Setup used to test the prototype. A: servo motor. B: gearbox. C: prop shaft. D: torque sensor. E: MGM prototype [16]

1.2.3   Continuously Variable Magnetic Gear

In 2010, Jian *et al.* simulated the performance of a 2.6:1 nominal gear ratio continuously variable magnetic gear (CVMG) that used a dual Halbach rotor structure and an outer control rotor stator [26]. The calculated torque and torque density were 816 Nm and 136.6 Nm/L respectively.

In 2011, Atallah *et al.* designed and tested a CVMG with a 1.23:1 nominal gear ratio using a stator that interacted with an outer control rotor [27, 28]. The design is shown in Figure 1-21. Atallah calculated a torque density of 37.8 Nm/L, while the measured torque density achieved was 26.4 Nm/L [27].
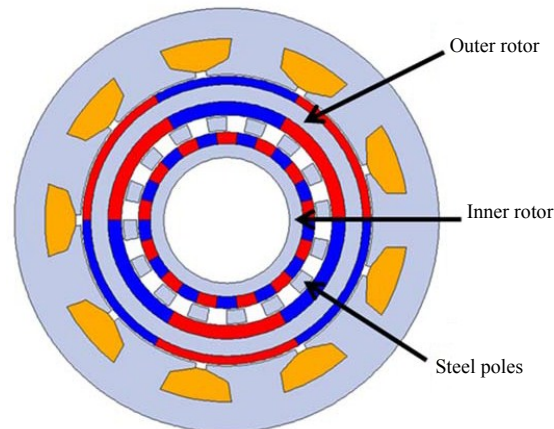
Figure 1-21: CVMG designed by Atallah [28]

In 2012, Zhu proposed integrating a planetary gear with a stator so as to form a planetary magnetically geared motor (PMGM) [29] shown in Figure 1-22. Zhu suggested that the PMGMs could be used in hybrid electric vehicles. Hybrid electric vehicles use continuous variable transmission (CVT) so as to obtain a variable gear ratio. A proposed CVT using the PMGM is shown in Figure 1-23. The engine shaft was connected to the axis of the sun gear and the magnetic planetary gear rotor was connected to the wheel drive shaft. The outer stator was connected to the outer rotor as shown in Figure 1-22. The drawback with this design was that the stator must provide a large torque and therefore the torque rating of the stator was not very much lower than what a direct drive machine would require. The efficiency of the PMGM was calculated to range from 87.5% to 95% over a range of output power from 3.5 kW to 15 kW. The calculated torque density was 57 Nm/L at an outer diameter of 194 mm.
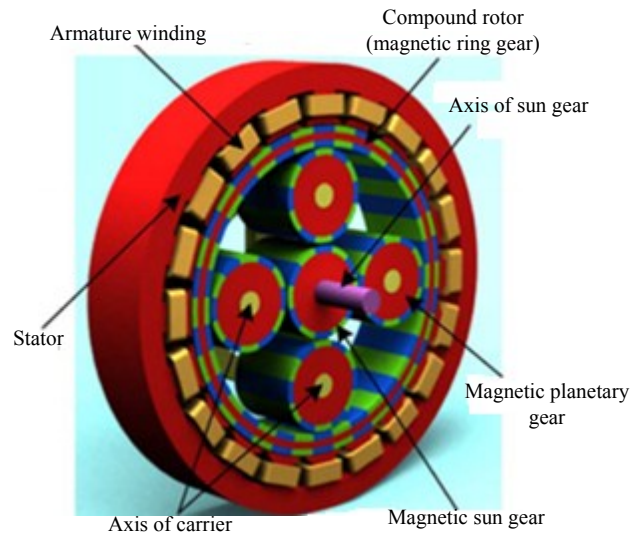
Figure 1-22. The proposed planetary MGM [29]
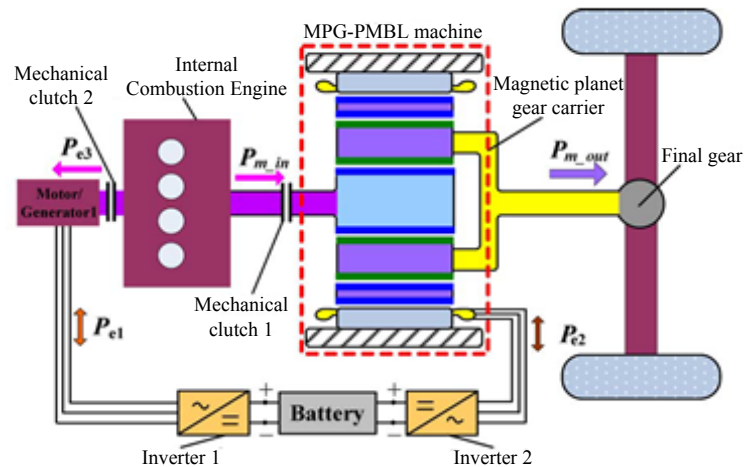
Figure 1-23: The electric CVT system using the PMGM machine [29]

In 2013, Padmanathan *et al*. proposed using an outer stator to create a continuously variable MG (CVMG). The 4.25:1 nominal gear ratio CVMG with a flux focusing control rotor [30] is shown in Figure 1-24. The stator with a fractional slot winding was added to an existing flux focusing coaxial MG, so the stator would couple
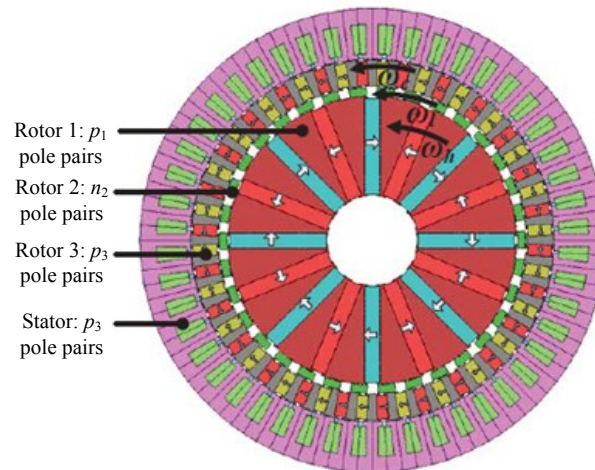
Figure 1-24: A flux focusing CVMG [30]

with the outer rotor and, hence, operates with a variable gear ratio. The CVMG enables the output speed to be made constant despite variations of the input speed. The outer MG rotor, called the control rotor shares the magnetic flux with both the stator and the inner MG rotors. The stator interacts with the outer rotor and hence the torque production is more directly connected. However, the disadvantage of this approach was that the required stator torque would be higher than what was needed to interact with the higher speed inner rotor [27].

1.2.4   Magnetically Geared Machine Performance Comparison

In the paper [31], the authors Fu *et al*. compared the performance of a flux modulated(FM) motor with those of an inner stator MGM and a fractional slot PM motor by using FEA. These designs are shown in Figure 1-25. An FM motor has the form of an MG but the inner PM rotor has been replaced with a stator. The FM motor is shown in Figure 1-25(b). The motor has the same type of form as a vernier motor [32]. The stator of the FM motor has the same number of pole pairs as that of the high speed rotor of the

MG and the maximum locked rotor torque was calculated to be 58 Nm. The inner stator MGM is shown in Figure 1-25(a) has $p_1 = 3$ pole pair on the inner rotor and $p_3 = 22$ pole pair on the outer rotor so the gear ratio is 7.3:1. The maximum output torque for this design was 293 Nm. The fractional slot motor shown in Figure 1-25(c) was used as the baseline conventional PM motor in this comparison study. The maximum locked rotor torque of this design was 59.5 Nm. The outer diameter of the machines was fixed at 92 mm. Table 1.3 shows the performance comparison of the three different motors. The high torque and torque density achievable by the MGM is evident. The FM motor has a similar torque density to that of the fractional slot PM motor with same current density. Therefore, it can be concluded that there is no benefit of using flux modulation without the inner permanent magnet rotor.

In paper [24], authors Gerber *et al*. compared the magnetically geared inner stator machine (GIS machine), the magnetically geared outer stator machine (GOS machine) with the fractional slot PM machine (FS machine) shown in Figure 1-26 . The machines were to be compared based on their torque densities, active mass and copper loss. The specifications for the purpose of comparison are listed in Table 1.3. The three machines occupied the same volume and have the same stack length and outer diameter. The lengths of all air gaps were the same. The number of outer magnet pole pairs was fixed at 17; hence, for a given operating speed; the operating frequency was roughly the same. The current density was fixed to 4 A/mm^2, which is acceptable for naturally air-cooled machines. No constraints were specified on the use of materials as the goal was to maximize the torque per active mass. From Table 1.4, it is evident that for a given volume, the volume torque densities of the geared machines exceed that of conventional FS machines. The use of magnets and the torque per kg magnet mass of the FS machine

is not significantly higher than the geared machines. Although the geared machines are complex to construct, they have higher torque densities.
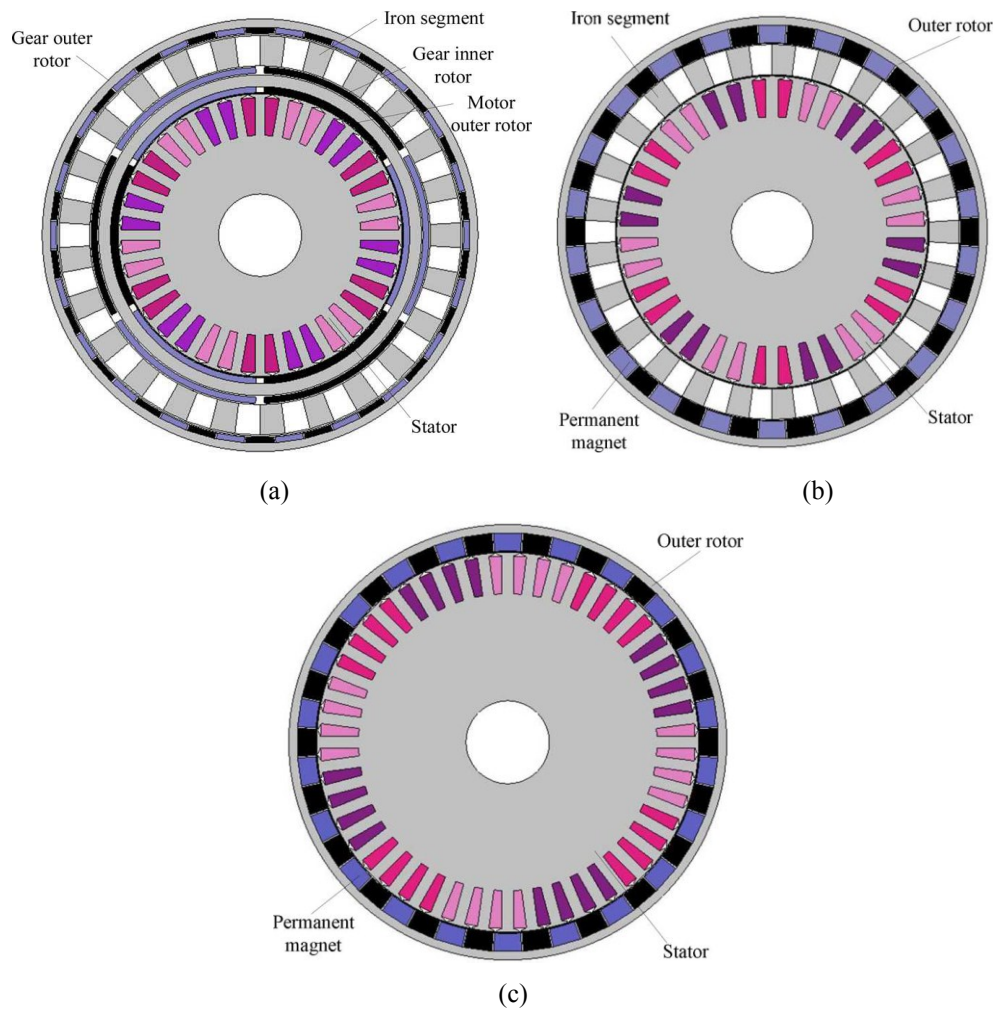
Figure 1-25: (a) MGM with internal stator and high speed rotor ,(b) FM motor with no inner rotor, (c) Fractional slot motor [31]
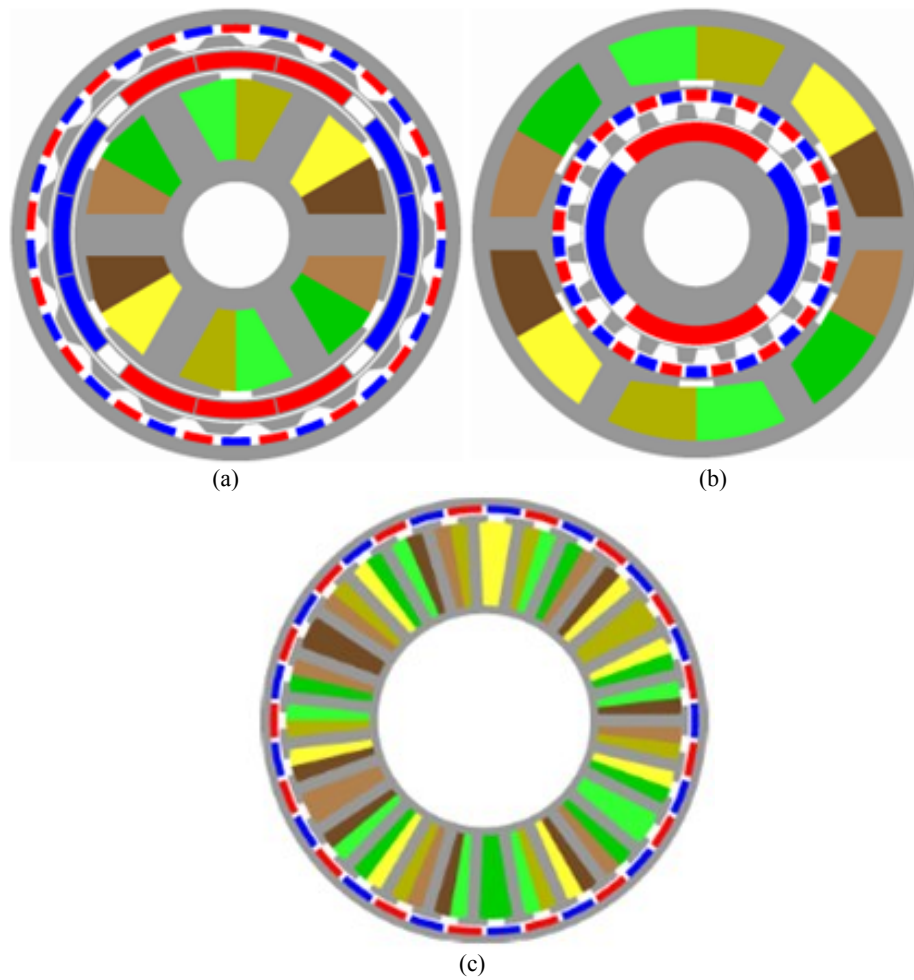
Figure 1-26: (a) Magnetically geared outer stator machine (GOS), (b) Magnetically geared inner stator machine(GIS) and (c) Conventional fractional slot PM machine [33]

The torque density of the 2010 Toyota Prius electric drive subsystem motor, considered state of the art in alternative vehicle technologies, is 82 Nm/L at peak and that of about 40 Nm/L for continuous operation [22]. Magnetically geared motors can be designed to have higher torque densities than the 2010 Toyota Prius motor.

TABLE 1.2
PERFORMANCE COMPARISON OF INNER STATOR MGM, FM MOTOR AND
FRACTIONAL SLOT MOTOR [31]

Motor type	MGM	FM motor	Fractional slot motor
Maximum locked rotor torque(Nm)	40	58	60
Output torque (Nm)	293	57	59.5
EMF of full load (V)	10	7.6	5
Cogging torque (Nm)	0.59	0.03	0.23
Core loss (W)	260	60	88
Torque density (Nm/L)	276	54	56

TABLE 1.3
MACHINE SPECIFICATIONS OF INNER STATOR MGM, FM MOTOR
AND FRACTIONAL SLOT MOTOR [33]

Description	Value	Unit
Outer diameter	140	mm
Minimum inner diameter	24	mm
Air-gap length	0.7	mm
Stack length	50	mm
Number of outer magnet pole pairs	17	-
Current density	4	A/mm^2
Copper fill factor	0.55	-

TABLE 1.4
PERFORMANCE COMPARISON OF FRACTIONAL SLOT, GEARED INNER STATOR
AND GEARED OUTER STATOR MGMS [33]

Description	Fractional Slot	Geared Inner Stator	Geared Outer Stator	Unit
2D Torque	23.24	61.85	58.51	Nm
3D Torque	22.4	56.6	49.0	Nm
3D Torque density	**29.1**	**73.54**	**63.66**	**Nm/L**
Magnet mass	0.31	0.83	0.69	kg
Copper mass	2.40	1.58	2.1	kg
Copper end-winding mass	0.58	1.27	2.25	kg
Steel mass	1.92	2.66	2.52	kg
Total mass	5.20	6.35	7.56	kg
3D Torque/magnet mass	**73.11**	**67.69**	**70.78**	**Nm/kg**
3D Torque/total copper mass	**7.52**	**19.86**	**11.27**	**Nm/kg**
3D Torque/steel mass	**11.69**	**21.26**	**19.47**	**Nm/kg**
3D Torque/total mass	**4.31**	**8.91**	**6.48**	**Nm/kg**
2D Copper loss	40.85	26.88	35.81	W
3D Copper loss	50.73	48.56	74.08	W
3D Torque/copper loss	0.44	1.17	0.66	Nm/W
3D Mechanical power @ 50 Hz	413.95	935.86	810.2	W
Generator efficiency @ 50 Hz [%]	87.75	94.81	90.86	-
3D Mechanical power@150 rpm	351.86	889.07	769.69	W
Generator efficiency @ 50 Hz [%]	85.58	94.54	90.38	-

The volumetric torque density for the various magnetically geared machines discussed in this review is summarized in Figure 1-27. The magnetically geared machines are complex to construct but have higher torque densities than conventional machines for a given volume. The use of magnetically geared machines in several field of applications have been discussed which shows their improved performance when compared to conventional machines.
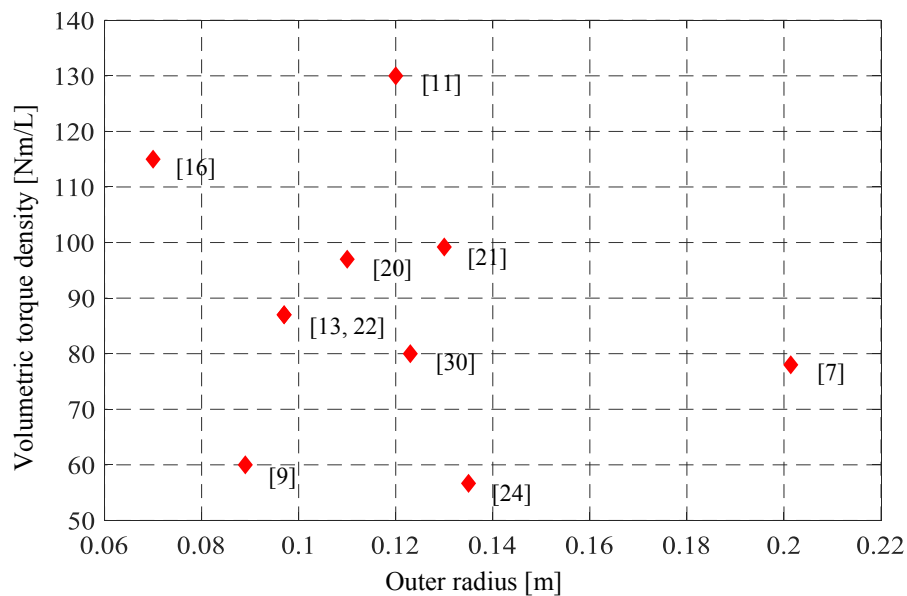
Figure 1-27: Variation of volumetric torque density for various magnetically geared machines

2   COAXIAL MG TYPOLOGY ANALYSIS

2.1   Principle of Operation of Magnetic Gear

A coaxial MG as shown in Figure 2-1 consists of three rotors, an inner rotor consisting of p_1 pole pairs, an outer rotor consisting of p_3 pole pairs and a cage rotor consisting of n_2 steel pieces. The steel pieces on the cage rotor act as field modulators to change the pole pairs between inner and outer air gaps. When the inner and the outer rotor fields pass through the steel pieces on the cage rotor, space harmonics are created in the outer and inner air gaps respectively. These magnetic fields, created by the inner and outer rotors, are coupled via the steel pieces and interact with each other to transfer torque. The working principle of the typical MG is further explained in detail using the linear model shown in Figure 2-2.
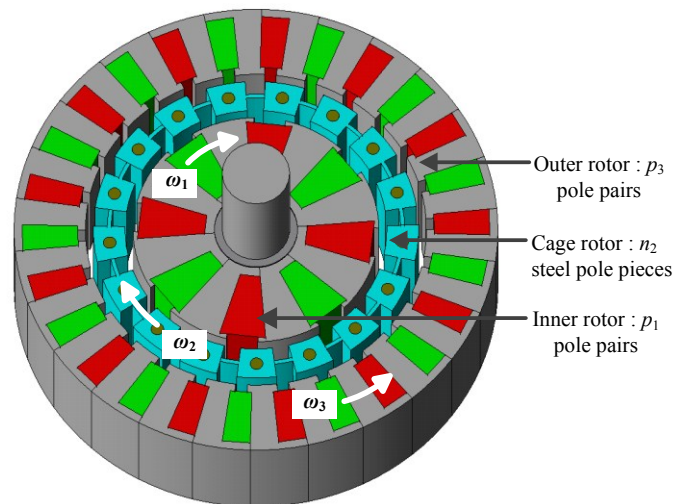
Figure 2-1: MG with pole pairs p_1=4, n_2=17 steel poles and p_3=13 pole pairs
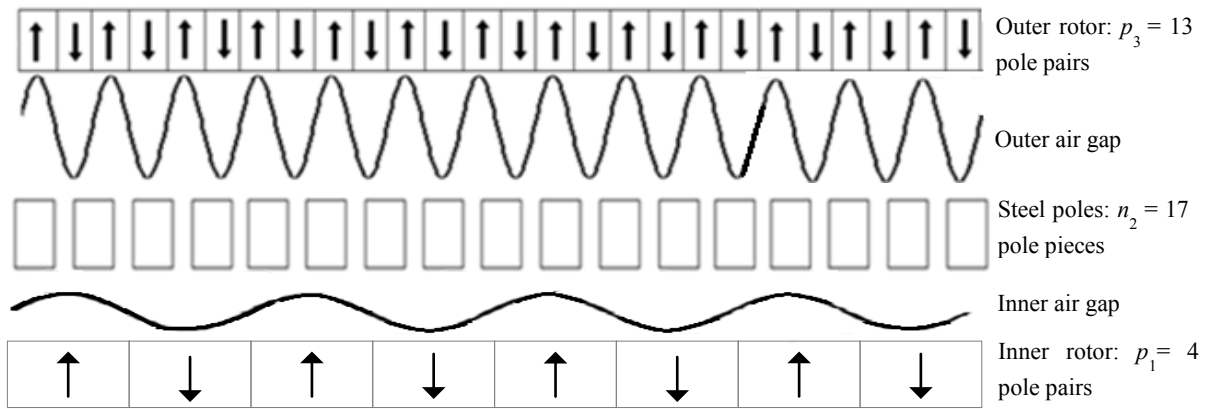
Figure 2-2: Typical MG modified into linear model [34]

For clarity, the typical MG design is represented as a linear model as shown in Figure 2-2. The linear model has $p_1 = 4$ pole pairs on the inner rotor, $n_2 = 17$ steel pieces on the cage rotor and $p_3 = 13$ pole pairs on the outer rotor. The magnetic field created by the inner rotor has a dominant 4th harmonic due to 4 pole pairs which is modulated by the 17 steel poles on the cage rotor. This results in a field with a dominant 13th harmonic in the outer air gap adjacent to the outer rotor. This is illustrated in Figure 2-2. This field will then interact with the 13th harmonic of the field created by the 13 pole pairs on the outer rotor and consequently transfer continuous average torque.

In order for the rotors to be in a coupled condition and to maximize the torque, the following condition must be satisfied [35]

$$n_2 = p_1 + p_3 \qquad (2.1)$$

In the most general case, the inner rotor with p_1 pole pairs, outer rotor with p_3 pole pairs and the steel poles with n_2 segments can all be rotated at speeds ω_1, ω_3, and ω_2 respectively. The rotors will create additional space harmonics and a field harmonic

analysis can be used to derive the general governing speed equations. The production of torque in an MG using harmonic analysis can be explained with the help of the following 4 cases that are illustrated in Figure 2-3. The rotors used are in a flux focusing typology.

Case (a) shows the arrangement for the calculation of flux density produced by the high speed inner rotor magnets in the inner air gap Figure 2-3(a).

Case (b) shows the arrangement for the calculation of flux density produced by the high speed inner rotor magnets in the outer air gap Figure 2-3 (b).

Case (c) shows the arrangement for the calculation of flux density produced by the stationary outer rotor magnets in the inner air gap Figure 2-3(c).

Case (d) shows the arrangement for the calculation of flux density produced by the stationary outer rotor magnets in the outer air gap Figure 2-3(d).

Case (b) and (c) shows the arrangements for analyzing the effect of the modulating segments on the field produced by one source, in the air gap adjacent to the other source.
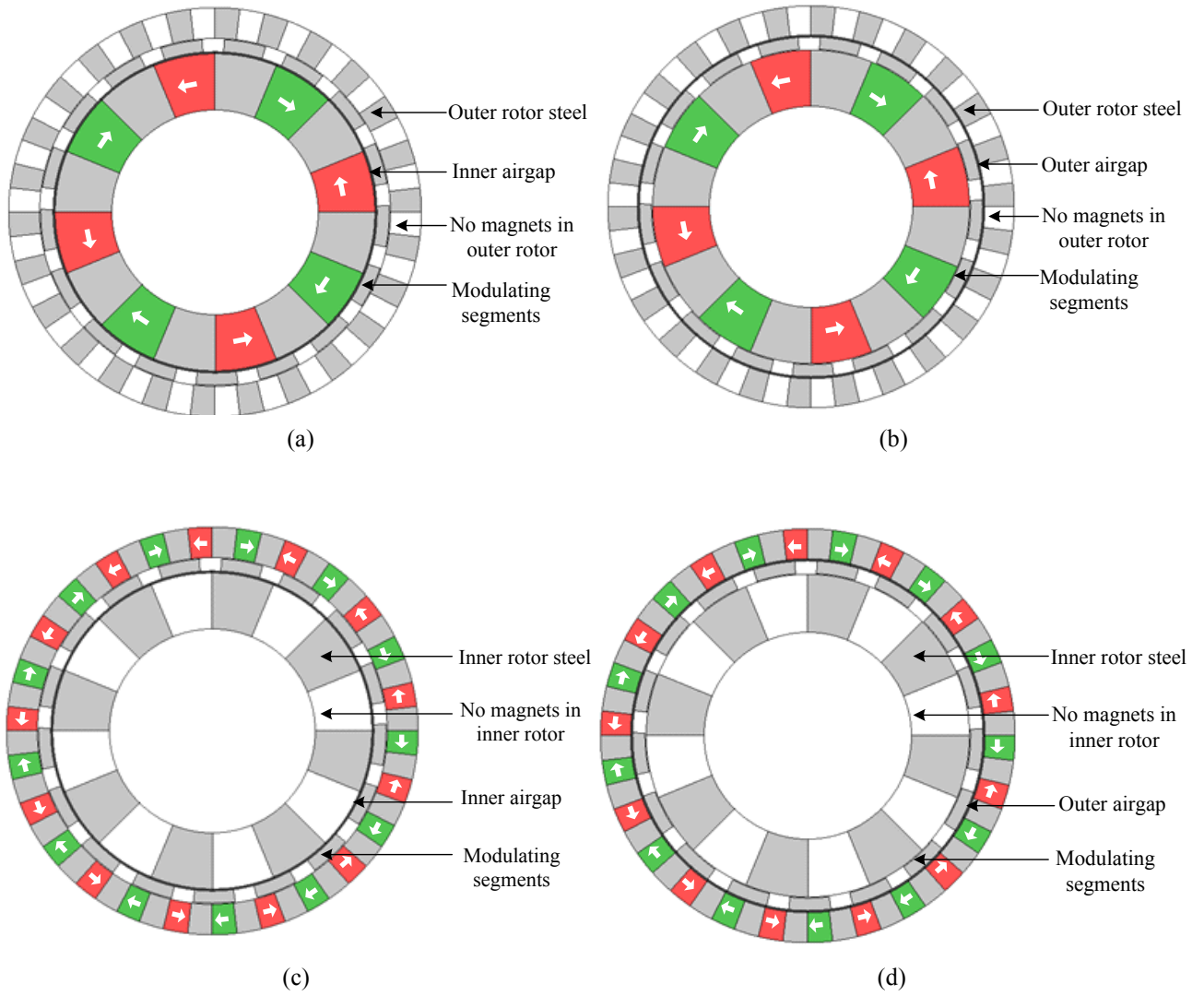
Figure 2-3: Arrangement for flux density calculation (a) inner rotor field in the inner air gap (b) inner rotor field in the outer air gap (c) outer rotor field in the inner air gap (d) outer rotor field in the outer air gap

2.1.1   Harmonic Analysis of the Fields Produced by the Inner Rotor at the Inner and Outer Air Gaps

Let us denote the radial flux density at a distance r produced by the high speed inner rotor as B_r^1 and the corresponding azimuthal flux density is denoted by B_θ^1. Using Fourier series, the flux densities can be written as

$$B_r^1(r,\theta,t) = \sum_{m=1,3,5,\dots}^{\infty} b_{r,m}^1(r)\cos[mp_1(\theta - \omega_1 t) + mp_1\delta_1] \tag{2.2}$$

$$B_\theta^1(r,\theta,t) = \sum_{m=1,3,5,\dots}^{\infty} b_{\theta,m}^1(r)\cos[mp_1(\theta - \omega_1 t) + mp_1\delta_1] \tag{2.3}$$

where, δ_1 is the initial phase angle at time $t = 0$. The numeric subscript and superscript denotes that we are referring to the rotors with '1' as the high speed rotor, '2' the modulating steel segments and '3' the low speed rotor, m denotes the harmonic number and subscript 'r' and 'θ' denote the radial and the azimuthal components respectively.

The radial flux density produced by the inner rotor at the inner air gap is shown in Figure 2-4(a). This is the same arrangement as mentioned in case (a). The harmonic analysis illustrated in Figure 2-4(b) shows that the inner rotor, at the inner air gap, only creates harmonics which are odd multiples of the inner rotor pole pair numbers.
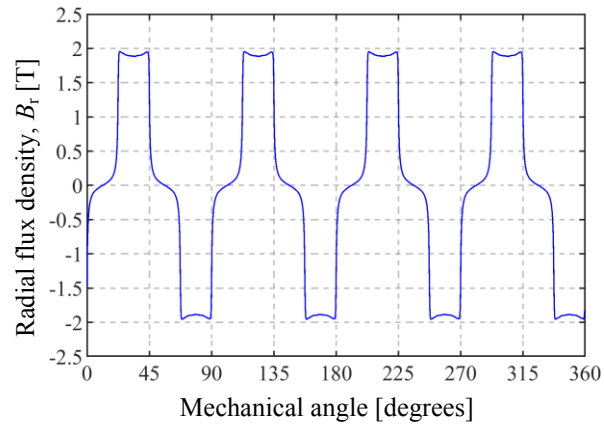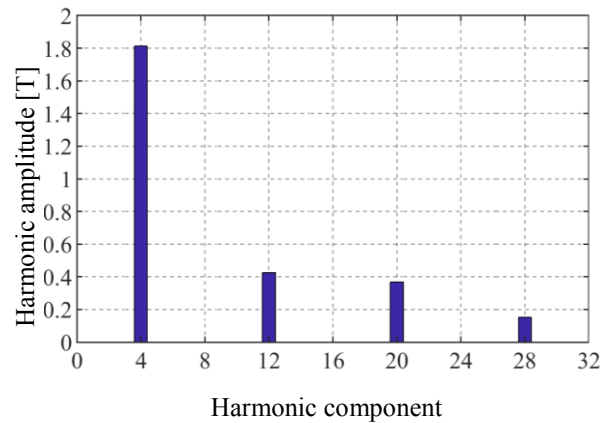
Figure 2-4: (a) Radial flux density produced by inner rotor at the inner air gap and (b)harmonic components of the radial field

The azimuthal flux density produced by the inner rotor at the inner air gap is shown in Figure 2-5(a). The corresponding harmonic analysis is illustrated in Figure 2-5(b). Like the radial flux density, this harmonic analysis also shows the presence of odd harmonics which are multiples of the inner rotor pole pairs.
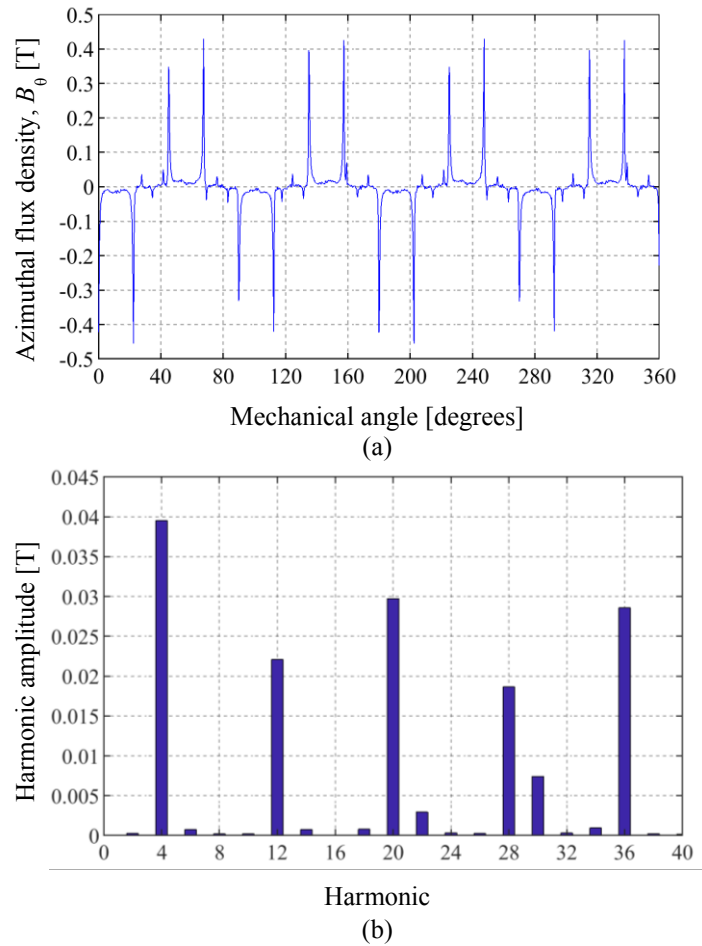
Figure 2-5: (a)Azimuthal flux density produced by inner rotor at the inner air gap and (b) harmonic components of the azimuthal field

When the steel pieces of the cage rotor exist, the magnetic lines of flux will distribute along the steel pieces due to the absence of any other magnetic medium around them. This modulation effect of the steel pieces of the cage rotor can be expressed mathematically by radial and azimuthal components. Using Fourier series, the radial and the azimuthal components of the modulation function are written as [36].

$$\lambda_r^2(r,\theta,t) = \lambda_{r,0}^2(r) + \sum_{j=1,3,5,\ldots} \lambda_{r,j}^2(r)\cos[jn_2(\theta - \omega_2 t) + jn_2\delta_2] \tag{2.4}$$

$$\lambda_\theta^2(r,\theta,t) = \lambda_{\theta,0}^2(r) + \sum_{j=1,3,5,\ldots} \lambda_{\theta,j}^2(r)\cos[jn_2(\theta - \omega_2 t) + jn_2\delta_2] \tag{2.5}$$

where, δ_2 is the initial phase angle at time $t = 0$ for the rotor. When modulated by the steel

pieces, the inner rotor field at the outer air gap, shown in Figure 2-3(b) can be obtained

from

$$B_r^{1,2}(r,\theta,t) = B_r^1(r,\theta,t)\lambda_r^2(r,\theta,t) \tag{2.6}$$

Substituting, (2.2) and (2.4) into (2.6) gives

$$B_r^{1,2}(r,\theta,t) = \sum_{m=1,3,\ldots} \lambda_{r,0}(r)b_{r,m}^1(r)\cos\left[mp_1(\theta - \omega_1 t) + mp_1\delta_1\right]$$
$$+ \sum_{m=1,3,\ldots}\sum_{j=1,3,\ldots} \lambda_{r,j}^2(r)b_{r,m}^1(r)\cos\left[mp_1(\theta - \omega_1 t) + mp_1\delta_1\right]\cos\left[jn_2(\theta - \omega_2 t) + jn_2\delta_2\right] \tag{2.7}$$

Using the trigonometric function given by

$$\cos(A)\cos(B) = \frac{\cos(A+B) + \cos(A-B)}{2} \tag{2.8}$$

we obtain,

$$B_r^{1,2}(r,\theta,t) = \lambda_{r,0}^2(r_s)\sum_{m=1,3,\ldots} b_{r,m}^2(r)\cos\left[mp_1(\theta - \omega_1 t) + mp_1\delta_1\right]$$
$$+ \sum_{m=1,3,\ldots}\sum_{j=1,3,\ldots} \frac{\lambda_{r,j}^2(r)b_{r,m}^1(r)}{2}\Big(\cos\left[mp_1\theta - mp_1\omega_1 t + mp_1\delta_1 + jn_2\theta - jn_2\omega_2 t + jn_2\delta_2\right]$$
$$+ \cos\left[mp_1\theta - mp_1\omega_1 t + mp_1\delta_1 - jn_2\theta + jn_2\omega_2 t - jn_2\delta_2\right]\Big) \tag{2.9}$$

Rearranging (2.9) gives,

$$B_r^{1,2}(r,\theta,t) = \lambda_{r,0}^2(r)\sum_{m=1,3,..} b_{r,m}^1(r)\cos\left[mp_1\left(\theta-\omega_1 t\right)+mp_1\delta_1\right]$$

$$+\sum_{m=1,3,..}\sum_{j=1,3,..}\frac{\lambda_{r,j}^2(r)b_{r,m}^1(r)}{2}\left(\cos\left[\left(mp_1+jn_2\right)\left(\theta-\frac{mp_1\omega_1+jn_2\omega_2}{mp_1+jn_2}t\right)+\left(mp_1\delta_1+jn_2\delta_2\right)\right]\right.$$

$$\left.+\cos\left[\left(mp_1-jn_2\right)\left(\theta-\frac{mp_1\omega_1-jn_2\omega_2}{mp_1-jn_2}t\right)+\left(mp_1\delta_1-jn_2\delta_2\right)\right]\right)$$

(2.10)

Similarly, the azimuthal field at the outer air gap, obtained by the modulation action of the steel pieces on the inner rotor field can be expressed as

$$B_\theta^{1,2}(r,\theta,t) = B_\theta^1(r,\theta,t)\lambda_\theta^2(r,\theta,t)$$

(2.11)

Substituting (2.3) and (2.5) into (2.11) and utilizing (2.8) gives,

$$B_\theta^{1,2}(r,\theta,t) = \lambda_{\theta,0}^2(r)\sum_{m=1,3...} b_{\theta,m}^1(r)\cos\left[mp_1\left(\theta-\omega_1 t\right)+mp_1\delta_1\right]$$

$$+\sum_{m=1,3,..}\sum_{j=1,3,..}\frac{\lambda_{\theta,j}^2(r)b_{\theta,m}^1(r)}{2}\left(\cos\left[\left(mp_1+jn_2\right)\left(\theta-\frac{mp_1\omega_1+jn_2\omega_2}{mp_1+jn_2}t\right)+\left(mp_1\delta_1+jn_2\delta_2\right)\right]\right.$$

$$\left.+\cos\left[\left(mp_1-jn_2\right)\left(\theta-\frac{mp_1\omega_1-jn_2\omega_2}{mp_1-jn_2}t\right)+\left(mp_1\delta_1-jn_2\delta_2\right)\right]\right)$$

(2.12)

2.1.2   Harmonic Analysis of the Field Produced by Outer Rotor at the Outer and Inner Air Gaps

The radial flux density produced by the outer rotor at the outer air gap is shown in Figure 2-6(a). This is the same arrangement as mentioned in case (d) of Figure 2-3. The harmonic analysis depicted in Figure 2-6(b) shows that the outer rotor, at the outer air gap, also creates only odd harmonics which are multiples of the outer rotor pole pair numbers. The corresponding azimuthal flux density is shown in Figure 2-7(a) and the harmonic analysis illustrated in Figure 2-7(b) also shows the presence of odd harmonics which are multiples of the outer rotor pole pair numbers.
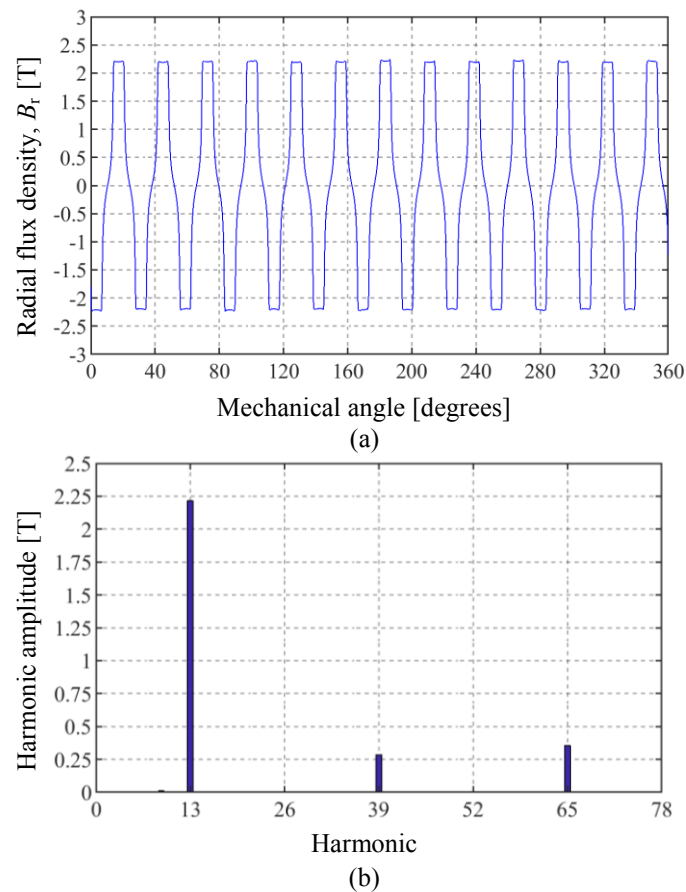
Figure 2-6: (a) Radial flux density produced by outer rotor at the outer air gap and (b)harmonic components of the radial field
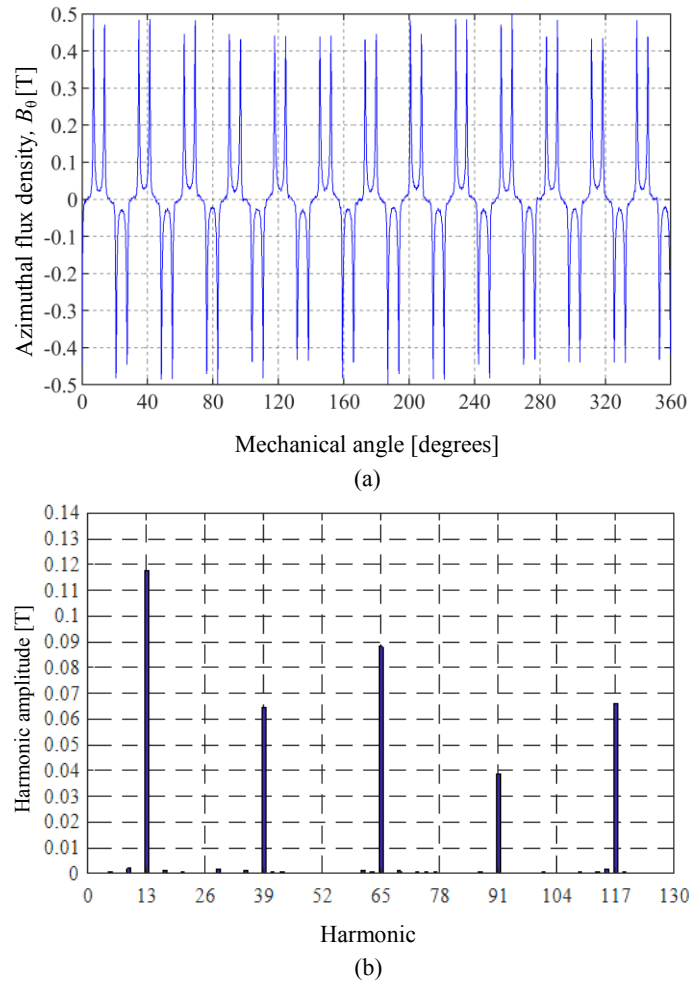
Figure 2-7: (a) Azimuthal flux density produced by outer rotor at the outer air gap and (b)harmonic components of the field

The radial and the azimuthal field produced by the outer rotor magnets in the outer air gap can be expressed as

$$B_r^3(r,\theta,t) = \sum_{k=1,3,5,..} b_{r,k}^3(r)\cos[kp_3(\theta-\omega_3 t)+kp_3\delta_3] \qquad (2.13)$$

$$B_\theta^3(r,\theta,t) = \sum_{k=1,3,5,..} b_{\theta,k}^3(r)\cos[kp_3(\theta-\omega_3 t)+kp_3\delta_3] \qquad (2.14)$$

where k denotes the harmonic number.

Through the modulation of the cage rotor steel pieces, the radial flux density and azimuthal flux density of the outer rotor field in the inner air gap shown in Figure 2-3(d) can be computed from the following equations

$$B_r^{3,2}(r,\theta,t) = B_r^3(r,\theta,t)\lambda_r^2(r,\theta,t) \tag{2.15}$$

and

$$B_\theta^{3,2}(r,\theta,t) = B_\theta^3(r,\theta,t)\lambda_\theta^2(r,\theta,t) \tag{2.16}$$

Substituting (2.13) and (2.4) into (2.15) and using trigonometric identity shown in (2.8) we obtain,

$$
\begin{aligned}
B_r^{3,2}(r,\theta,t) = {}& \lambda_{r,0}^2(r)\sum_{k=1,3,\ldots} b_{r,k}^3(r)\cos\left[kp_3\left(\theta - \omega_3 t\right) + kp_3\delta_3 \right] \\
& + \sum_{k=1,3,\ldots}\sum_{j=1,3,\ldots} \frac{\lambda_{r,j}^2(r)b_{r,k}^3(r)}{2}\left(\cos\left[\left(kp_3 + jn_2\right)\left(\theta - \frac{kp_3\omega_3 + jn_2\omega_2}{kp_3 + jn_2}t\right) + \left(kp_3\delta_3 + jn_2\delta_2\right)\right]\right. \\
& \left. + \cos\left[\left(kp_3 - jn_2\right)\left(\theta - \frac{kp_3\omega_3 - jn_2\omega_2}{kp_3 - jn_2}t\right) + \left(kp_3\delta_3 - jn_2\delta_2\right)\right]\right)
\end{aligned}
\tag{2.17}
$$

Similarly, substituting (2.14) and (2.5) into (2.16) and using (2.8), the azimuthal flux density in the inner air gap can be written as,

$$
\begin{aligned}
B_\theta^{3,2}(r,\theta,t) = {}& \lambda_{\theta,0}^2(r)\sum_{k=1,}^\infty b_{\theta,k}^3(r)\cos\left[kp_3\left(\theta - \omega_3 t\right) + kp_3\delta_3 \right] \\
& + \sum_{k=1}^\infty\sum_{j=1}^\infty \frac{\lambda_{\theta,j}^2(r)b_{\theta,k}^3(r)}{2}\left(\cos\left[\left(kp_3 + jn_2\right)\left(\theta - \frac{kp_3\omega_3 + jn_2\omega_2}{kp_3 + jn_2}t\right) + \left(kp_3\delta_3 + jn_2\delta_2\right)\right]\right. \\
& \left. + \cos\left[\left(kp_3 - jn_2\right)\left(\theta - \frac{kp_3\omega_3 - jn_2\omega_2}{kp_3 - jn_2}t\right) + \left(kp_3\delta_3 - jn_2\delta_2\right)\right]\right)
\end{aligned}
\tag{2.18}
$$

2.1.3 Torque Production Using Maxwell's Stress Tensor

From the definition of Maxwell stress tensor [37], the total torque in an electric machine can be determined by evaluating the surface integral along a closed surface S in the air gap [38] using,

$$T_e = \int_S (r \times \sigma) dS \tag{2.19}$$

where , r is the air gap radius and σ is the stress tensor defined as [38]

$$\sigma = \frac{1}{\mu_0}(B \cdot n)B - \frac{1}{2\mu_0}(B)^2 \cdot n \tag{2.20}$$

and B is the magnetic flux density and n is the unit normal vector of the integration surface.

The force over a surface S is given by [39-42]

$$F = \int_S \sigma \cdot dS \tag{2.21}$$

In cylindrical coordinates, the force components computed on a cylindrical surface can be obtained as [43]

$$F_z = \frac{1}{\mu_0}\int_S B_z B_r dS \tag{2.22}$$

$$F_r = \frac{1}{2\mu_0}\int_S \left[(B_r)^2 - (B_\theta)^2 - (B_z)^2 \right] dS \tag{2.23}$$

$$F_\theta = \frac{1}{\mu_0} \int_s B_\theta B_r \, dS \tag{2.24}$$

The torque T at a distance r can be can be computed as

$$T = \mathbf{F} \times \mathbf{r} \tag{2.25}$$

$$= \begin{vmatrix} \hat{r} & \hat{\theta} & \hat{z} \\ F_r & F_\theta & F_z \\ r & 0 & 0 \end{vmatrix}$$

$$= rF_z \hat{\theta} - rF_\theta \hat{z}$$

Substituting (2.24) in the z component of (2.25), the torque around the z axis at radius r is computed as

$$T = \frac{1}{\mu_0} \int_s rB_r B_\theta \, dS$$

$$= \frac{1}{\mu_0} \int_0^{2\pi} \int_{-d/2}^{d/2} rB_r B_\theta r \, dz \, d\theta$$

$$= \frac{r^2 d}{\mu_0} \int_0^{2\pi} B_r B_\theta \, d\theta \tag{2.26}$$

where, d is the stack length of the MG.

The field at the outer air gap consists of the field produced by the outer rotor poles and the field produced by the inner rotor poles modulated by the cage rotor steel pieces. These are depicted in Figure 2-3 (b) and Figure 2-3 (d). Thus the radial and azimuthal flux densities in the outer air gap at radius r_o can be written as

$$B_r^o = B_r^{1,2} + B_r^3 \tag{2.27}$$

$$B_\theta^o = B_\theta^{1,2} + B_\theta^3 \tag{2.28}$$

where, the superscript and the subscript 'o' denotes the outer air gap.

Similarly, combining the cases shown in Figure 2-3(a) and Figure 2-3(c) the radial and azimuthal flux densities in the inner air gap at radius r_i can be written as

$$B_r^i = B_r^1 + B_r^{3,2} \tag{2.29}$$

$$B_\theta^i = B_\theta^1 + B_\theta^{3,2} \tag{2.30}$$

where, the superscript and the subscript 'i' denotes the inner air gap.

Substituting (2.27) and (2.28) in (2.26) we get,

$$T_o = \frac{r^2 d}{\mu_0} \int_0^{2\pi} \left[B_r^{1,2} B_\theta^{1,2} + B_r^{1,2} B_\theta^3 + B_r^3 B_\theta^{1,2} + B_r^3 B_\theta^3 \right] d\theta \tag{2.31}$$

The first and last term in (2.31) will be zero as the rotor torque is acting on itself. Therefore the torque equation simplifies to

$$T_0 = \frac{r^2 d}{\mu_0} \left(\int\limits_0^{2\pi} B_r^3 B_\theta^{1,2} d\theta + \int\limits_0^{2\pi} B_r^{1,2} B_\theta^3 d\theta \right) \tag{2.32}$$

Similarly, the torque equation in the inner air gap can be written as

$$T_i = \frac{r^2 d}{\mu_0} \left(\int\limits_0^{2\pi} B_r^1 B_\theta^{3,2} d\theta + \int\limits_0^{2\pi} B_r^{3,2} B_\theta^1 d\theta \right) \tag{2.33}$$

The first integral term in (2.33) is made up of two terms (2.2) and (2.18).

Multiplying gives,

$$
B_r^1 B_\theta^{3,2} = \left\{ \sum_{m=1,3,5,\ldots}^\infty b_{r,m}^1(r) \cos[mp_1(\theta - \omega_1 t) + mp_1 \delta_1] \right\} \times
$$
$$
\begin{bmatrix}
\lambda_{\theta,0}^2(r) \sum\limits_{k=1.}^\infty b_{\theta,k}^3(r) \cos\left[kp_3(\theta - \omega_3 t) + kp_3\delta_3 \right] \\
+ \sum\limits_{k=1}^\infty \sum\limits_{j=1}^\infty \frac{\lambda_{\theta,j}^2(r) b_{\theta,k}^3(r)}{2} \left(\cos\left[(kp_3 + jn_2)\left(\theta - \frac{kp_3\omega_3 + jn_2\omega_2}{kp_3 + jn_2} t \right) + (kp_3\delta_3 + jn_2\delta_2) \right] \right. \\
\left. + \cos\left[(kp_3 - jn_2)\left(\theta - \frac{kp_3\omega_3 - jn_2\omega_2}{kp_3 - jn_2} t \right) + (kp_3\delta_3 - jn_2\delta_2) \right] \right)
\end{bmatrix} \tag{2.34}
$$

In order to obtain the speed relation of the MG let us consider only the 1st harmonic. This can be achieved by using $k = m = 1$. Equation (2.34) simplifies to

$$B_r^1 B_\theta^{3,2} = \left\{ b_{r,1}^1(r)\cos[p_1(\theta - \omega_1 t) + p_1\delta_1] \right\} \times$$

$$\left\{ \begin{array}{l} \lambda_{\theta,0}^2(r)b_{\theta,1}^3(r)\cos\left[p_3(\theta - \omega_3 t) + p_3\delta_3 \right] \\[2ex] + \dfrac{\lambda_{\theta,1}^2(r)b_{\theta,1}^3(r)}{2}\left(\cos\left[(p_3 + n_2)\left(\theta - \dfrac{p_3\omega_3 + n_2\omega_2}{p_3 + n_2}t \right) + (p_3\delta_3 + n_2\delta_2) \right] \right. \\[3ex] \left. + \cos\left[(p_3 - n_2)\left(\theta - \dfrac{p_3\omega_3 - n_2\omega_2}{p_3 - n_2}t \right) + (p_3\delta_3 - n_2\delta_2) \right] \right) \end{array} \right\}$$

$$(2.35)$$

Let us denote

$$p_1(\theta - \omega_1 t) + p_1\delta_1 = A$$

$$p_3(\theta - \omega_3 t) + p_3\delta_3 = B$$

$$(p_3 + n_2)\times\left(\theta - \frac{p_3\omega_3 + n_2\omega_2}{p_3 + n_2}t \right) + (p_3\delta_3 + n_2\delta_2) = C$$

$$(p_3 - n_2)\times\left(\theta - \frac{p_3\omega_3 - n_2\omega_2}{p_3 - n_2}t \right) + (p_3\delta_3 - n_2\delta_2) = D$$

$$(2.36)$$

Equation (2.35) then reduces to

$$B_r^1 B_\theta^{3,2} = \{M\cos A\}\times\{N\cos B + P(\cos C + \cos D)\}$$
$$= MN\cos A\cos B + MP\cos A\cos C + MP\cos A\cos D$$

$$(2.37)$$

where,

$$M = b_{r,1}^1(r)$$

$$N = \lambda_{\theta,0}^2(r)b_{\theta,1}^3(r)$$

$$P = \frac{\lambda_{\theta,1}^2(r)b_{\theta,1}^3(r)}{2}$$

$$(2.38)$$

Applying trigonometric identity (2.8) in (2.37) and simplifying, we obtain the following

cosine terms

$$\cos(A+B) = \cos\left[p_1\left(\theta - \omega_1 t\right) + p_1\delta_1 + p_3\left(\theta - \omega_3 t\right) + p_3\delta_3 \right] \tag{2.39}$$

$$\cos(A-B) = \cos\left[p_1\left(\theta - \omega_1 t\right) + p_1\delta_1 - p_3\left(\theta - \omega_3 t\right) - p_3\delta_3 \right] \tag{2.40}$$

$$\cos(A+C) = \cos\left[p_1\left(\theta - \omega_1 t\right) + p_1\delta_1 + \left(p_3 + n_2\right)\left(\theta - \frac{p_3\omega_3 + n_2\omega_2}{p_3 + n_2}t\right) + \left(p_3\delta_3 + n_2\delta_2\right) \right] \tag{2.41}$$

$$\cos(A-C) = \cos\left[p_1\left(\theta - \omega_1 t\right) + p_1\delta_1 - \left(p_3 + n_2\right)\left(\theta - \frac{p_3\omega_3 + n_2\omega_2}{p_3 + n_2}t\right) + \left(p_3\delta_3 + n_2\delta_2\right) \right] \tag{2.42}$$

$$\cos(A+D) = \cos\left[p_1\left(\theta - \omega_1 t\right) + p_1\delta_1 + \left(p_3 - n_2\right)\left(\theta - \frac{p_3\omega_3 - n_2\omega_2}{p_3 - n_2}t\right) + \left(p_3\delta_3 - n_2\delta_2\right) \right] \tag{2.43}$$

$$\cos(A-D) = \cos\left[p_1\left(\theta - \omega_1 t\right) + p_1\delta_1 - \left(p_3 - n_2\right)\left(\theta - \frac{p_3\omega_3 - n_2\omega_2}{p_3 - n_2}t\right) + \left(p_3\delta_3 - n_2\delta_2\right) \right] \tag{2.44}$$

Each of the terms in equations (2.39) to equation (2.44) contains both a time varying

term and a spatial θ term. In order to obtain the torque in the inner air gap using equation

(2.33), equation (2.37) needs to be integrated over the integral from 0 to 2π. The cosine

of the spatial θ term which when integrated from 0 to 2π will result in a zero average

torque. In order to create a non-zero torque, the angular θ dependent term in these

equations must be eliminated. For instance, if we consider (2.43), the angular dependent

term is eliminated when

$$p_3 - n_2 = -p_1$$

or,

$$n_2 = p_1 + p_3 \tag{2.45}$$

Evaluating all the equations from (2.39) to (2.44) will yield a zero average torque when integrated over integral 0 to 2π except equation (2.43) which will then reduce to

$$\cos(A+D) = \cos\left[-p_1\omega_1 t - p_1\left(-\frac{p_3\omega_3 - n_2\omega_2}{-p_1}t\right) + \left(p_3\delta_3 + p_1\delta_1 - n_2\delta_2\right)\right] \qquad (2.46)$$

To achieve a constant torque, the time varying terms in equation (2.46) must be zero. This requires

$$-p_1\omega_1 t - p_1\left(\frac{p_3\omega_3 - n_2\omega_2}{p_1}t\right) = 0 \qquad (2.47)$$

Further rearranging and simplifying gives,

$$\omega_1 = \frac{n_2}{p_1}\omega_2 - \frac{p_3}{p_1}\omega_3 \qquad (2.48)$$

Using the harmonic components, (2.48) can be expressed in the generalized form as

$$mp_1 = \left|kp_3 \pm jn_2\right| \qquad (2.49)$$

where, $\qquad m, k = 1, 3, 5, \ldots\infty$

$$j = 0, \pm 1, \pm 2, \ldots, \pm\infty \qquad (2.50)$$

Substituting (2.45) in (2.48), we can also write equation (2.48) as

$$\omega_1 = \frac{n_2}{n_2 - p_3}\omega_2 - \frac{p_3}{n_2 - p_3}\omega_3 \qquad (2.51)$$

Assuming there are no losses, the torque relation between rotors can be derived from conservation of power flow, given by

$$T_1\omega_1 + T_2\omega_2 + T_3\omega_3 = 0 \tag{2.52}$$

where, T_1, T_2 and T_3 are the torques on inner rotor, cage rotor and outer rotor respectively. When the cage rotor is held stationary, i.e. $\omega_2 = 0$, the speed ratio reduces to

$$\omega_1 = -\frac{p_3}{n_2 - p_3}\omega_3 \tag{2.53}$$

Substituting (2.53) in (2.52) and using $\omega_2 = 0$ the relation between inner rotor torque and outer rotor torque becomes

$$T_3 = \frac{p_3}{n_2 - p_3}T_1 \tag{2.54}$$

When the outer rotor is held stationary, i.e. $\omega_3 = 0$, the speed ratio reduces to

$$\omega_1 = \frac{n_2}{n_2 - p_3}\omega_2 \tag{2.55}$$

Substituting (2.55) in (2.52) and using $\omega_3 = 0$ the torque relation between inner rotor and cage rotor becomes

$$T_2 = -\frac{n_2}{n_2 - p_3}T_1 \tag{2.56}$$

If the poles are not slipping the speed relationships in (2.53) and (2.55) is always valid. The torque relationships in equation (2.54) and (2.56) are only valid when there are no losses. From (2.54) and (2.56) it is evident that the highest torque is obtained on the cage rotor when the outer rotor is stationary i.e. $\omega_3 = 0$ and $n_2 > p_3$. The relationship between torques on the three rotors is given by

$$T_1 + T_2 + T_3 = 0 \qquad (2.57)$$

This can be confirmed by substituting (2.54) and (2.56) in (2.57), which gives

$$T_1 + \left(-\frac{n_2}{n_2 - p_3} \right) T_1 + \left(\frac{p_3}{n_2 - p_3} \right) T_1 = 0 \qquad (2.58)$$

2.2   Flux Focusing Design of Magnetic Gears

The surface mounted magnet designs are used extensively for designing MGs used in various fields [44]. However, the flux focusing MG rotor design approach was chosen over the surface mounted magnet rotor design as the magnetic flux density in the air gap can be substantially increased by arranging the magnets in a flux focusing arrangement, also known as spoke type arrangement [38-41]. The increase in the magnetic flux concentration in the air gap for each rotor pole is due to two circumferentially magnetized PMs buried between the steel cores, contributing to the air gap flux instead of one. This arrangement is as shown in Figure 2-8 (a). The flux concentration of magnets onto the steel is as shown in Figure 2-8 (b). The increase in magnetic flux concentration at the air gap results in a higher torque output than a radially magnetized surface mounted rotor. With this arrangement, the permanent magnets are less likely to become demagnetized [17]. There are however, some disadvantages of using the flux focusing arrangement. This arrangement requires complicated construction

(a)   (b)
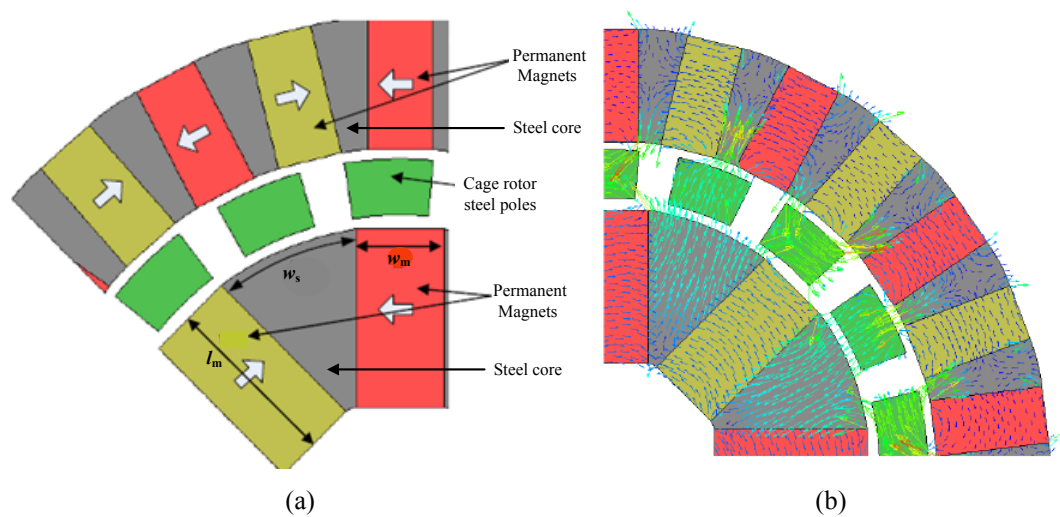
Figure 2-8: (a) Flux focusing arrangement of magnets and (b) flux concentrating on the steel [34]
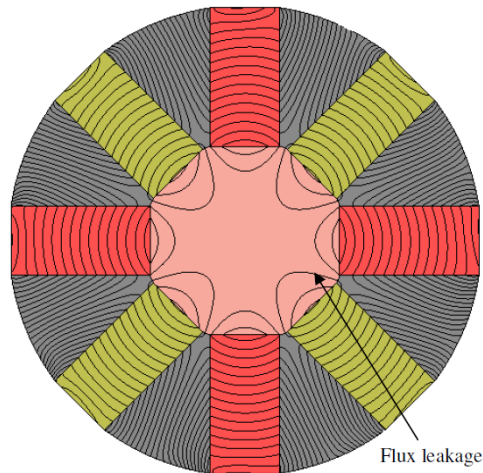
Figure 2-9: Leakage flux on the shaft of inner rotor
[34]

to reduce or eliminate the PM flux leakage, shown in Figure 2-9, in the radially inward direction on the inner rotor shaft of the MG. Another disadvantage is the complicated construction required to retain the PMs and the pole pieces in the rotor during normal operation [34]. The flux focusing design also tends to create higher order harmonics.

In this chapter, three different typological designs of an MG have been investigated. These are the flux focusing design with the cage rotor as the intermediate rotor, flux focusing design with the cage rotor as the outer rotor and the flux focusing MG design with consequent poles on the outer rotor. In section 2.2.1, an initial study of the baseline flux focusing MG design has been conducted, followed by its idealized design in section 2.2.2. The gear ratio used for both the baseline and idealized design was 4.25:1. The study was conducted further on an idealized design with a gear ratio of 8.5:1. In section 2.2.3, the outer cage rotor flux focusing design was investigated for gear ratios of 4.25:1 and 8.5:1. The consequent pole design was studied in section 2.2.4.

2.2.1 The Baseline Flux Focusing Design

As the name suggests, the baseline flux focusing design serves as the starting point of all other MG designs studied in this chapter. The 2D model of the baseline flux focusing design is shown in Figure 2-10. As the primary aim of studying this design was to maximize the volume torque density, the inner radius of the inner rotor was kept small. The smaller inner radius design results in the inner rotor magnets being radially thicker, than needed. Rectangular magnets were used to reduce the manufacturing cost and additional steel pole lips were used to retain the magnets in place. The exploded view of the mechanical assembly, the rotor assemblies and the test set up for the baseline design are shown in Figure 2-11 and Figure 2-12. The geometric parameters for the simulation of this baseline flux focusing design, are specified in Table 2.1.

. In order to simulate the design, the angular velocities of the three rotors were calculated at first, the relationship between which can be obtained from (2.51). To achieve the highest torque, the outer rotor is held stationary i.e. $\omega_3 = 0$. With $\omega_3 = 0$ and putting (2.45) in (2.51) we obtain,

$$\omega_1 = \frac{n_2}{p_1}\omega_2 = G_{12}\omega_2 \tag{2.59}$$

where, G_{12} is the gear ratio. Using the geometric properties mentioned in Table 2.1.

, the gear ratio obtained is $G_{12} = 4.25$.
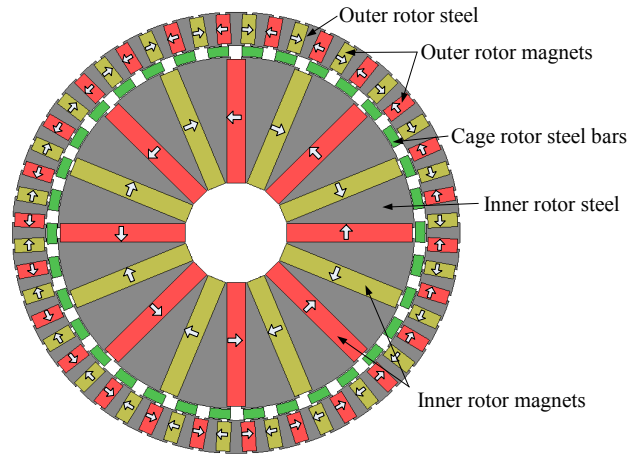
Figure 2-10: 2D baseline flux focusing MG using JMAG [34]
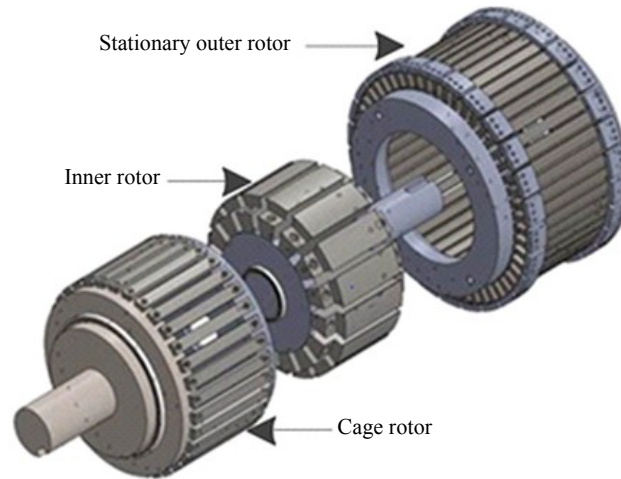
Figure 2-11: Exploded view of the mechanical assembly [34]
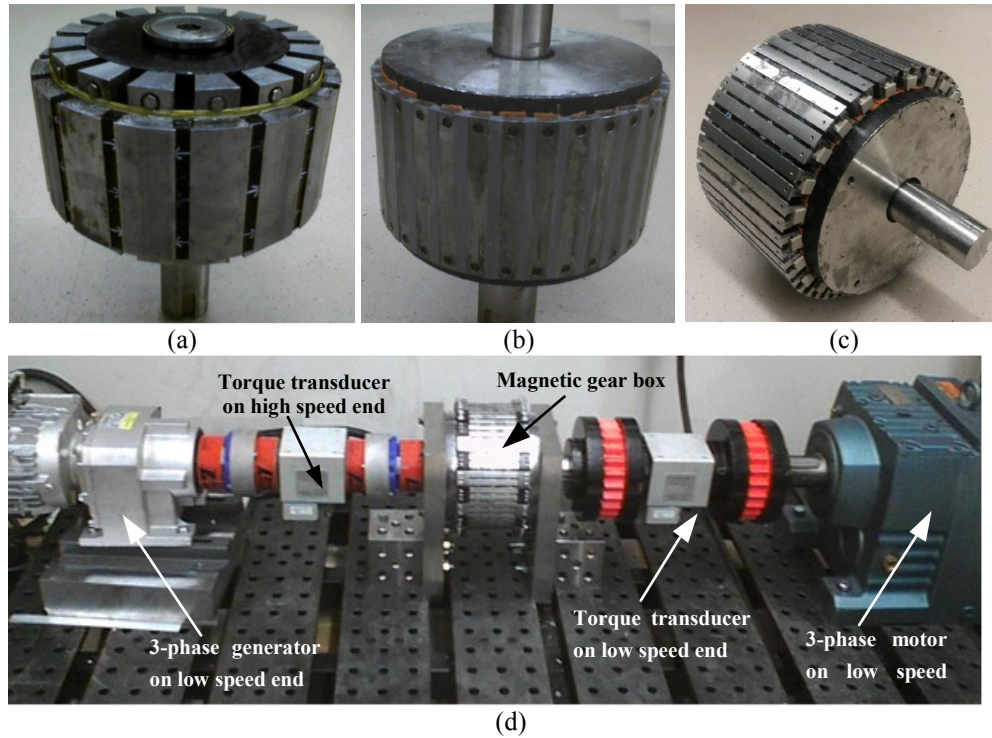
Figure 2-12: (a) Inner rotor assembly, (b) cage rotor assembly with inner rotor, (c) complete assembly and (d) test bench setup [34]

TABLE 2.1.
GEOMETRIC PARAMETERS AND MATERIAL PROPERTIES OF THE
BASELINE DESIGN

	Description	Value	Unit
Inner rotor (high speed)	Pole pairs, p_1	8	-
	Inner radius, r_{i1}	26	mm
	Outer radius, r_{o1}	92	mm
	Width of magnets, w_{m1}	9.5	mm
	Steel pole span, θ_{s1}	$\pi/(2p_1)$	radians
Cage rotor (low speed)	Steel bars, n_2	34	-
	Steel bar thickness, l_2	5	mm
	Steel bar span, θ_{s2}	$2\theta_{s2}$	degrees
Outer rotor (stationary)	Pole pairs, p_3	26	-
	Inner radius, r_{i3}	98	mm
	Width of magnets, w_{m3}	3	mm
	Outer radius with lips, r_{o3}	114	mm
	Steel pole span, θ_{s3}	$\pi/(2p_3)$	radians
Material	416 steel resistivity	57	μΩ-cm
	1018 steel resistivity	15.9	μΩ-cm
	416 steel density, ρ_s	7850	kg/m3
	1018 steel density, ρ_s	7850	kg/m3
	NdFeB magnet density, ρ_m	7600	kg/m3

Air gap, g	0.5	mm
Thickness of steel lips	1	mm
Stack length, d	75	mm
Gear ratio	4.25	-

The 2-D FEA calculated torque obtained as a function of the low speed rotor angle is shown in Figure 2-13. It is evident from Figure 2-13 that a low torque ripple of 2 Nm exists on each of the high speed and the low speed rotor. The torque ripple on the low speed rotor is 0.25% and that on high speed rotor is 1% of their respective steady state torques. The torque and torque density values are summarized in Table 2.1. The formulae used to calculate the torque density values are mentioned in (2.65), (2.66) and (2.67). Although the design parameters chosen produced a significant volume torque density, the mass torque density and the torque per kg magnet mass are quite low. The design is further modified in the next section in order to improve the torque densities.
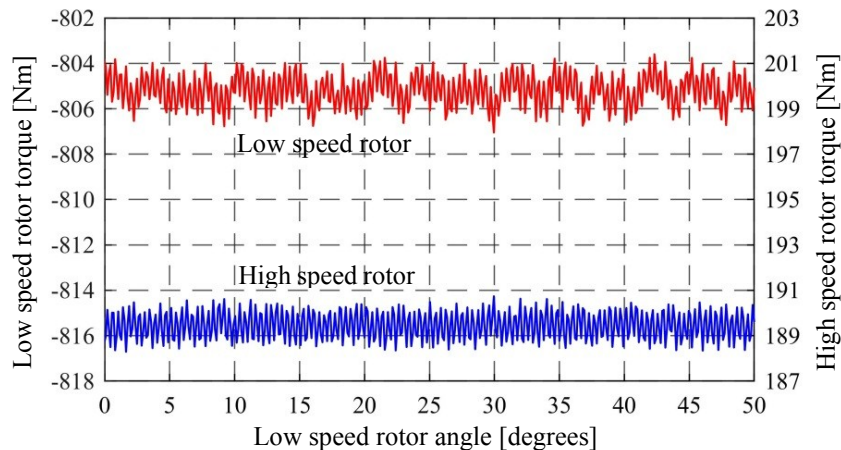
Figure 2-13: Torque at peak torque angle for baseline flux focusing design

TABLE 2.1.

2D FEA CALCULATED TORQUE AND
TORQUE DENSITY VALUES

	Description	Values	Units
Average torque	Inner rotor	189	Nm
	Cage rotor	805	Nm
	Outer rotor	616	Nm
Volume torque density		262	Nm/L
Mass torque density		41	Nm/kg
Torque per kg magnet mass		88	Nm/kg

2.2.2 The Idealized Flux Focusing Design

An idealized version of the baseline flux focusing design is shown in Figure 2-14. The idealized design is used as the basis for all the other designs which were developed by incorporating structural and geometric parameter changes in the idealized design. The idealized design, shown in Figure 2-14 is obtained by replacing the rectangular magnets of the baseline design by angular ones and removing the steel pole lips. This was done in an attempt to simplify the designs for further study. In this section, the idealized designs with two different gear ratios have been studied, the 4.25:1 and 8.5:1gear ratio.

2.2.2.1 Geometric Parameter Definition and Material Properties

The geometric parameter definitions used in the flux focusing idealized design are illustrated in Figure 2-15. The inner rotor of the MG consists of p_1 pole pairs and the same number of steel poles segments as the number of magnets.
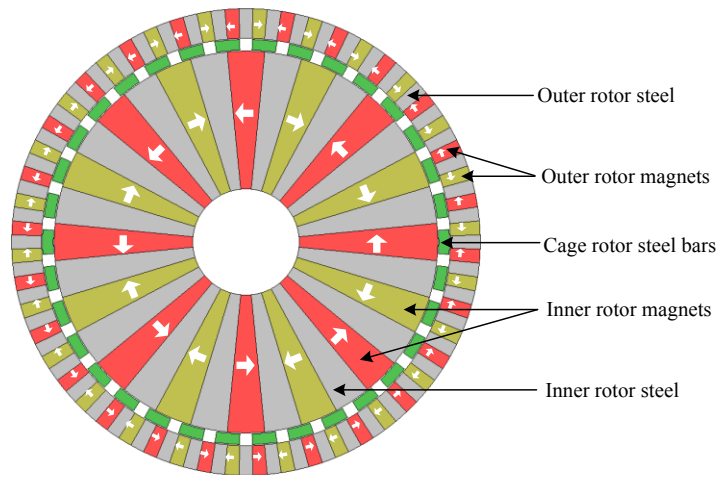
Figure 2-14: A 4.25:1 Idealized model before optimization

The angular spans for the steel poles, θ_{s1}, and magnets θ_{m1} are defined as

$$\theta_{s1} = \frac{\pi}{2p_1} \tag{2.60}$$

$$\theta_{s1} = \theta_{m1} \tag{2.61}$$

The outer rotor of the MG contains p_3 pole pairs and an equal number of steel segments. The steel segment angular span, θ_{s3}, and magnet span, θ_{m3} for outer rotor are defined as

$$\theta_{s3} = \frac{\pi}{2p_3} \tag{2.62}$$

$$\theta_{s3} = \theta_{m3} \tag{2.63}$$

The span of the cage rotor steel pieces is defined as

$$\theta_{s2} = 2\theta_{s3} \tag{2.64}$$
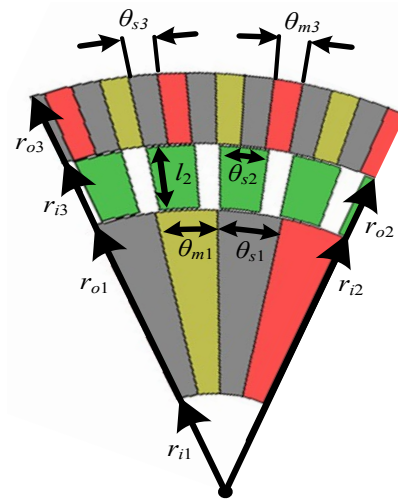
Figure 2-15: Geometric parameter definition

The volume torque density T_v has been calculated using

$$T_v = \frac{T_2}{\pi r_{o3}^2 d}$$

(2.65)

where, d is the axial length of the MG, T_2 is the torque obtained on the cage rotor and r_{o3} is the outer radius of the outer rotor of the MG.

The mass torque density T_m is computed by

$$T_m = \frac{T_2}{\left[\rho_s\left[\pi\left(r_{o2}^2 - r_{i2}^2\right)\right] + (\rho_s + \rho_m) \times 0.5\left[\pi\left\{\left(r_{o3}^2 - r_{i3}^2\right) + \left(r_{o1}^2 - r_{i1}^2\right)\right\}\right]\right]d}$$

(2.66)

where, ρ_s is the density of the steel and ρ_m is the density of the magnet used, r_{i1} and r_{o1} are respectively the inner and the outer radii of the inner rotor of the MG; r_{i3} is the inner radius of the outer rotor of the MG, defined in Figure 2-15.

The torque per kilogram of magnet mass is computed by using

$$T_{mm} = \frac{T_2}{\rho_m \left[\pi \left\{ \left(r_{o3}^2 - r_{i3}^2 \right) + \left(r_{o1}^2 - r_{i1}^2 \right) \right\} \right] d \times 0.5} \tag{2.67}$$

2.2.2.2 A 4.25:1 Idealized Flux Focusing Design

The 4.25:1 idealized flux focusing design is shown in Figure 2-14. The design has the same number of pole pairs as the baseline design. The modified geometric parameters are specified in Table 2.2. The change in the rotor radii values could be attributed to the removal of the steel pole lips and keeping the radial thickness of the magnets and the steel segments the same as the baseline design. This reduced the outer radius of the outer rotor to 110 mm when the inner radius of the inner rotor was kept fixed at 26 mm. To obtain the peak torque, the cage rotor was initially rotated, keeping the inner rotor and the outer rotor fixed. The pole slipping torque obtained as a function

of the low speed rotor angle is shown in Figure 2-16. The cage rotor was rotated to an

angular position where the peak torque can be achieved, keeping the positions of the

inner and the outer rotor unaltered. To obtain a steady state peak torque, the inner rotor

and the cage rotor were rotated at speeds conforming to (2.3.2). The steady state torque

obtained as a function of the low speed rotor angle is shown in Figure 2-17. The 2-D FEA

calculated torque and torque density values are as shown in Table 2.3.

TABLE 2.2
ROTOR RADII FOR SIMULATING 4.25:1 IDEALIZED DESIGN

	Description	Value	Unit
Inner rotor (high speed)	Inner radius, r_{i1}	26	mm
	Outer radius, r_{o1}	90	mm
	Pole span, θ_{s1}	$\pi/(2p_1)$	radians
Cage rotor (low speed)	Inner radius, r_{i2}	90.5	mm
	Outer radius, r_{o2}	95.5	mm
	Pole span, θ_{s2}	$2\theta_{s3}$	degrees
Outer rotor (stationary)	Inner radius, r_{i3}	96	mm
	Outer radius, r_{o3}	110	mm
	Pole span, θ_{s3}	$\pi/(2p_3)$	radians
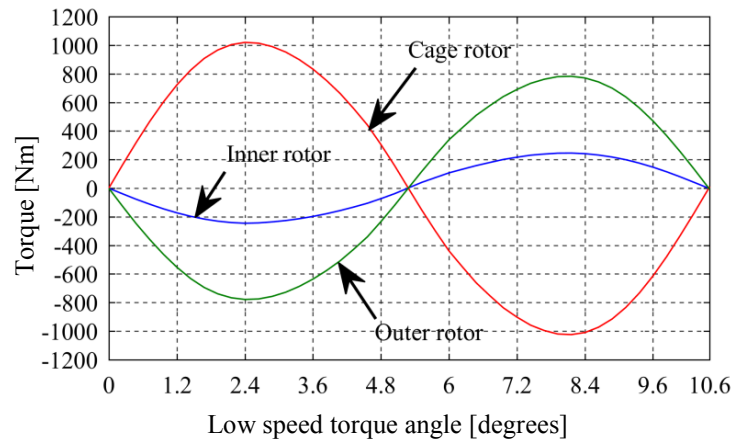
Figure 2-16: Pole slipping torque for 4.25 to 1 idealized design
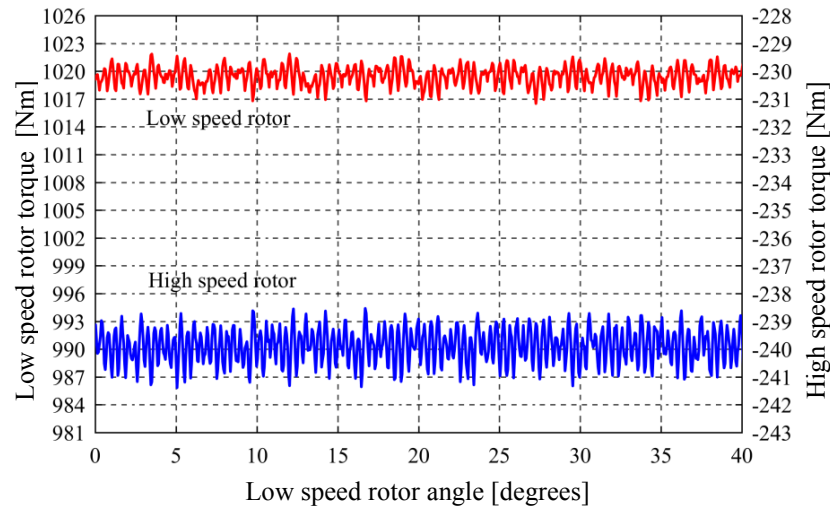
Figure 2-17: Torque at peak torque angle for idealized 4.25 to flux focusing design without optimization

TABLE 2.3.
2D FEA CALCULATED TORQUE AND
TORQUE DENSITY VALUES FOR BASELINE DESIGN

	Description	Value	Unit
	Inner rotor	240	Nm
Average torque	Cage rotor	1019	Nm
	Outer rotor	778	Nm
Volume torque density		357	Nm/L
Mass torque density		51	Nm/kg
Torque per kg magnet mass		110	Nm/kg

Comparing Table 2.1 and Table 2.3 it is evident that the peak torque values of the baseline and the idealized design differ by 214 Nm. The increase in the torque of the idealized design is due to the removal of the steel pole lips and replacing rectangular magnets by angular ones. To maximize the torque density of the idealized design, a geometric parameter sweep analysis was conducted. The flow of the sweep analysis is depicted in Figure 2-18. The sweep analysis was initiated by fixing the inner radius of the high speed inner rotor was at $r_{i1} = 25$ mm and the outer radius of the stationary outer rotor at $r_{o3} = 110$ mm. The outer radius of the inner rotor, r_{o1}, and the inner radius of the cage rotor r_{i2} were also kept fixed at 80 mm and 80.5 mm respectively. The thickness of the
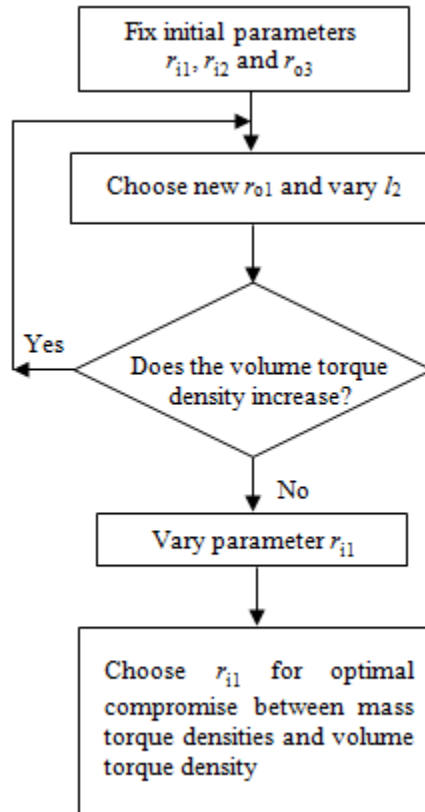
Figure 2-18: Flowchart for geometric parameter sweep analysis of idealized MG

cage rotor, l_2 was varied from 5 mm to 13 mm in the radially outward direction with an increment of 2 mm in each step. The outer radius of the inner rotor, r_{o1} = 80 mm, was increased by 2 mm until r_{o1} = 90 mm. The parameters producing the peak volume torque density were chosen for further analysis. The variation of volume torque density versus the mass torque density and torque per kg magnet mass are shown in Figure 2-19 (a) and (b) respectively. The point marked with a red dot in these figures refers to the peak torque density point and the corresponding geometric parameters (r_{i1}, r_{o1}, l_2) = (25,88,9) are selected for further sweep analysis. The inner radius of the inner rotor r_{i1} was varied from 25 mm to 70 mm with an increase of 5 mm in each step. Figure 2-20(a) shows the plot of the volumetric torque density versus the mass torque density when r_{i1} is varied. The

variation of volume torque density versus the torque per kg magnet mass and torque are plotted in Figure 2-20(b) and (c) respectively. The final parameters were chosen such that the mass torque density and the torque per kg magnet mass are compromised only by a small value of 8 Nm/kg and 30 Nm/kg respectively. The point marked with a red dot represents the torque densities of the final parameters chosen for final simulation. The final parameter values are specified in Table 2.4. The final design for simulation is shown in Figure 2-21. The torque simulated using 2D FEA is shown in Figure 2-22 as a function of the low speed rotor angle.
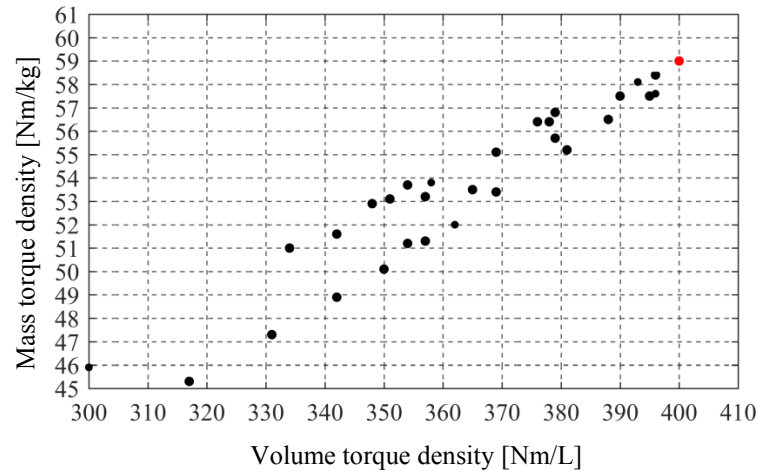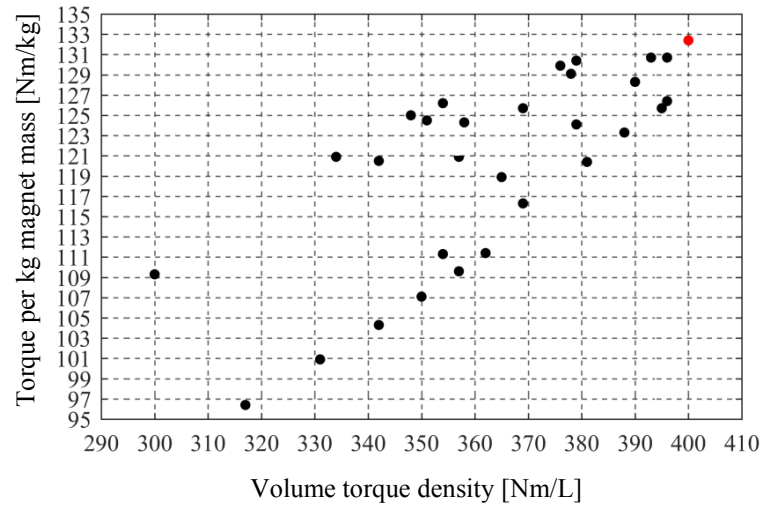
Figure 2-19: The volumetric torque density versus (a) the mass torque density and (b) torque per kg magnet mass when l_2 and r_{o1} are varied
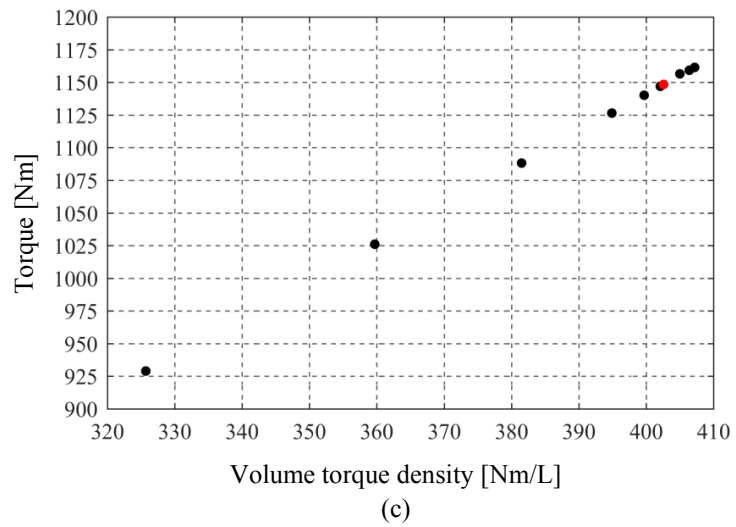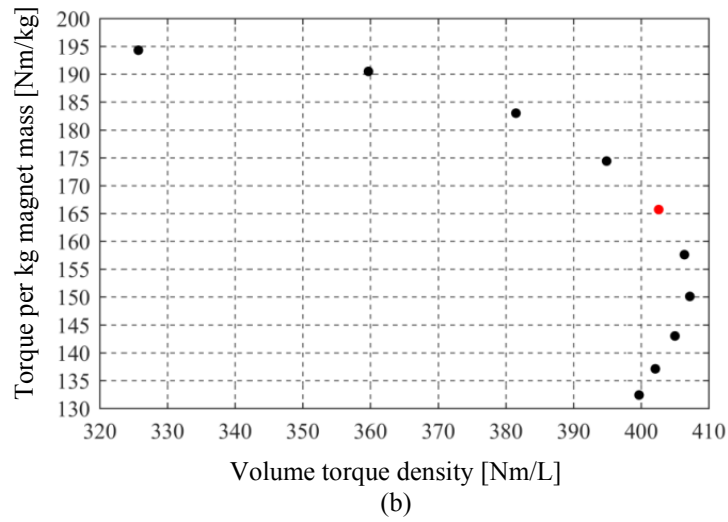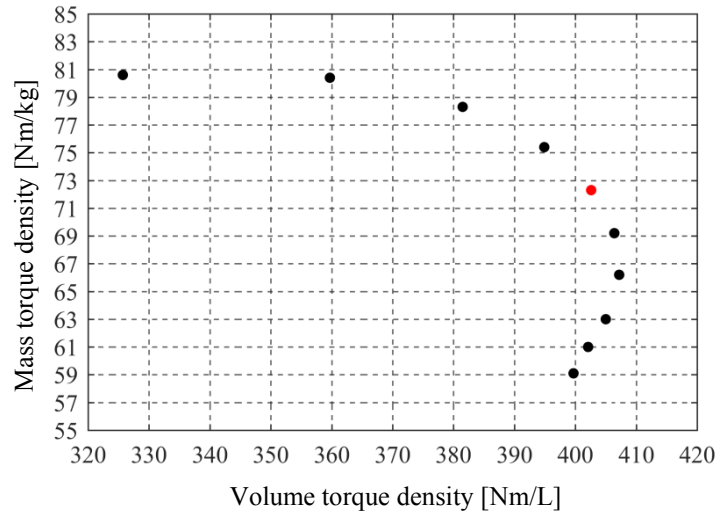
Figure 2-20: The volumetric torque density versus (a) the mass torque density, (b) torque per kg magnet mass and (c)torque when r_{i1} is varied

TABLE 2.4
FINAL GEOMETRIC PARAMETERS FOR SIMULATING
4.25:1 IDEALIZED DESIGN

	Description	Value	Unit
Inner rotor (high speed)	Inner radius, r_{i1}	50	mm
	Outer radius, r_{o1}	88	mm
Cage rotor (low speed)	Inner radius, r_{i2}	88.5	mm
	Outer radius, r_{o2}	97.5	mm
Outer rotor (stationary)	Inner radius, r_{i3}	98	mm
	Outer radius, r_{o3}	110	mm
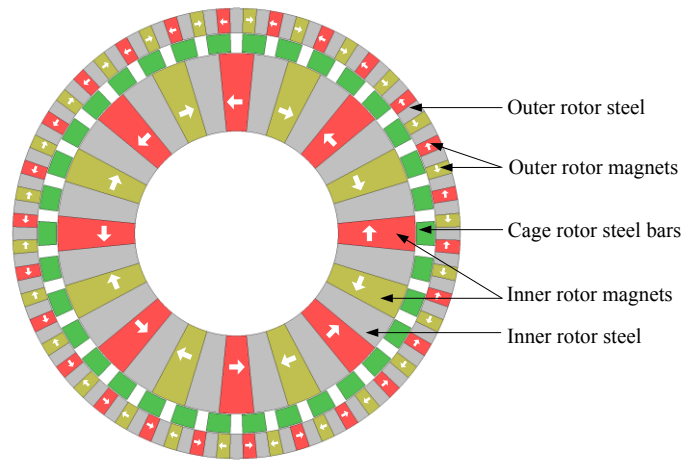
Figure 2-21: Idealized 4.25:1 gear ratio flux focusing MG after optimization
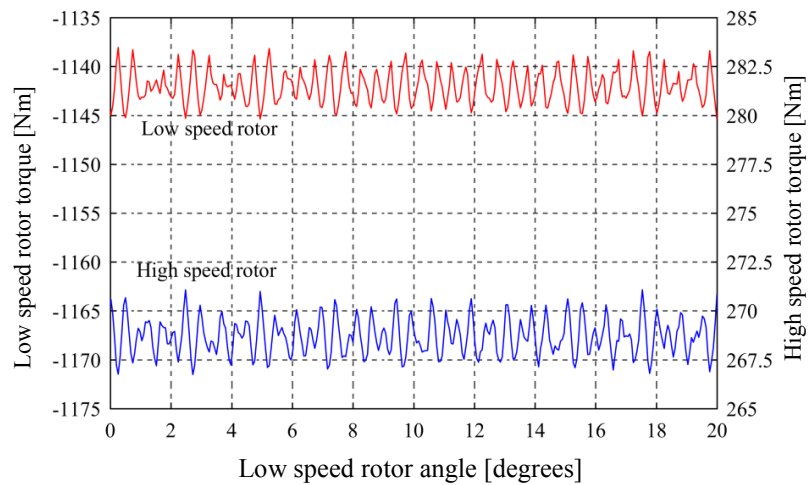
Figure 2-22: Steady state peak torque for idealized 4.25:1 flux focusing MG

A comparison between the baseline, and the idealized designs both before and after the parameter sweep analysis, is shown in Table 2.5. It shows that the volume torque density increased by 36% from the baseline design to the ideal design and by 53% to the maximized ideal design. The increase for the mass torque density was 24% from the baseline design to the ideal design and by 78% to the maximized design. The corresponding increase in torque per kg magnet mass for idealized design without and with maximization is by 25% and 87.5% respectively.

TABLE 2.5.
COMPARISON OF TORQUE AND TORQUE DENSITY VALUES OF
BASELINE AND IDEALIZED DESIGNS

	Description	Baseline values	Ideal values	Maximized Ideal values	Units
Average torque	Inner rotor	189	240	268	Nm
	Cage rotor	805	1019	1142	Nm
	Outer rotor	616	778	874	Nm
Volume torque density		262	357	403	Nm/L
Mass torque density		41	51	73	Nm/kg
Torque per kg magnet mass		88	110	165	Nm/kg

2.2.2.3   A 8.5:1 Idealized Flux Focusing Design

In this section an idealized flux focusing MG designed with a higher gear ratio of 8.5:1 has been studied. A higher gear ratio MG produces higher speed and lower torque on the input rotor compared to its lower gear ratio counterpart. To achieve this gear ratio, the pole combination was selected to be $(p_1, n_2, p_3) = (4,34,30)$. An 8.5:1 idealized flux focusing design is as shown in Figure 2-23. A parametric sweep analysis of the geometry of the design was conducted to maximize the torque and the torque density of the MG. The same sweep analysis technique as adopted for the 4.25:1 gear ratio design has been used. Figure 2-24 (a) shows the variation of the mass torque density versus the volume torque density when the cage rotor thickness l_2 and outer radius of inner rotor r_{o1} were varied. The variation of the torque per kg magnet mass versus the volume torque density is shown in Figure 2-24 (b). The point marked with a red dot represents the peak volume torque density point. The corresponding geometric parameters $(r_{o1}, l_2) = (85,9)$ mm were selected for further sweep analysis.
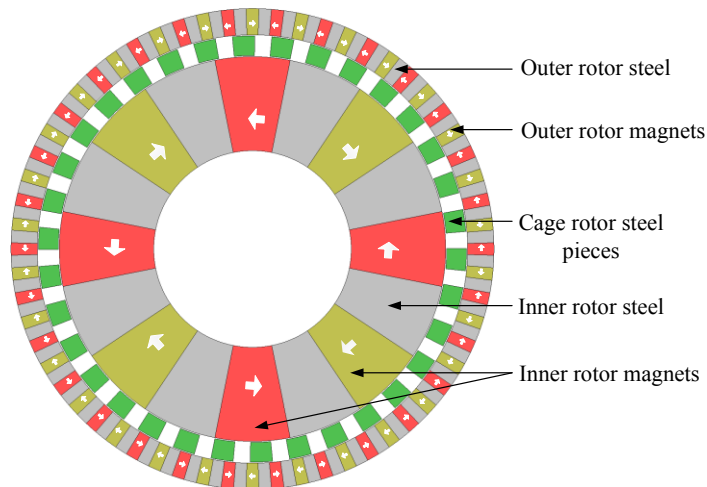
Figure 2-23: Idealized 8.5:1 gear ratio flux focusing MG

Figure 2-25(a) shows the plot of the volumetric torque density versus the mass torque density when r_{i1} is varied. The variation of the volume torque density with torque per kg magnet mass is shown in Figure 2-25(b) and Figure 2-25(c) shows the corresponding variation of the volume torque density with torque. The final geometric parameters chosen were $(r_{i1}, r_{o1}, l_2) = (45, 88, 9)$ mm. The corresponding torque densities are marked in red in each of these figures. The final parameter values are summarized in Table 2.6. Table 2.7. shows the calculated torque and torque density values.
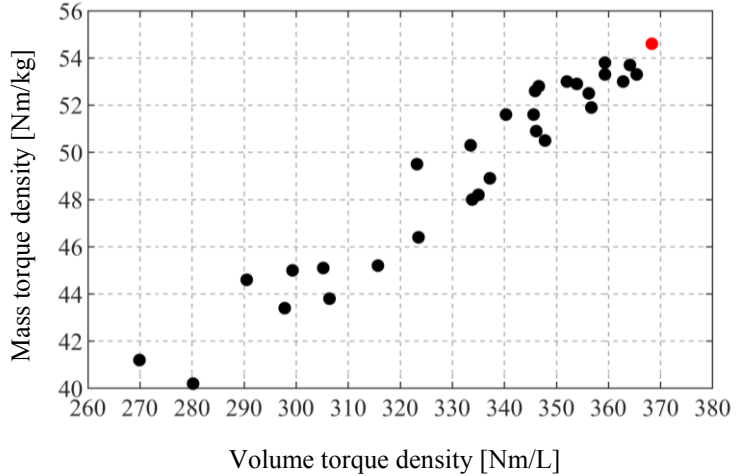
(a)
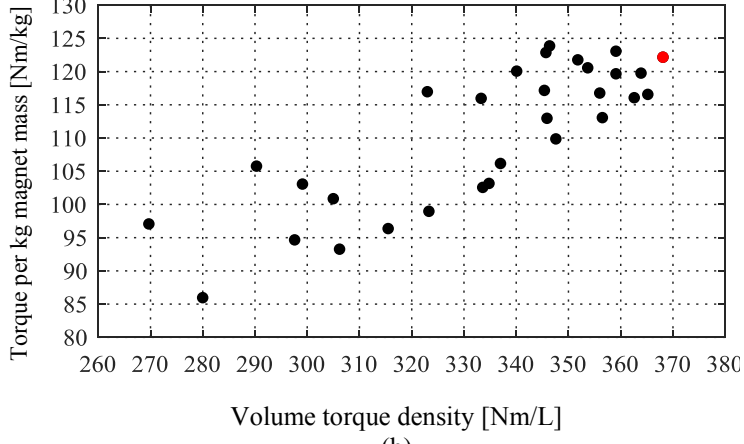
(b)

Figure 2-24: The volumetric torque density versus (a) the mass torque density and (b) torque per kg magnet mass when l_2 and r_{o1} are varied
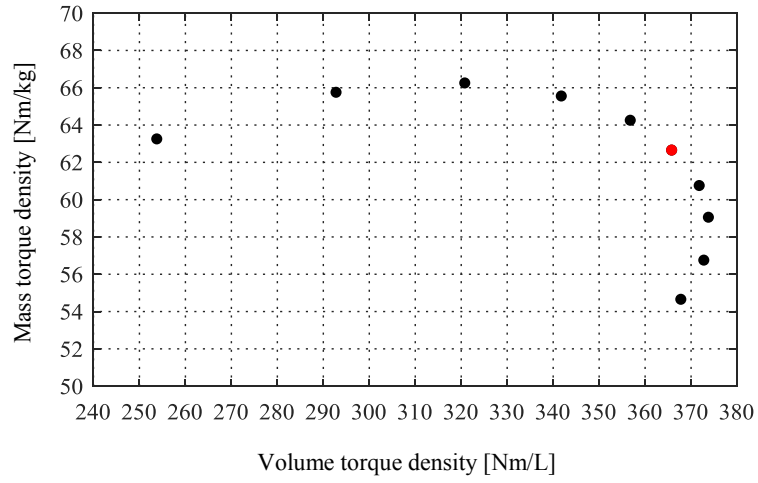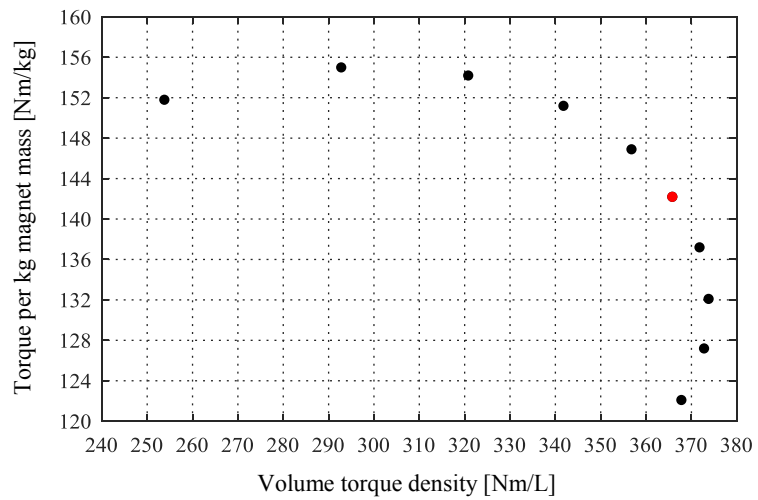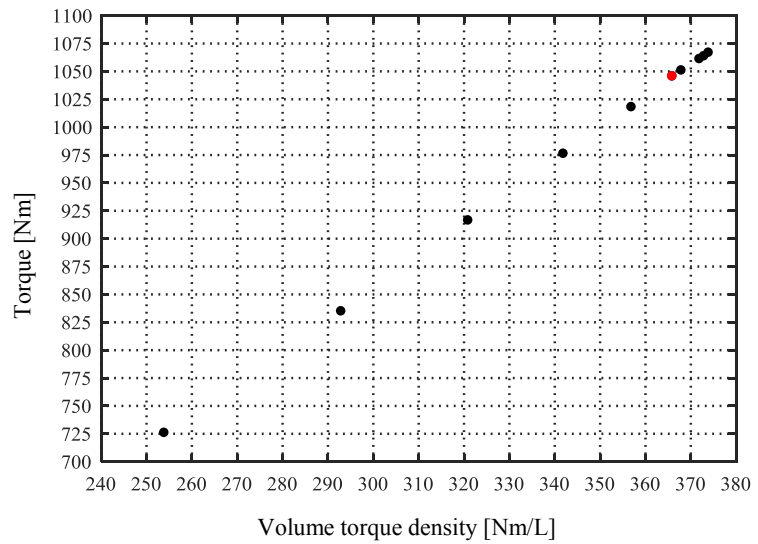
Figure 2-25: The volumetric torque density versus (a) the mass torque density, (b) torque per kg magnet mass and (c) torque when r_{i1} is varied

TABLE 2.6
FINAL GEOMETRIC PARAMETERS FOR 2D FEA ANALYSIS OF 8.5:1MG

	Description	Value	Unit
Inner rotor (high speed)	Inner radius, r_{i1}	45	mm
	Outer radius, r_{o1}	88	mm
	Pole span, θ_{s1}	$\pi/(2p_1)$	radians
Cage rotor (low speed)	Cage bar thickness, l_2	9	mm
	Pole span, θ_{s2}	$2\theta_{s3}$	degrees
Outer rotor (stationary)	Inner radius, r_{i3}	98	mm
	Outer radius, r_{o3}	110	mm
	Pole span, θ_{s3}	$\pi/(2p_3)$	radians
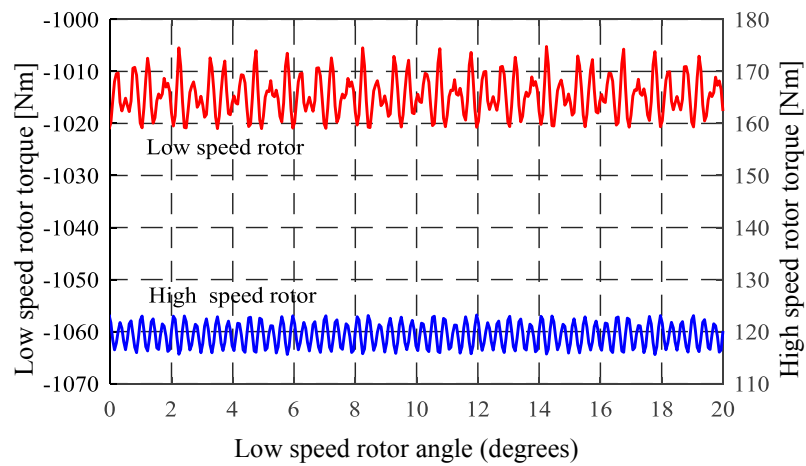
Figure 2-26: Torque for idealized 8.5:1 gear ratio flux focusing MG

TABLE 2.7.
2D FEA CALCULATED TORQUE AND TORQUE
DENSITY VALUES

	Description	Value	Units
Average torque	Inner rotor	118	Nm
	Cage rotor	1017	Nm
	Outer rotor	880	Nm
Volume torque density		366	Nm/L
Mass torque density		62	Nm/kg
Torque per kg magnet mass		142	Nm/kg

A comparative analysis between the performance of the 8.5:1 idealized MG design and 4.25:1 idealized MG design is presented in Table 2.8. It can be noted that a high torque can still be obtained when using a relatively high gear ratio without degrading the torque density significantly.

TABLE 2.8.
COMPARISON BETWEEN 4.25:1 AND 8.5:1 IDEALIZED DESIGNS

Description		Value		Unit
		4.25:1	8.5:1	
Average torque	Inner rotor	268	118	Nm
	Cage rotor	1142	1017	Nm
	Outer rotor	874	880	Nm
Volume torque density		403	336	Nm/L
Mass torque density		73	62	Nm/kg
Torque per kg magnet mass		165	142	Nm/kg

2.2.3 Flux Focusing Magnetic Gear Design with an Outer Cage Rotor

A second type of design approach has been used in this section wherein, the cage rotor steel pieces are used as the outermost rotor. The main purpose of studying this design is that, the cage rotor in the outermost region can be modified into a stator, and the MG can be made to work as an MGM. To achieve this design, the cage rotor and the outer rotor positions in the previous designs are interchanged. The outer rotor in previous designs acts as the as the intermediate rotor. Figure 2-27 shows such a design. The inner rotor has p_1 pole pairs, the intermediate rotor has p_2 pole pairs and the cage rotor has n_3 steel bars. The relation among the speed of the three rotors is governed by (2.69). The outer cage rotor with n_3 steel pieces is stationary whereas, the intermediate rotor and the inner rotor are rotating.
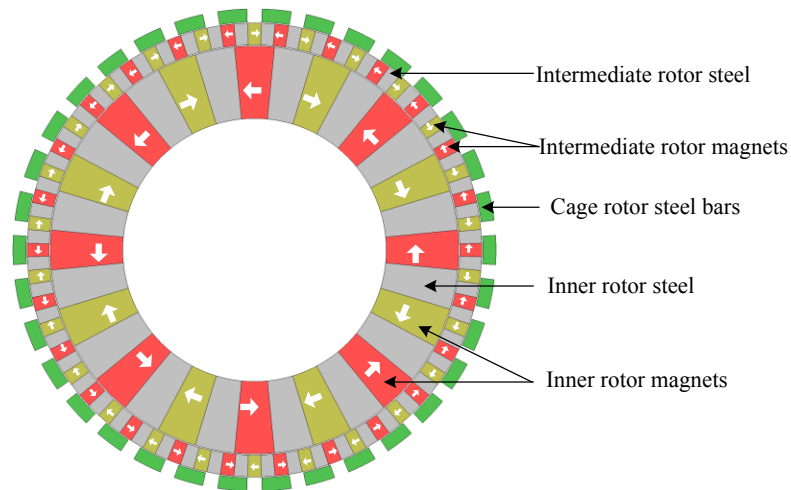
Figure 2-27: A 3.25:1 gear ratio outer cage rotor flux focusing MG

With $\omega_3 = 0$ used in (2.68) the speed relation among the three rotors becomes (2.69).

$$\omega_1 = \frac{n_3}{n_3 - p_2}\omega_3 - \frac{p_2}{n_3 - p_2}\omega_2 \qquad (2.68)$$

$$\omega_1 = -\frac{p_2}{p_1}\omega_2 = -G_{12}\omega_2 \qquad (2.69)$$

where, G_{12} is the gear ratio.

A 3.25:1 outer cage rotor MG design shown in Figure 2-27 has the same number of pole pair as the flux focusing design shown in Figure 2-21 but the cage rotor and the outer rotor positions are interchanged. Thus, the number of pole pairs on the inner rotor and the intermediate rotor are $p_1 = 8$ and $p_2 = 26$ and the number of steel pieces on the outer cage rotor is $n_3 = 34$. Using (2.69), this gives a gear ratio $G_{12} = 3.25:1$. A parametric sweep analysis has been conducted to maximize the torque density. The geometric parameter definition for the sweep analysis is shown in Figure 2-30 and the same procedure as described in Figure 2-18 has been implemented. The inner and the outer radii of the MG were fixed initially at $r_{i1} = 25$ mm and $r_{o3} = 110$ mm.
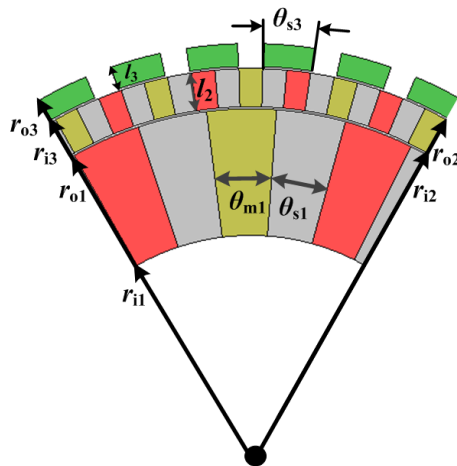
Figure 2-28: Geometric parameter definition of outer cage rotor MG design

The plot of the mass torque density and torque per kg magnet mass versus the volume torque density when r_{o1} and l_2 are varied are shown in Figure 2-29. The parameters values chosen for further sweep analysis were $(r_{o1}, l_2) = (93,10)$ mm. These values produced the maximum volume torque density marked in red. The variation of mass torque density, torque per kg magnet mass and torque when r_{i1} is varied are plotted in Figure 2-29. The final geometric parameters $(r_{i1}, l_2, l_3) = (60,10,6)$ mm are chosen at a volume torque density of 142 Nm/L. Table 2.9 summarizes the final geometric parameters.
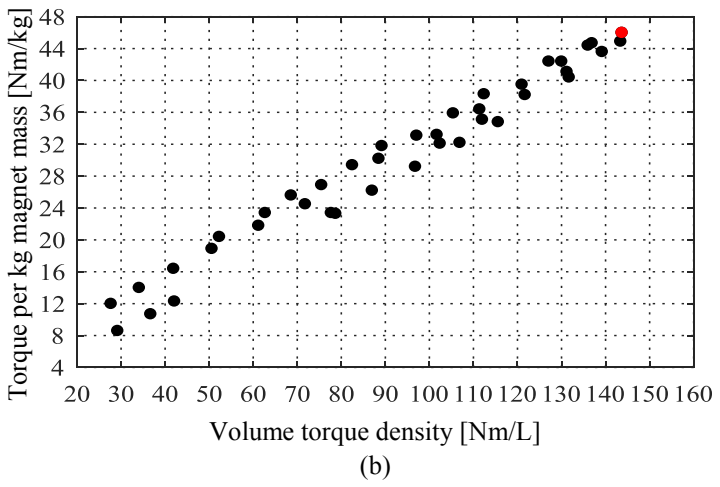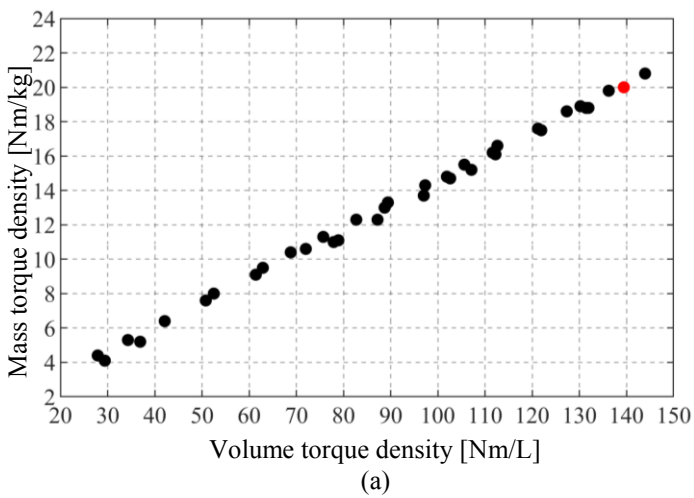
Figure 2-29: Volume torque density versus (a) mass torque density and (b) torque per kg magnet mass when l_2 and r_{o1} are varied
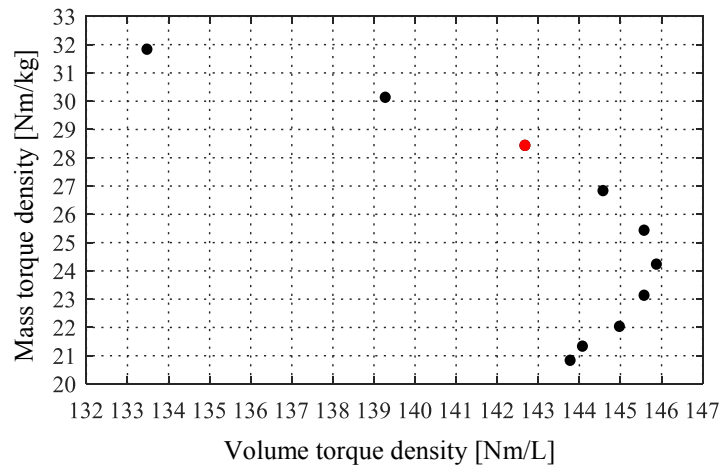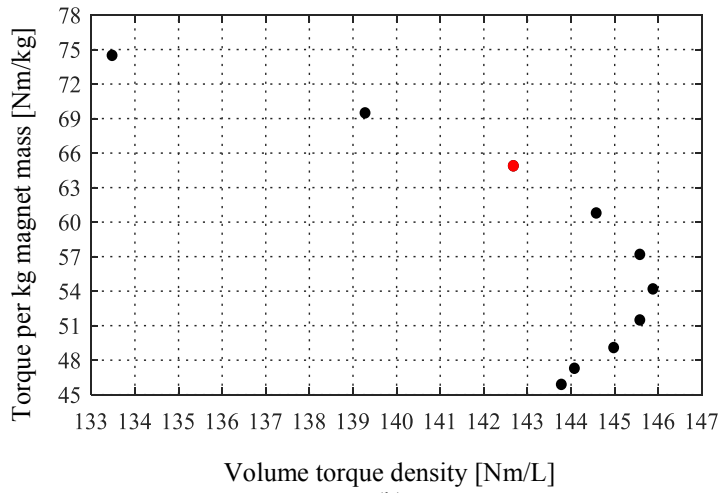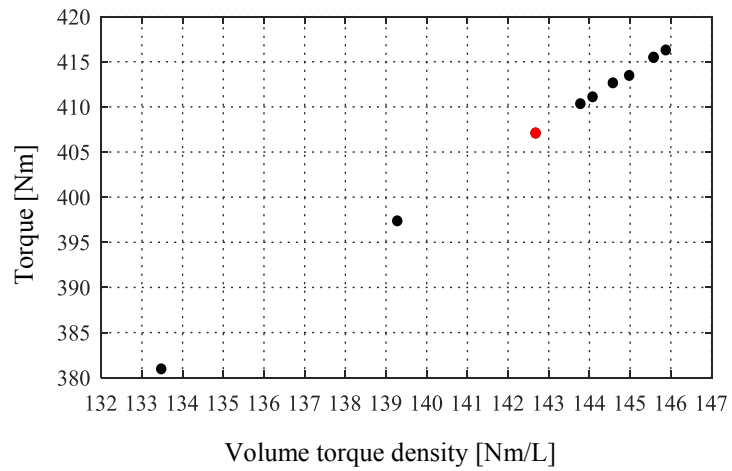
Figure 2-30: Volume torque density versus (a) mass torque density (b) torque per kg magnet mass and (c) torque when r_{i1} is varied

TABLE 2.9.
INNER AND OUTER RADII OF THE THREE ROTORS

	Description	Value	Unit
Inner Rotor	Inner radius, r_{i1}	60	mm
	Outer radius, r_{o1}	93	mm
Intermediate Rotor	Inner radius, r_{i2}	93.5	mm
	Outer radius, r_{o2}	103.5	mm
Cage rotor	Inner radius, r_{i3}	104	mm
	Outer radius, r_{o3}	110	mm

The design is simulated using 2D FEA, the steady state torque obtained as a function of low speed rotor angle is shown in Figure 2-31. The calculated torque and torque densities are summarized in Table 2.10. When compared with the 4.25:1 baseline design, the torque generated by the 3.25:1 outer cage rotor design seems to have decreased significantly.
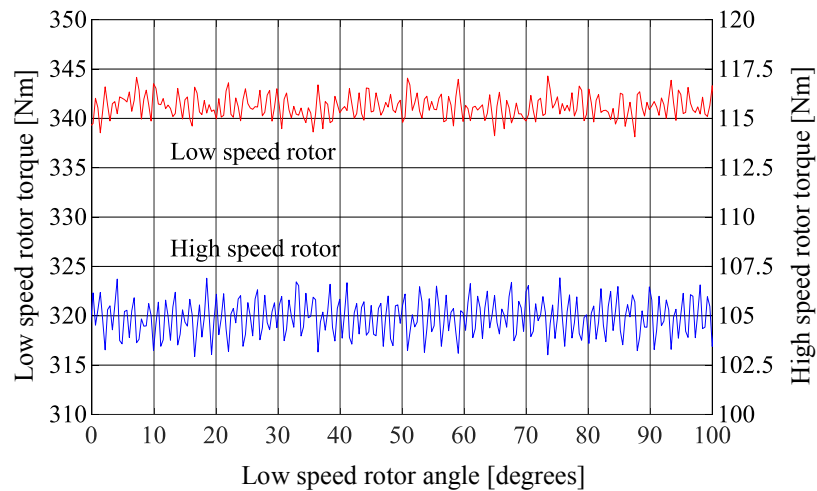
Figure 2-31: Torque for 3.25:1 gear ratio outer cage rotor flux focusing MG

TABLE 2.10
TORQUE AND TORQUE DENSITY VALUES OF AN OUTER CAGE ROTOR
MG DESIGN 3.25:1 GEAR RATIO

	Description	Value	Unit
	Inner rotor	103	Nm
Average torque	Intermediate rotor	344	Nm
	Cage rotor	449	Nm
Volume torque density		121	Nm/L
Mass torque density		25	Nm/kg
Torque per kg magnet mass		54	Nm/kg

A 7.5:1 flux focusing MG with an outer cage rotor is shown in Figure 2-32. The number of pole pairs on the inner rotor, intermediate rotor and the outer rotor is (p_1, p_2, n_3) = (4,30,34). The inner rotor and the outer cage rotor steel segments are rotating at a speed governed by (2.69), giving a gear ratio of G_{12} = 7.5:1. The torque density of the design is maximized by using the same technique as used for the 3.25:1 outer cage rotor design. The variation of the mass torque density and torque per kg magnet mass with the variation of the volume torque density is as shown in Figure 2-33.
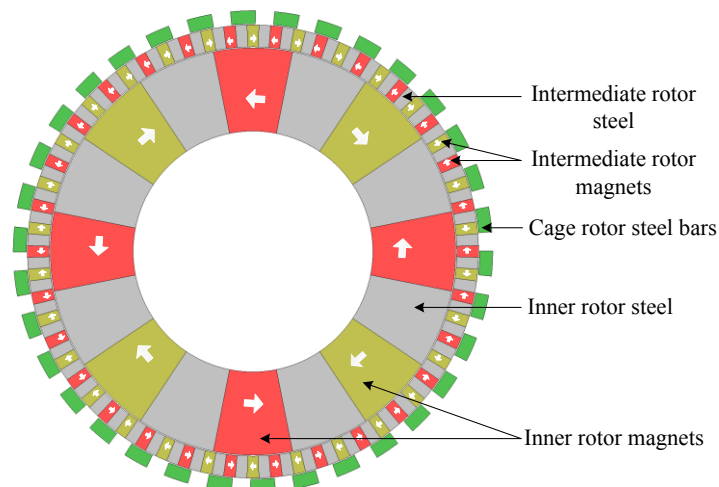
Figure 2-32. A 7.5:1 gear ratio outer cage rotor flux focusing MG

The parameters which produced the maximum volume torque density when r_{o1} and l_2 were varied were $(r_{i1}, r_{o1}, l_2) = (25, 93, 10)$ mm. The torque densities corresponding to these parameters are marked in red in Figure 2-33. The plot of the variation of the mass torque density, torque per kg magnet mass and torque versus the volumetric torque density when inner radius r_{i1} is varied are shown in Figure 2-34(a), (b) and (c) respectively. The final parameters, marked with red like the prior designs were $(r_{i1}, l_2, l_3) = (55, 10, 6)$.
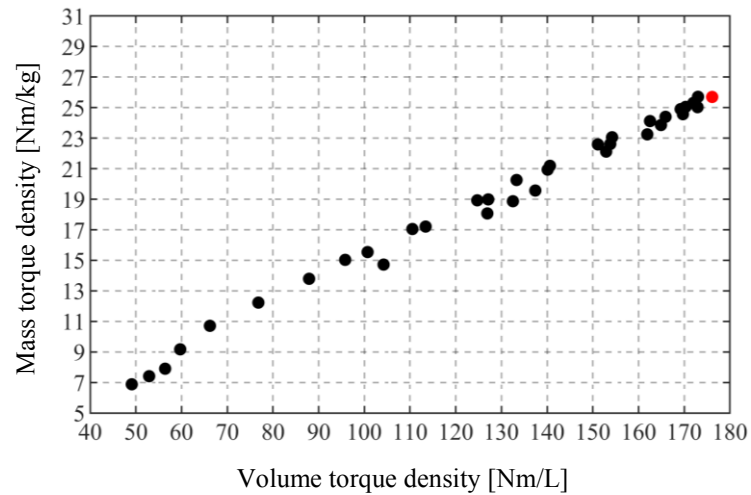
(a)
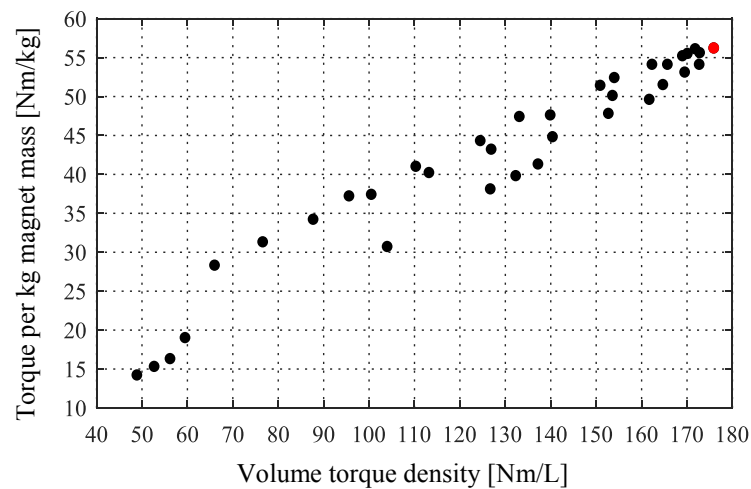
(b)

Figure 2-33: Volume torque density versus (a) mass torque density and (b) torque per kg magnet mass when l_{o2} and r_{o1} are varied
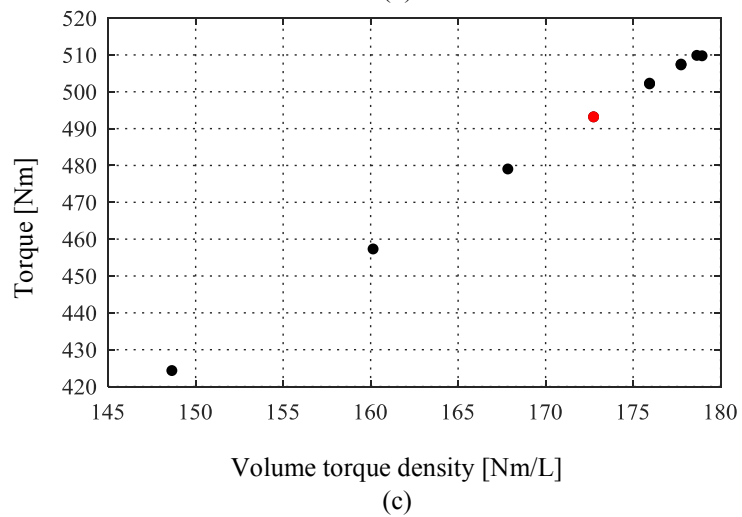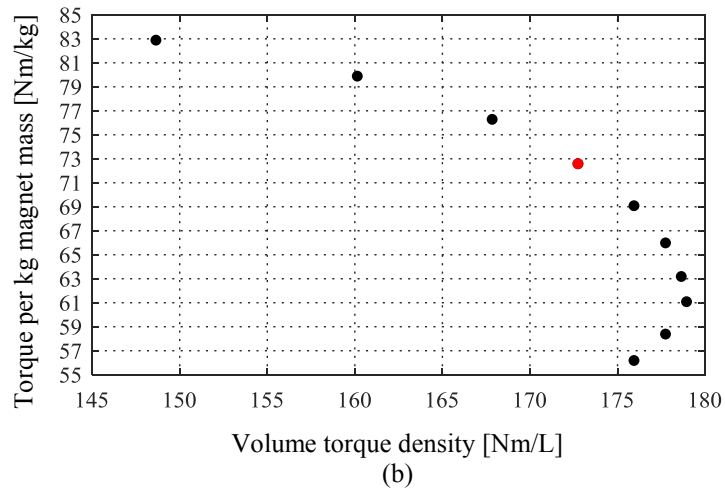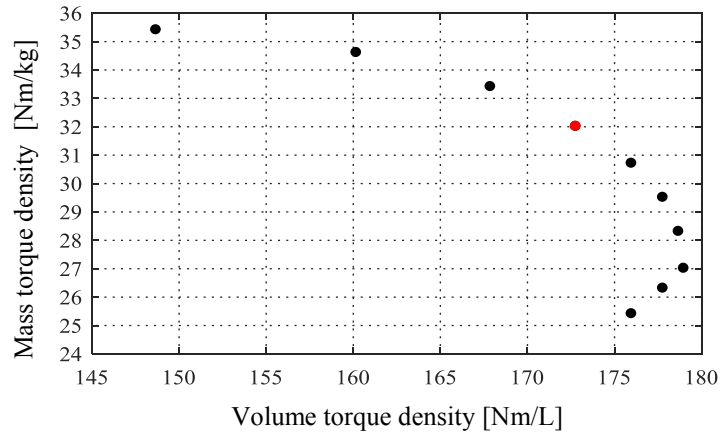
Figure 2-34: Volume torque density versus the (a) mass torque density,(b) torque per kg magnet mass and (c) torque when r_{i1} is varied

The final geometric parameters are mentioned in Table 2.11. The calculated torque as a function of low speed rotor angle is shown in Figure 2-35.The torque and the torque density values are summarized in Table 2.11.

TABLE 2.11.
FINAL GEOMETRIC PARAMETERS OF 8.5:1
OUTER CAGE ROTOR MG

	Description	Value	Unit
Inner rotor	Inner radius, r_{i1}	55	mm
	Outer radius, r_{o1}	93	mm
Intermediate	Inner radius, r_{i2}	93.5	mm
	Outer radius, r_{o2}	103.5	mm
Cage rotor	Inner radius, r_{i3}	104	mm
	Outer radius, r_{o3}	110	mm
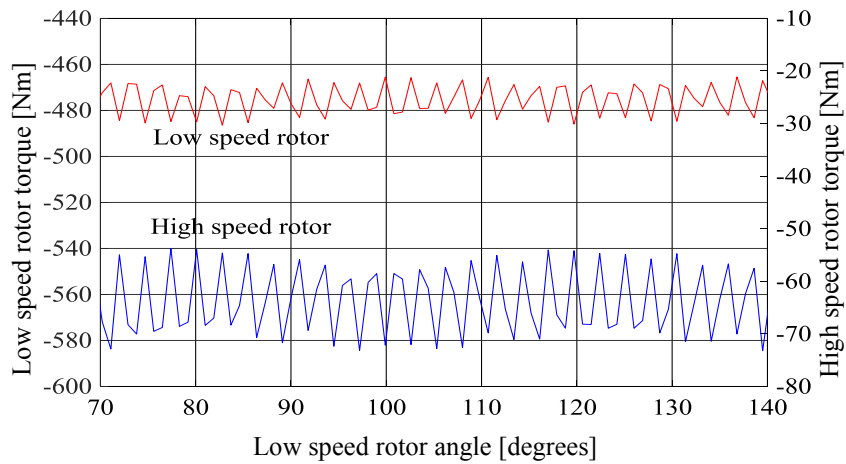
Figure 2-35. Torque for 7.5:1 gear ratio outer cage rotor flux focusing MG

TABLE 2.12.
TORQUE AND TORQUE DENSITY VALUES OF 7.5:1
OUTER CAGE ROTOR MG

Description		Value	Unit
Average torque	Inner rotor	67	Nm
	Cage rotor	544	Nm
	Intermediate rotor	472	Nm
Volume torque density		165	Nm/L
Mass torque density		32	Nm/kg
Torque per kg magnet mass		69	Nm/kg

It can be noted that by shifting the cage rotor modulating segments to the outside the torque decreased. This is because the relative distance between the modulating segments with the inner rotor and the intermediate rotor increases and hence the fields of both these rotors weaken before being modulated by the cage rotor.

2.2.4 An 8.5:1 Magnetic Gear with Consequent Pole Outer Rotor Structure

A consequent pole rotor has permanent magnets, magnetized in the radial directions, embedded in the rotor steel. The design of an MG with consequent pole outer rotor is shown in Figure 2-36. This design has the same inner rotor and cage rotor structure as an 8.5:1 idealized design. The outer rotor has been replaced by consequent poles which are oriented radially inwards. The flux path originating from a consequent pole finds its returning path through the steel segments on either side of the magnets. This gives the number of pole pairs as $(p_1, n_2, p_3) = (4, 34, 30)$. The angular span of the cage rotor is chosen to be equal to that of the consequent poles on the outer rotor. The inner rotor and the cage rotor are the high speed and low speed rotors respectively. A parametric sweep analysis using similar technique as before has been conducted. The geometric parameter definitions for the sweep analysis is shown in Figure 2-37.
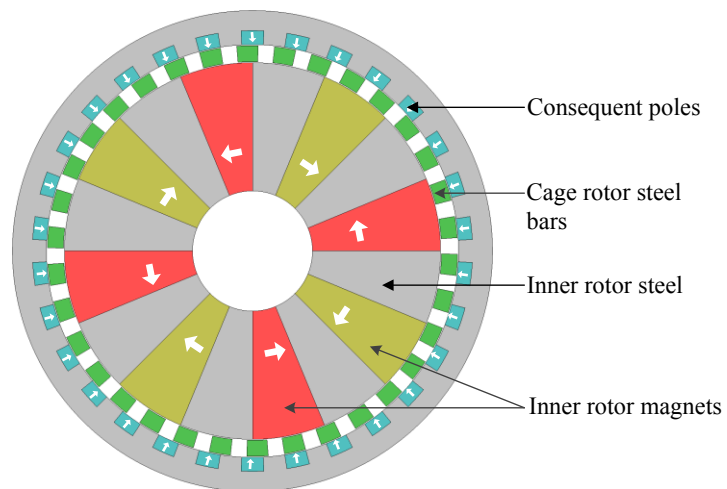
Figure 2-36: An 8.5:1 MG with consequent pole outer rotor structure
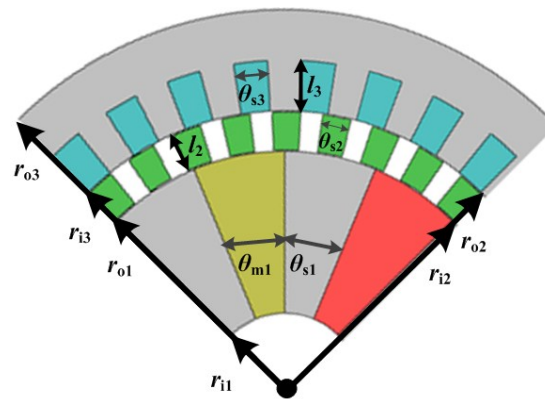
Figure 2-37: Geometric parameter definition for consequent pole MG design

By sweeping r_{o1} and l_2, the variation of the mass torque density and the torque per kg magnet mass with respect to the volume torque density are shown in Figure 2-38(a) and (b). Figure 2-39 (a),(b) and (c) shows the variation of the mass torque density, torque per kg magnet mass and torque with respect to the volumetric torque density when r_{i1} is sweeped.The parameters which produced the maximum volume torque densities have been finalized and are marked in red in Figure 2-39. The final geometric parameters are listed in Table 2.13.
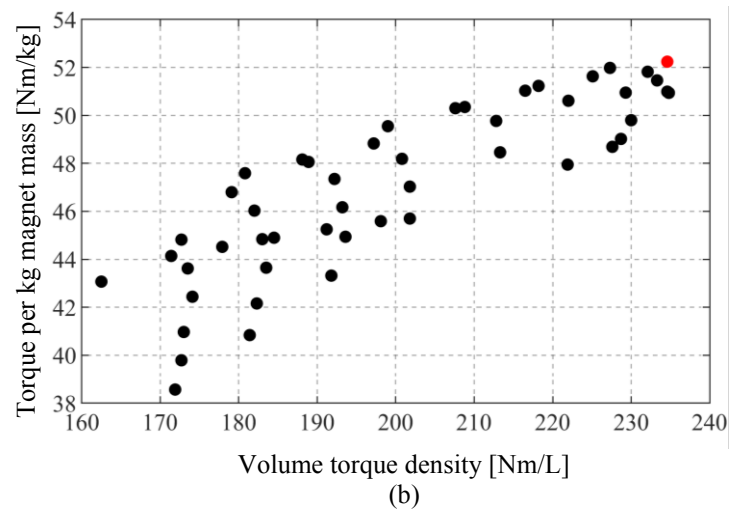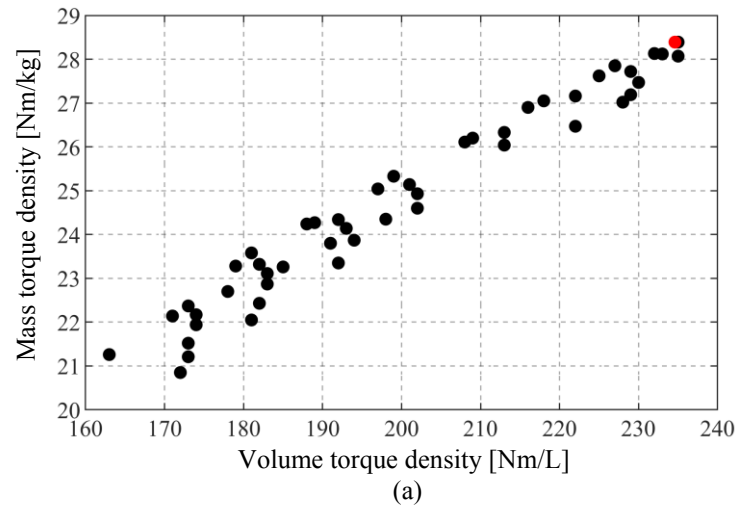
Figure 2-38: Volumetric torque density versus (a)mass torque density and (b) torque per kg magnet mass when r_{o1} and l_2 are varied
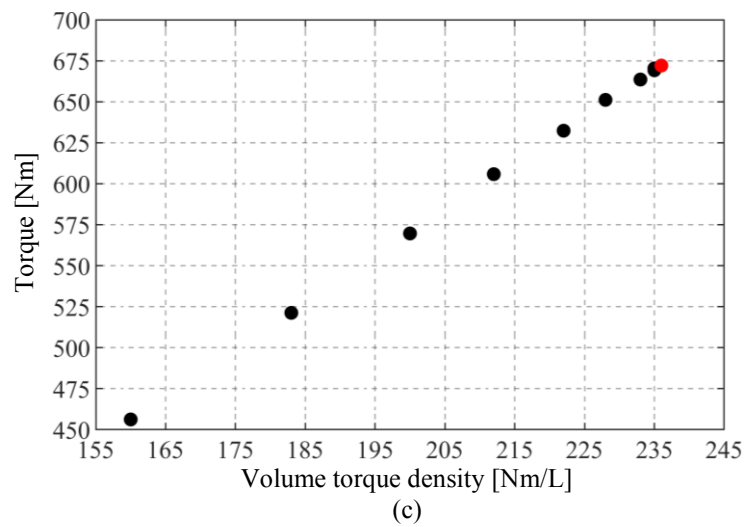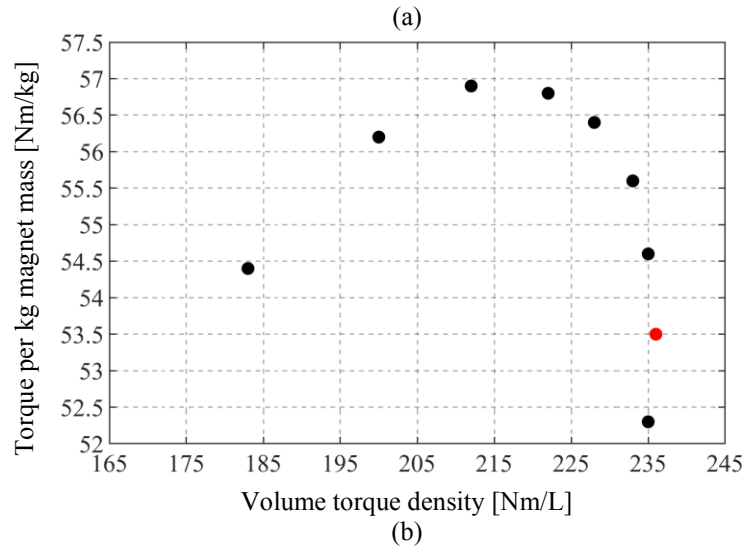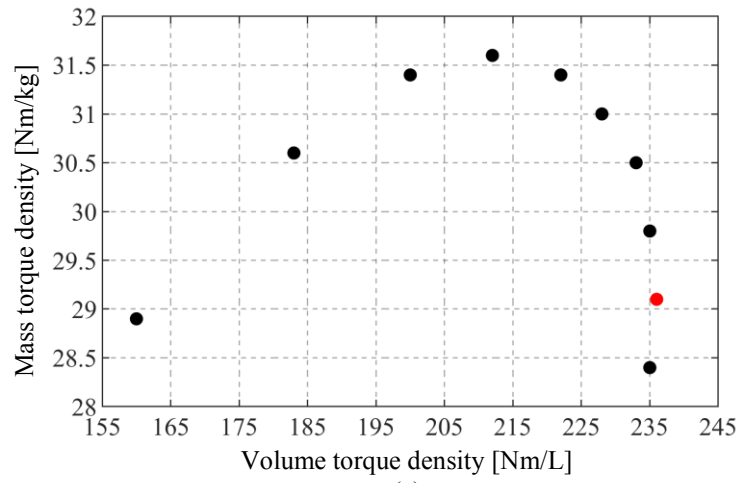
Figure 2-39: Volumetric torque density versus (a)mass torque density and (b) torque per kg magnet mass and (c) torque when r_{i1} is varied

TABLE 2.13
GEOMETRIC PARAMETERS FOR CONSEQUENT POLE
MG Simulation

	Description	Value	Unit
Inner rotor (high speed)	Inner radius, r_{i1}	30	mm
	Outer radius, r_{o1}	94	mm
	Pole span, θ_{s1}	$\pi/(2p_1)$	radian
Cage rotor (low speed)	Cage bar thickness, l_2	8	mm
	Pole span, θ_{s2}	θ_{s3}	radian
Outer rotor (stationary)	Inner radius, r_{i3}	103	mm
	Outer radius, r_{o3}	120	mm
	Consequent pole thickness, l_3	7	mm
	Pole span, θ_{s3}	π/p_3	radian

Using 2D FEA, the steady state peak torque obtained as a function of the low speed rotor angle is shown in Figure 2-40. The calculated torque and the torque density values obtained are summarized in Table 2.14. It can be noted that use of the consequent pole structure significantly decreased the torque when compared to the flux focusing design.
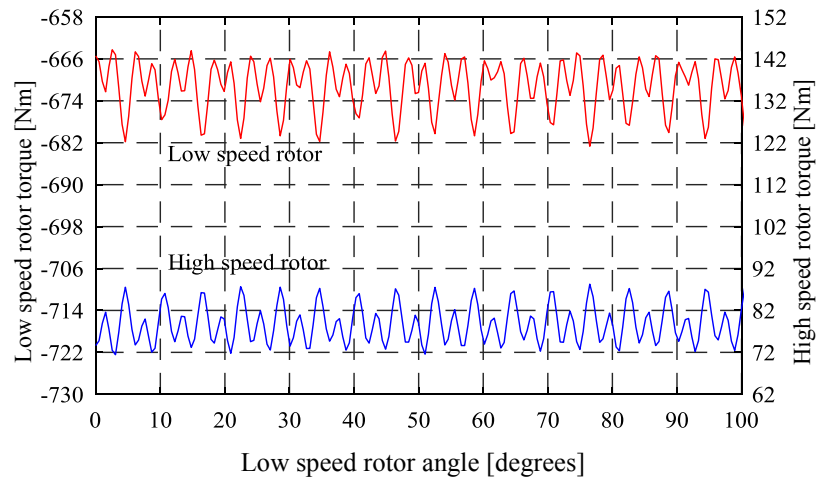
Figure 2-40: Peak steady state torque in 8.5:1 gear ratio MG with consequent pole outer rotor

TABLE 2.14.

TORQUE AND TORQUE DENSITY VALUES

	Description	Value	Unit
Average torque	Inner rotor	78	Nm
	Cage rotor	671	Nm
	Outer rotor	584	Nm
Volume torque density		198	Nm/L
Mass torque density		30	Nm/kg
Torque per kg magnet mass		79	Nm/kg

2.3 Conclusion

In this chapter different MG typologies have been studied and the FEA calculated torque and torque densities are summarized in Figure 2-41 and Table 2.15. It was shown that when the steel lips and the rectangular magnets were removed from the baseline design, the torque and the torque densities were increased by 12% for the idealized design obtained. This was due to the reduction of the air gap between the rotors when the steel lips were removed. The idealized design and the outer cage rotor MG designs were studied for both 4.25:1 and 8.5:1 gear ratios. By doubling the gear ratio the torque reduced by only 11% in the case of idealized design. Interestingly on the contrary, for the outer cage rotor design, the torque increased by 20% when the gear ratio was doubled. The torque for both the outer cage rotor design and the consequent pole designs were much lower compared to the idealized design. Thus, based on this study the idealized flux focusing design with an intermediate cage rotor between the inner and the outer rotor is considered to be the suitable design for further analysis and study.
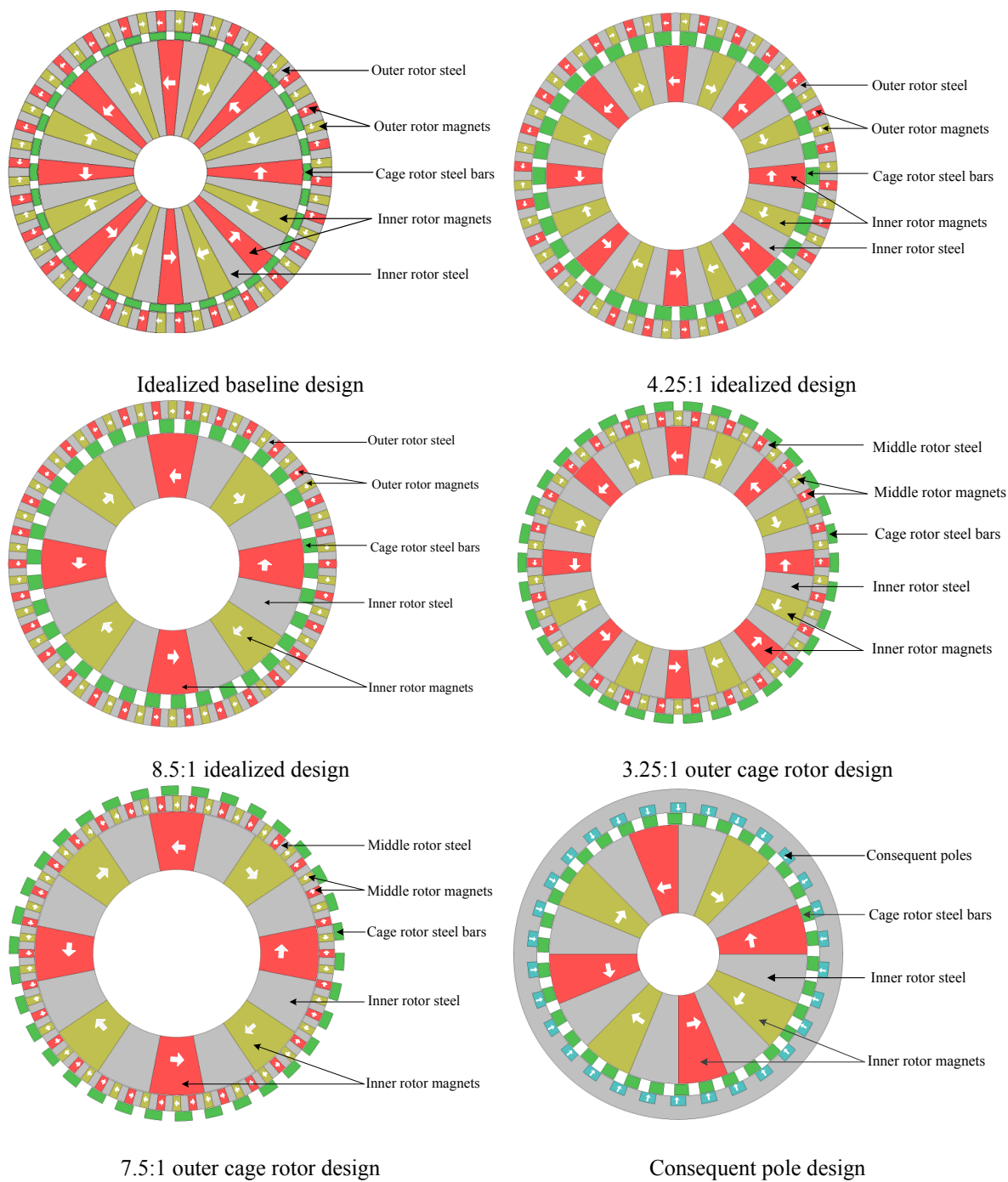
Figure 2-41: Summary of different flux focusing MG designs

TABLE 2.15.
SUMMARY OF THE PEAK TORQUE DENSITY DESIGN FOR EACH MAGNETIC GEAR
TYPOLOGIES

Description	Baseline		Idealized design		Outer cage rotor		Consequent pole	Unit
	With steel lips	No steel lips						-
Gear ratio	4.25:1	4.25:1	4.25:1	8.5:1	3.25:1	7.5:1	8.5:1	-
Volume torque density	262	357	403	336	121	165	236	Nm/L
Mass torque density	41	51	73	62	25	32	29	Nm/kg
Torque per kg magnet mass	88	110	165	142	54	69	53	Nm/kg
Torque	805	1019	1142	1017	344	472	671	Nm

3 FLUX CONCENTRATION HALBACH MAGNETIC GEARBOX ANALYSIS

3.1 Introduction

A new type of flux concentration Halbach (FCH) rotor typology was recently proposed by Hibbs *et al.* [97] in which an additional flux concentration ferromagnetic steel pole was added into the Halbach rotor. An example of FCH rotors used in a MG structure is shown in Figure 3-1. By adding additional ferromagnetic pole pieces in front of the radially directed magnets the flux concentration Halbach type rotors can be constructed without the need for a mechanical retaining sleeve; this thereby enables a smaller air-gap to be maintained between rotors. This type of FCH structure was recently studied by Fu *et al.* [98] for use in a MG. Fu showed that it held particular promise. However, the steel poles in Fu's simulated design were selected to be 0.4 mm thick which appears to be impractically thin to construct. Apart from the additional patent by Toyota *et al.* [99] it would appear that few authors have studied this type of novel rotor typology. The practical benefits of using this new FCH structure in a MG are investigated in this chapter. Analysis and experimental results for a FCH-MG structure are also presented.
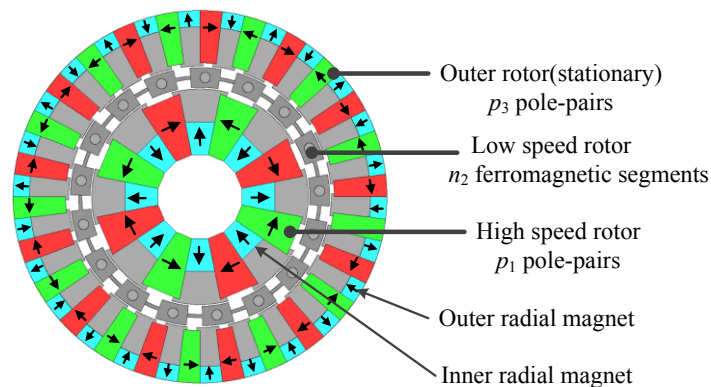
Figure 3-1: Cross-sectional view of a 4.25:1 flux concentration Halbach rotor magnetic gearbox.

3.2   Flux Concentration Halbach Rotor Design

The MG parameters used in the FCH-MG design are summarized in Table 3.1. The design is based on the flux-focusing MG design presented in [100] and shown in Figure 3-2 and the performance of the FCH-MG will be compared with this base design.

A parameter sweep analysis when changing only the radial length of the inner and outer radial magnets was conducted as shown in Figure 3-3 for the FCH-MG design. Based on this sweep analysis the outer and inner radial magnets were selected to be 10mm and 6mm in radial length respectively. Using finite element analysis (FEA) the peak torque for this FCH-MG was calculated to be T_2 = 148.7 Nm (201Nm/L) while the calculated peak torque for the flux focusing MG shown in Figure 3-2 was T_2 = 103.1Nm (139.5 Nm/L) [100]. This indicates that the FCH-MG typology should significantly increase the torque density of the MG, however this will be at the cost of increasing mechanical construction and assembly complexity.
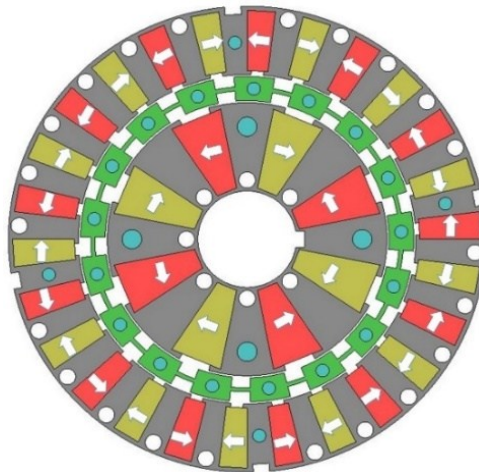
Figure 3-2: Flux focusing magnetic gearbox with 4.25:1 gear ratio. The inner rotor as p_1=4 pole-pairs, the outer rotor has p_3=13 pole pairs. [100]

TABLE 3.1.
FLUX CONCENTRATION HALBACH MAGNETIC GEARBOX PARAMETERS

	Description	Value	Unit
Inner rotor	Inner radius, r_{i1}	12.5	mm
	Outer radius, r_{o1}	33.0	mm
	Pole pairs, p_1	4	-
	Angular span, θ_1	$\pi/(2p_1)$	radians
	Radial length of radial magnet	8.0	mm
	Radial length of azimuth magnet	18.6	mm
Cage rotor	Inner radius, r_{i2}	33.5	mm
	Outer radius, r_{o2}	39.5	mm
	Pole pairs, n_2	17	-
	Angular span, θ_2	0.2443	radians
	Connecting bridge, inner radius	36	mm
	Connecting bridge, outer radius	37	mm
	Rods, radius	1.5875	mm
Outer rotor	Inner radius, r_{i3}	40.0	mm
	Outer radius, r_{o3}	57.0	mm
	Pole pairs, p_3	13	-
	Angular span, θ_3	$\pi/(2p_3)$	radians
	Radial length of radial magnet	4.0	mm
	Radial length of azimuth magnet	14.0	mm
Axial stack length, d		75	mm

In order to enable the FCH-MG to be assembled more easily back-iron was added, as

shown in Figure 3-4. The back-iron resulted in the radial magnets on the inner and outer

rotor being reduced in length to 8mm and 4mm respectively. The back-iron also allowed

the magnets to be made with rectangular and trapezoidal dimensions. These changes

reduced the peak calculated torque to $T_2 = 142.2$ Nm (192.4Nm/L). The peak torque as a

function of angular position is shown in Figure 3-5, the torque ripple is low. The radial

and azimuthal magnetic flux density within the FCH-MG is shown in Figure 3-6.The

saturation within the ferromagnetic poles can be seen in Figure 3-6(a), the additional

radial magnets greatly reduces the azimuthal flux leakage when compared to using flux

barrier holes [100].
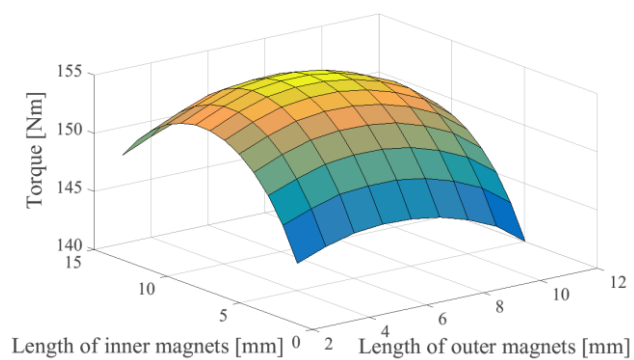
Figure 3-3: Inner and outer rotor radial magnet length
parameter sweep analysis
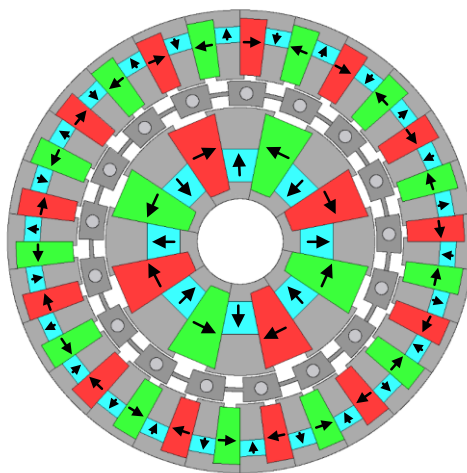
Figure 3-4: Cross-sectional view of the
4.25:1 flux-concentration Halbach MG with
back-iron added in place.
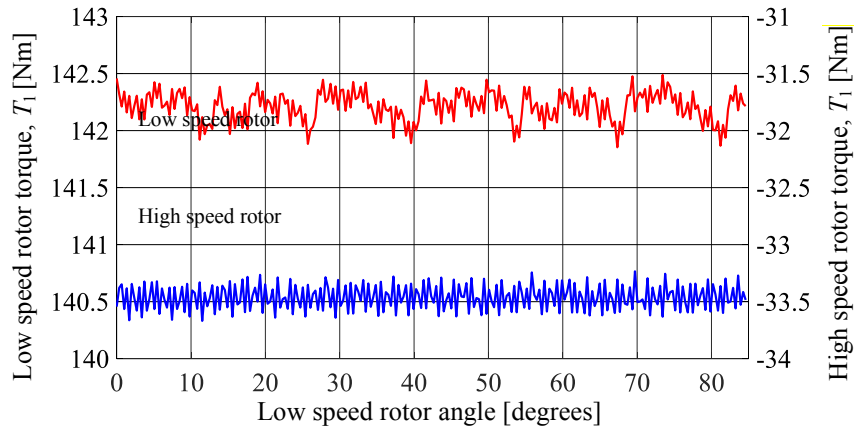
Figure 3-5: Peak torque as a function of low-speed rotor angle for the high and low speed rotors
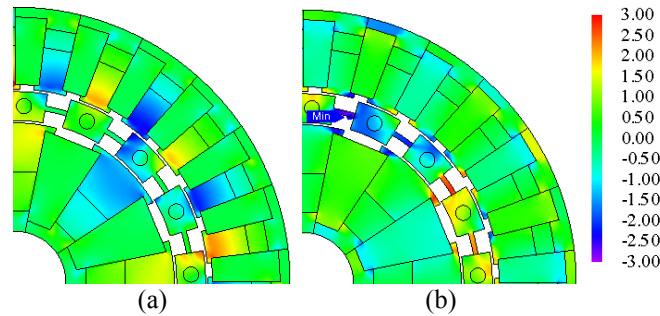
Figure 3-6: (a) Radial flux density B_r and (b) azimuthal flux density B_θ for the flux concentration Halbach design with reduced B_r values

3.3   Experimental Prototype

The FCH-MG mechanical assembly is illustrated in Figure 3-7 the central cage rotor is made of laminations while the inner and outer rotor poles are made using solid ferromagnetic steel. Solid steel was used for some parts as the primary purpose of the analysis was to investigate the construction feasibility and peak torque density (but not high speed efficiency) of this novel FCH-MG structure. The inner rotor steel poles are shown in Figure 3-8(a) and the laminated cage rotor is shown in Figure 3-8(b). The outer rotor assembly is shown in Figure 3-8(c) and the fully assembled inner rotor and

complete assembly is shown in Figure 3-9. The inner rotor was not significantly more difficult than a typical rotor to construct. However, the outer rotor was significantly more difficult to assemble because there were a large number of assembly pieces.
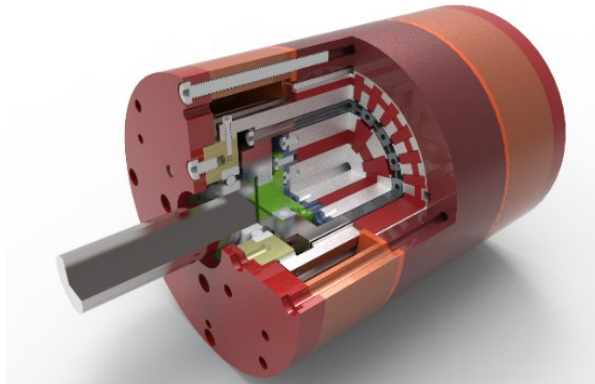
Figure 3-7: Mechanical assembly of the FCH-MG

(a) (b) (c)
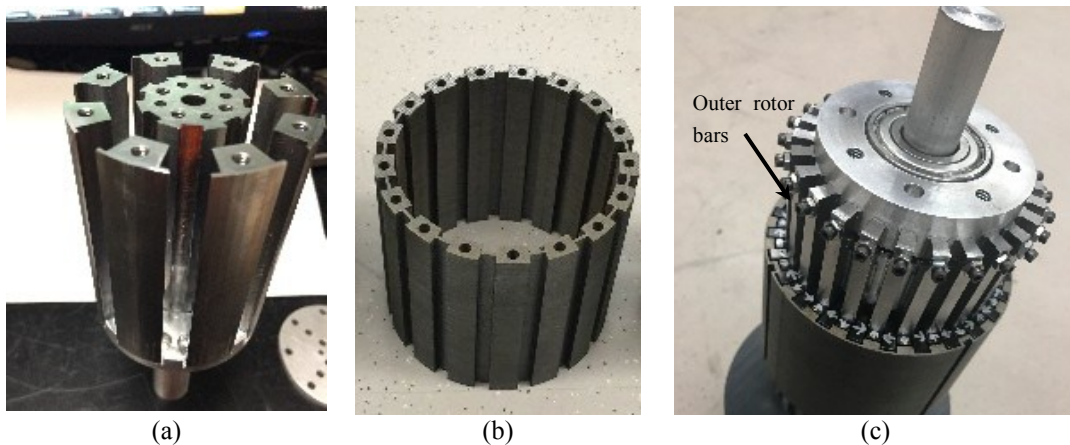
Figure 3-8.(a) Inner rotor 1018 grade ferromagnetic poles (b) low speed M19 ferromagnetic cage rotor and (c) outer rotor with 1018 ferromagnetic steel

(a) (b)

Figure 3-9. (a) High-speed inner rotor assembly (b) fullly assembled MG

The inner rotor field comparison, when surrounded by air, is shown in Figure 3-10 and the harmonic comparison is shown in Figure 3-11. It shows that the measured peak fundamental radial magnetic flux density value is $B_r = 0.4$ T while the fundamental of the FEA calculated value is $B_r = 0.44$ T. In order to match the torque values the magnet's residual flux density value was reduced to $B_{mr} = 1$ T. Using this reduced B_{mr} value the MG torque was recalculated as shown in Figure 3-12. The reduced residual flux density caused the calculated peak torque to reduce to $T_2 = 116.5$ Nm (152 Nm/L). The FCH-MG was experimentally tested by making load step changes using the test setup shown in Figure 3-13, the measured torque step changes as a function of time are shown in Figure 3-14. The peak torque was measured to be only $T_2 = 82.8$ Nm. This measured torque value is 27% lower than the expected torque value and represents a measured torque density of only 112 Nm/L.
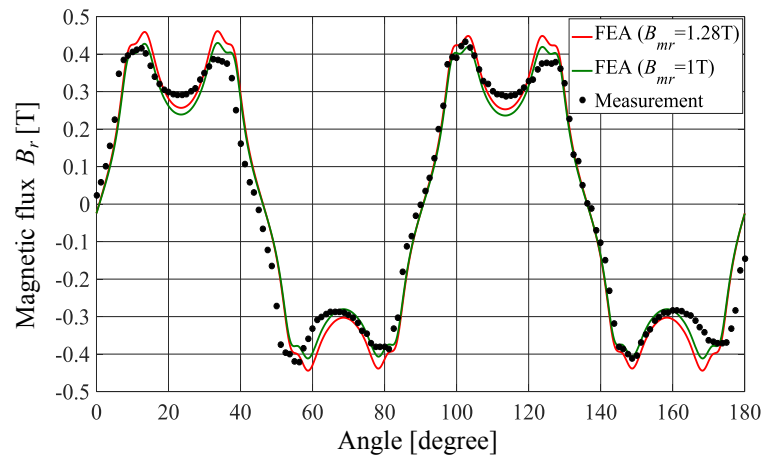
Figure 3-10: Measured inner rotor field at 1.3mm above the rotor surface. The inner rotor is surrounded by air. Also shown is the calculated magnetic flux density field values when $B_{mr} = 1.28$T and $B_{mr} = 1$T.
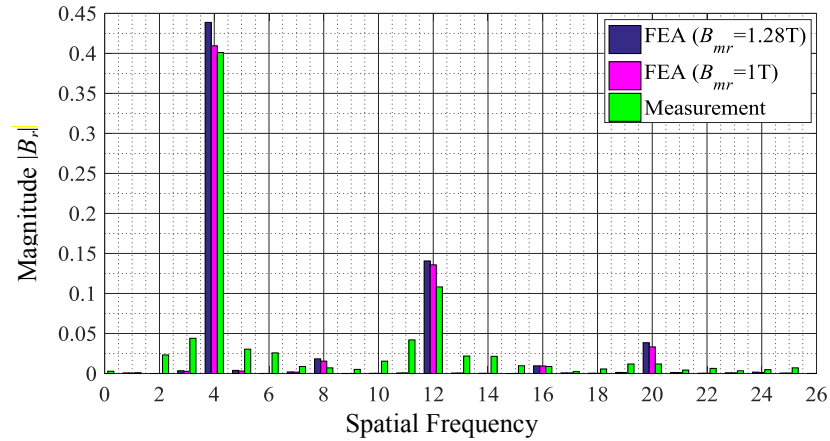
Figure 3-11: Spatial harmonic analysis of the inner rotor radial magnetic
flux density when surrounded by air.

An additional reason for the significantly lower torque than expected is believed to be
due to the need to pre-stress the outer rotor bars, shown in Figure 3-8(c), so as to prevent
them from making contact with the low-speed rotor. This caused intentional deflection in
the bars that resulted in a larger than expected air-gap. A summary of the measured and
calculated torque and torque density values is shown in Table 3.2 for the case when
different discrepancies are accounted for.

TABLE 3.2.
SUMMARY OF CALCULATED AND MEASURED TORQUE
AND TORQUE DENSITY

Analysis type	Peak torque [Nm]	Peak torque density [Nm/L]
2-D - original	142	185
2-D - reduced magnet B_r	118	154
3-D - reduced magnet B_r	106	138
3-D - reduced B_r, (1mm outer rotor air gap)	92	120
Measured value	82	107
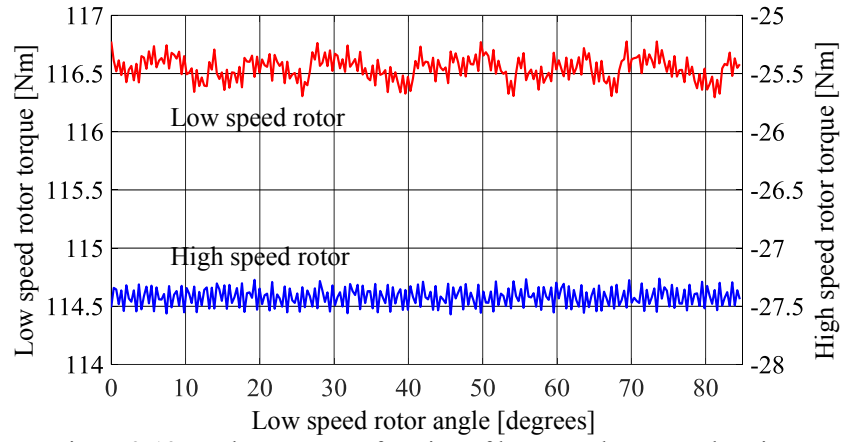
Figure 3-12: Peak torque as a function of low-speed rotor angle using reduced magnet residual flux density B_{mr}.
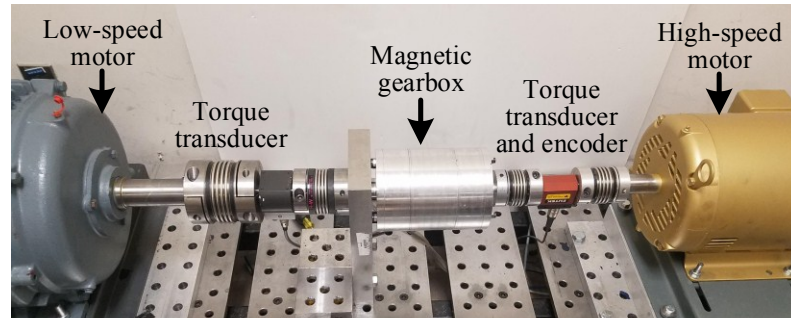
Figure 3-13: Experimental test-stand for testing the FCH-MG
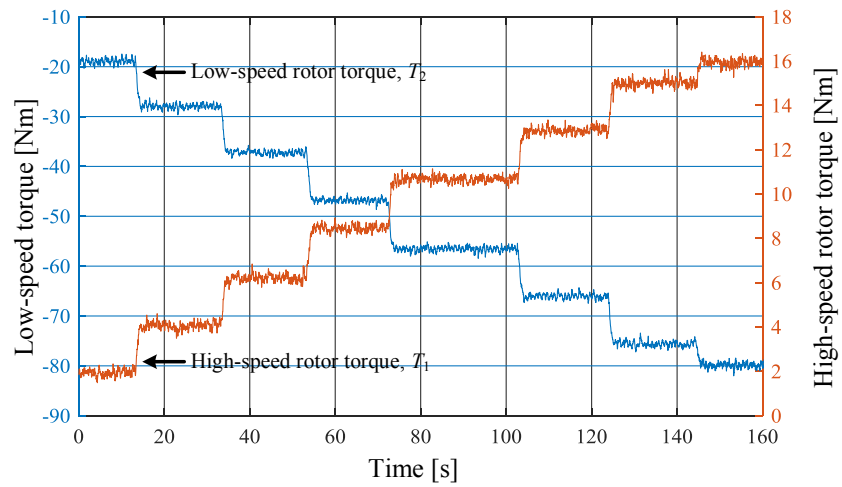
Figure 3-14:Experimentally measured torque and at different load levels

3.4   Ideal Sizing Analysis

It was shown earlier that the inclusion of the ferromagnetic pole in front of the radial Halbach rotor magnet increased the torque density. This increase is caused by the steel pole concentrating the magnetic field thereby increasing the flux density around the air-gap. In order to properly understand the effect of using the ferromagnetic rotor pole an ideal MG typology as illustrated in Figure 3-15 was studied. This design does not contain any magnet retaining lips or additional back-iron and therefore enables the influence of the ferromagnetic rotor pole addition to be more clearly highlighted.
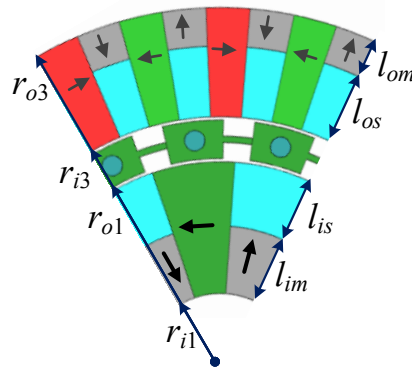
Figure 3-15: Ideal model of FCH-MG
with dimensional definitions

Using the inner rotor magnet and steel pole lengths, as defined in Figure 3-15, a scaling ratio can be defined as

$$\Gamma_{\mathrm{i}} = \frac{l_{im}}{l_{im} + l_{is}}$$

(3.1)

Similarly, an outer rotor magnet-steel scaling ratio can be defined as

$$\Gamma_o = \frac{l_{om}}{l_{os} + l_{om}} \tag{3.2}$$

When $\Gamma_i = \Gamma_o = 1$ the MG forms a 4 segment Halbach rotor MG when $\Gamma_i = \Gamma_o = 0$ the MG rotors become spoke-type or flux focusing in typology. Using (3.1) and (3.2), the steel pole lengths were varied for the ideal MG design and the peak torque, torque density and mass torque density were computed. The results are shown in Figure 3-16.

The active mass torque density was computed from

$$T_m = \frac{T_2}{m_s + m_m} \tag{3.3}$$

where, m_s is the ferromagnetic steel mass

$$m_s = \frac{\pi}{2} \rho \qquad \qquad \rho \tag{3.4}$$

and m_m is the magnet material mass

$$m_m = \frac{\pi}{2} \rho \quad \underset{\_}{} \quad \left(r_{i1} + l_{im}\right)^2 - 2r_{i1}^2 + r_{o3}^2 - r_{i3}^2 + r_{o3}^2 - \left(r_{o3} - l_{om}\right)^2 \right] \tag{3.5}$$

where $\rho_s = 7850$ kg/m³ and $\rho_m = 7600$ kg/m³ are the mass density values for the steel and magnet material and θ is the fraction of angular span occupied by the cage rotor segments. The magnet mass torque density is then simply

$$T_{mm} = \frac{T_2}{m_m} \tag{3.6}$$
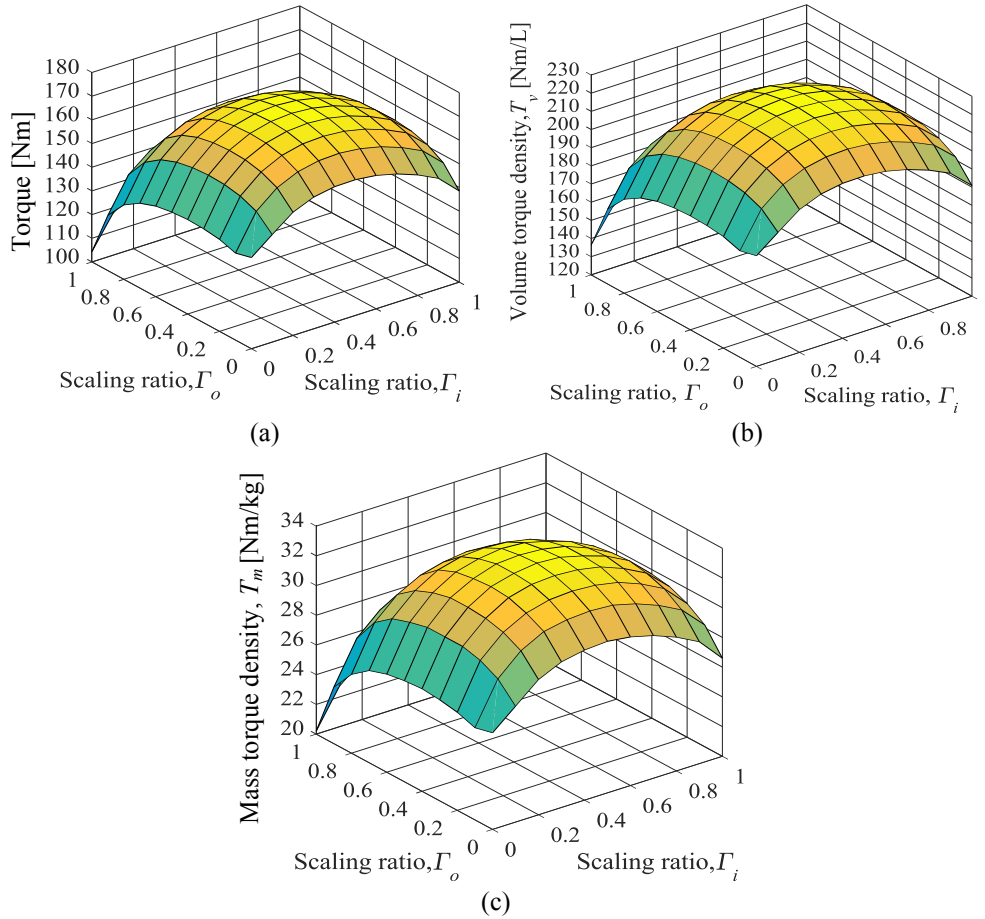
Figure 3-16: The influence of inner rotor scaling ratio, Γ_i and outer rotor scaling ratio, Γ_o, on (a) torque, (b) active region volumetric torque density and (c) active region mass torque density

By studying Figure 3-16, it was determined that the peak torque and torque density occurred at $(\Gamma_i,\ \Gamma_o) = (0.5,\ 0.43)$. The torque density however does not change significantly when the outer radial magnet ratio is significantly greater than $\Gamma_o = 0.2$. This is seen by looking at Figure 3-17 in which Γ_i was held fixed at $\Gamma_i = 0.5$. Figure 3-17(a)

shows that there is minimal change in volumetric torque density between $\Gamma_o = 0.2$ and $\Gamma_o = 0.7$. The mass torque density, shown in Figure 3-17(b), exhibits a similar relationship. In contrast the magnet mass torque density is highest when $\Gamma_o = 0$. This is not true for the inner rotor however Figure 3-18 shows that the peak magnet mass torque density occurs at $(\Gamma_i, \Gamma_o) = (0.2, 0)$. Therefore, even the magnet mass torque density can benefit from having some percentage of ferromagnetic inserts.
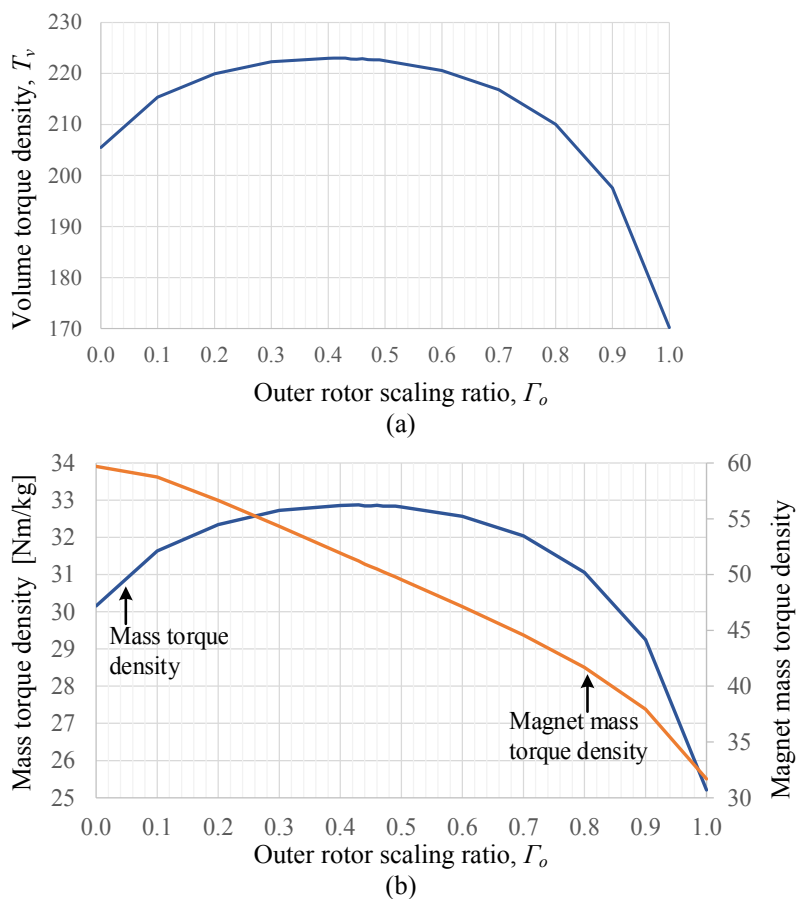
Figure 3-17:Variation of (a) volume torque density, (b) mass torque density and torque-per-kg magnet mass as a function of outer scaling ratio for an inner scaling ratio of $\Gamma_i = 0.5$.
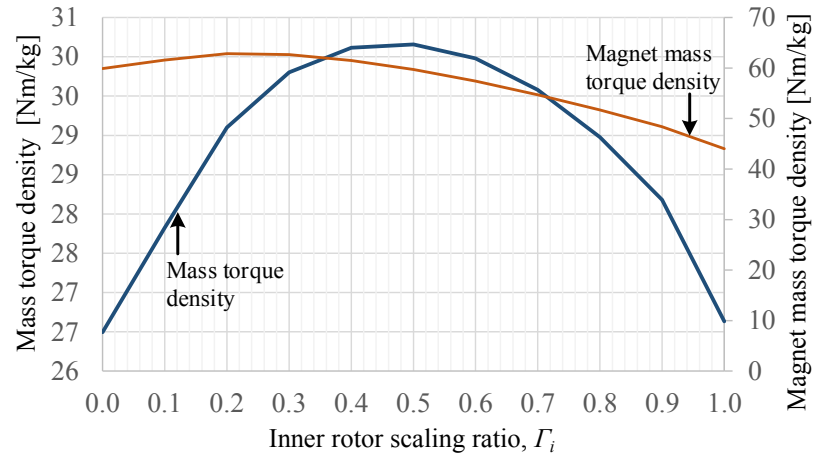
Figure 3-18: Variation of mass torque density and magnet mass torque density as a function of inner scaling ratio when the outer scaling ratio is $\Gamma_o = 0$.

In order to study the impact of the inclusion of the ferromagnetic segment the analysis presented here was for the case when the inner and outer rotor radial lengths were constant such that $(r_{o1}-r_{i1}) = 20.5$ mm and $(r_{o3} - r_{i3}) = 17$mm. However, the general conclusion that the inclusion of the ferromagnetic poles increases torque density still holds when a smaller rotor radial length is used. For example, Figure 3-19 shows how the torque density changes when a different r_{i1} is used. It can be seen that in this case the peak volumetric torque density is not at either $\Gamma_i = 1$ or $\Gamma_i = 0$. A summary of the torque analysis results is provided in Table III.
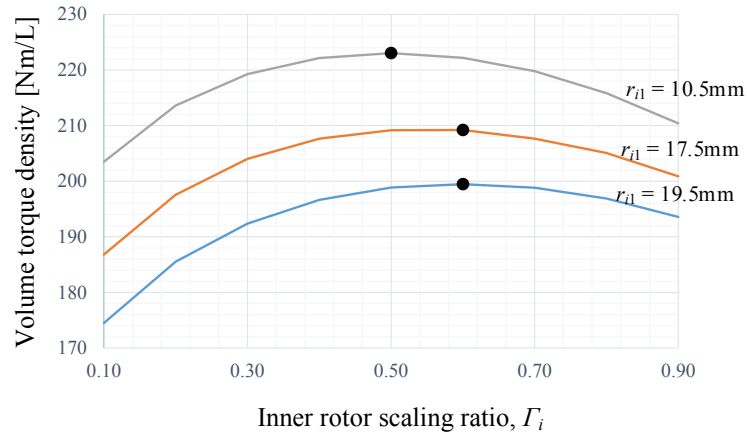
Figure 3-19: The variation of torque density as a function of inner rotor scaling ratio for different inner radius values when $\Gamma_o = 0.43$. The peak torque density located is marked with a black marker. The outer rotor radii of the inner rotor was kept constant at $r_{o1} = 33$mm.

TABLE 3.3
CALCULATED TORQUE DENSITY RESULTS WHEN VARYING THE INNER
AND OUTER ROTOR SCALING RATIOS

Rotor type	(Γ_i, Γ_o)	Torque density		
		Volume, T_v [Nm/L]	Mass, T_m [Nm/kg]	Magnet mass, T_{mm} [Nm/kg]
Flux focusing rotor	(0,0)	171.2	25.4	56.7
Halbach rotor	(1,1)	153.8	22.9	25.5
Flux concentration rotor	(0.5,0.43)	223.0	33	51.2
	(0.2,0)	198.6	29.1	62.9
	(0.5,0)	205	30	59.7

3.5   Conclusion

A new type of FCH-MG has been presented and experimentally tested. The measured torque density was determined to be 112Nm/L. It was shown that by incorporating the ferromagnetic flux concentration poles within the Halbach type structure the torque density could be increased. However, this did increase the number of assembly parts and resulted in a more complicated assembly process. Therefore, using a FCH rotor structure is perhaps best considered in situations where the rotor has a low number of pole-pairs.

4   INNER STATOR MAGNETICALLY GEARED MACHINE ANALYSIS

4.1   Introduction

Different designs of MGs aiming at achieving high torque densities have been studied and some prototypes were built [36, 45-47]. The process of designing MGs with even higher torque densities is still ongoing. However, MGs are simply transmission devices which have no provision for providing or obtaining electrical input or output. Instead of just being a replacement of a mechanical gear, integrating an MG with an electrical machine should be considered for the purpose of practical application. Thus a new class of a compact system known as MGM was developed. The MGM could then replace the conventional drive system, which consists of a motor, mechanical gear and a torque limiter [9]. The high speed rotor is driven by the electromotive force generated by the windings and the low speed rotor rotates in accordance with the gear ratio. MGMs can be categorized broadly into four types on the basis of integrating the electrical machine with the MG. These are the mechanically coupled machines [48-56], the pseudo machines [19, 57-63], the mechanically and magnetically coupled machines [64-77] and the partitioned stator machines [78-89]. Based on the relative positions of the electrical machine to the MG, MGMs can be further classified as internal stator MGM [90] and external stator MGM [27]. Such MGMs are illustrated in Figure 1-3. In this chapter, internal stator MGM designs with fractional slot and integral slot stator windings and utilizing flux focusing rotors have been studied.

4.2   Inner Stator Magnetically Geared Motor

The 8.5:1 gear ratio inner stator MGM with flux focusing rotors that will be studied in this section is shown in Figure 4-1. The number of pole pairs is the same as the design studied in section 2.2.2.3 i.e. $(p_1, n_2, p_3) = (4, 34, 30)$. The inner radius of the inner rotor has been modified to $r_{i1} = 40$ mm to accommodate the stator on the inside of the MG. The outer radius of the MG has been increased from $r_{o3} = 110$ mm to $r_{o3} = 145$ mm to compensate for the reduced torque density obtained as a consequence of increasing r_{i1}. The stator windings must be designed to produce a rotating magnetic field that would interact with the inner rotor.

To maximize the torque density, a parametric sweep analysis has been performed initially on the MG. The sweep analysis was performed using the same technique utilized in section 2.2.2.3 for the 8.5:1 MG design. The plot of the volume torque density versus the mass torque density and the torque per kg magnet mass obtained by varying the cage rotor thickness, l_2 is shown in Figure 4-2. By sweep analysis, the parameters chosen for further simulation are $(r_{i1}, r_{o1}, l_2) = (40, 118, 11)$ mm. The corresponding torque densities are marked in red in Figure 4-2(a) and (b).
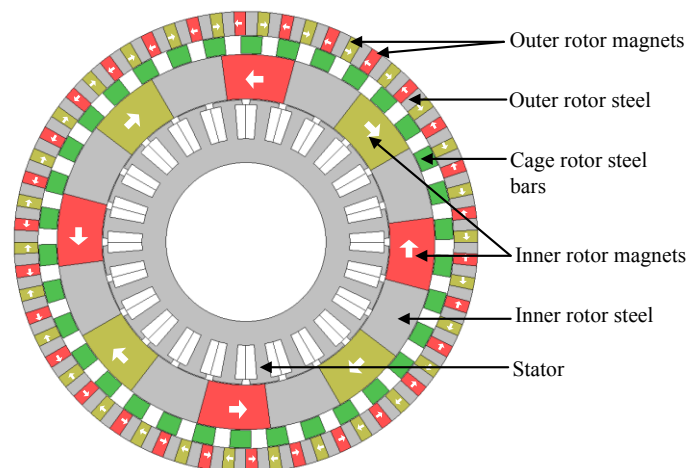
Figure 4-1: An 8.5:1 internal stator MGM
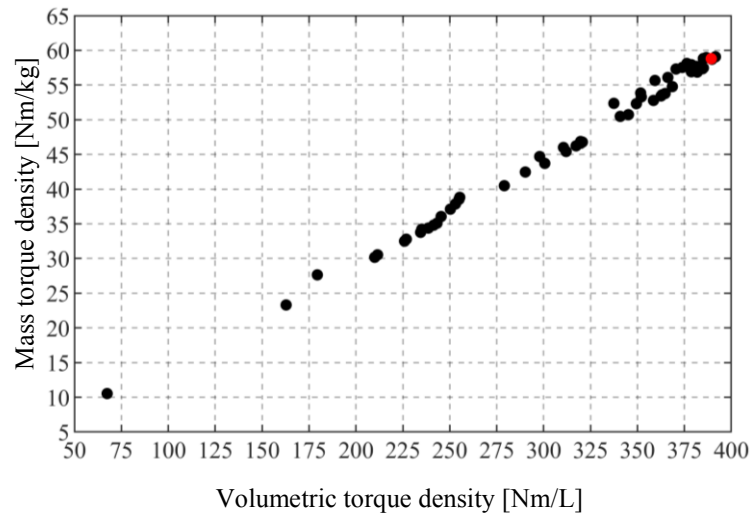
(a)
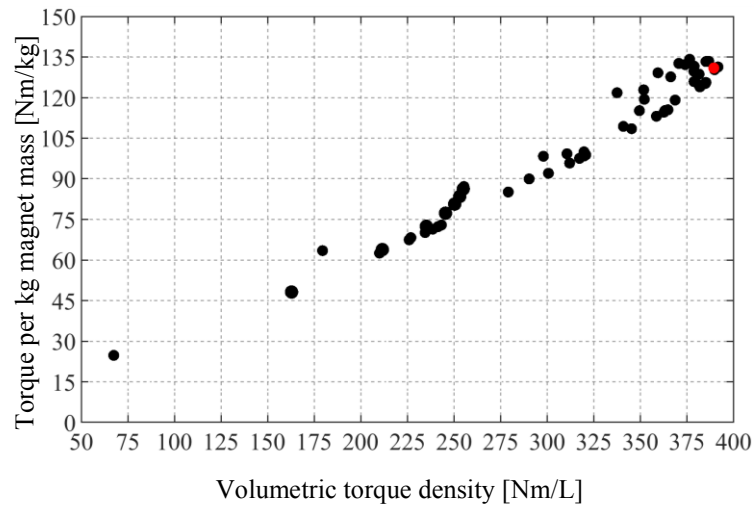
(b)

Figure 4-2: Volumetric torque density versus (a) mass torque density, (b) torque per kg magnet mass when r_{o1} and l_2 are varied

In order to accommodate the internal stator, r_{i1} should be modified such that the stator can operate at a peak volume torque density of $T_{ds} = 90$ Nm/L on the inner rotor surface. The inner rotor surface torque density is computed from

$$T_{ds} = \frac{T_1}{\pi \times d \times r_{i1}^2}$$

(4.1)

This torque density is assumed to be the peak torque density that can be achieved over a short time period. It is not the continuous torque rating. The variation of T_{ds} with r_{i1} is shown in Figure 4-3(a). The final parameters which produced a value of $T_{ds} = 90$ Nm/L are $(r_{i1}, r_{o1}, l_2) = (90, 118, 11)$ mm. The overall compromise in the volume torque density of the MG for selecting $T_{ds} = 90$ Nm/L, is evident from Figure 4-3(b). The peak volume torque density decreased from 388 Nm/L to 300 Nm/L. The selection of these final geometric parameter values did not cause significant compromise of the torque and other torque densities from their peak values as shown in Figure 4-4. However, the torque is reduced from its maximum value of 1900 Nm to 1500 Nm.
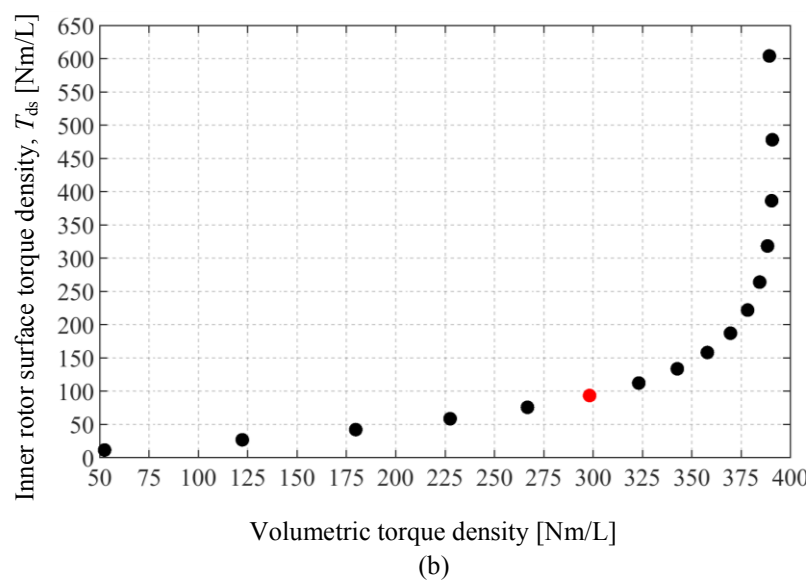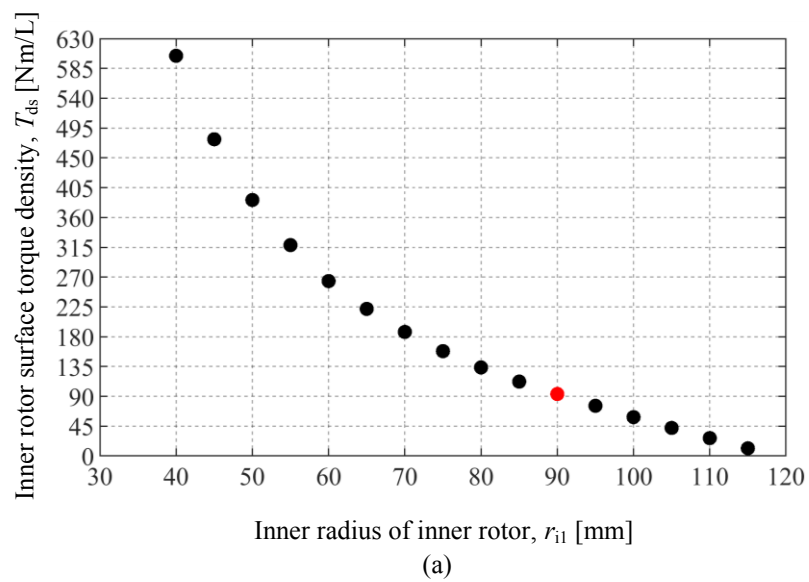
Figure 4-3: Variation of the inner rotor surface torque density versus (a) the inner radius of inner rotor and (b) volumetric torque density when r_{i1} is varied
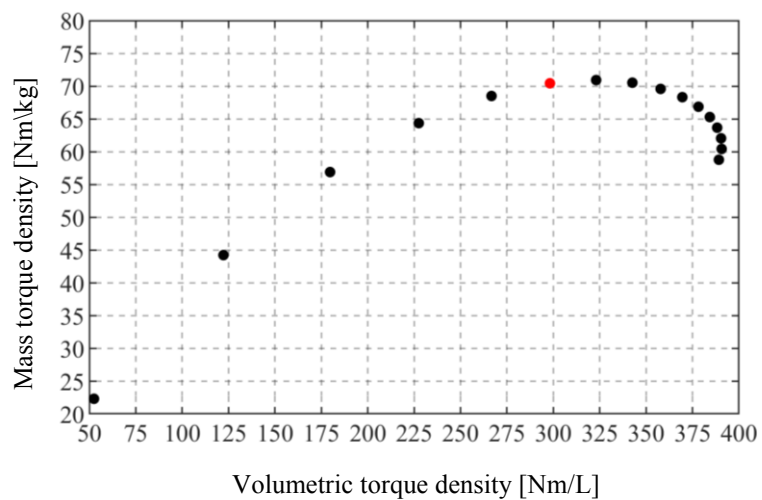
(a)
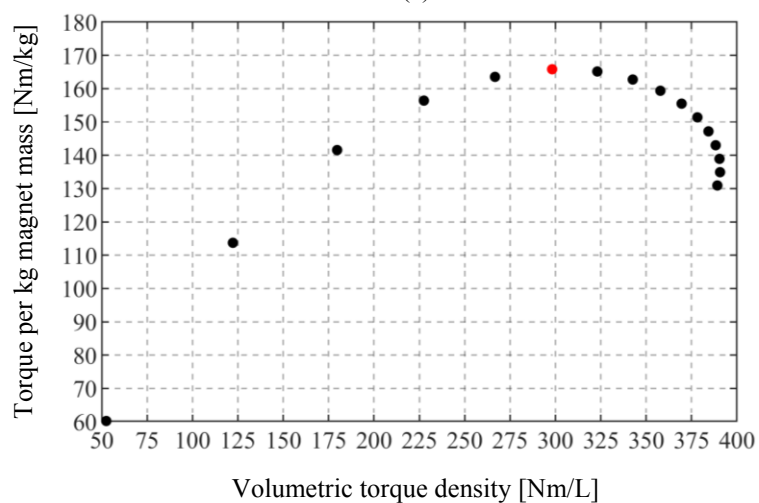
(b)
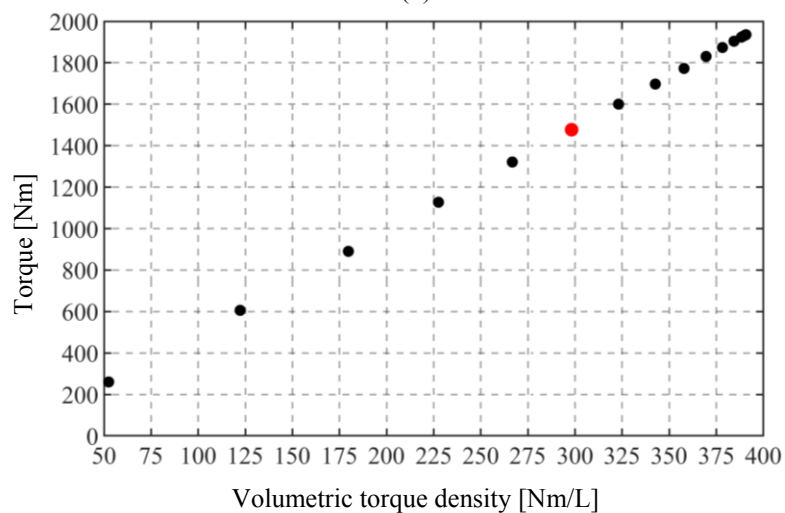
(c)

Figure 4-4: Volumetric torque density versus (a) mass torque density, (b) torque per kg magnet mass and (c) torque when r_{i1} is varied

The final design of the MG is shown in Figure 4-5. The corresponding geometric parameters are mentioned in Table 4.1. The design was simulated using 2D FEA. The variation of the pole slipping torque as a function of the low speed rotor angle is shown in Figure 4-6. The torque density values calculated using (2.65), (2.66), (2.67) and the torque are specified in Table 4.2.
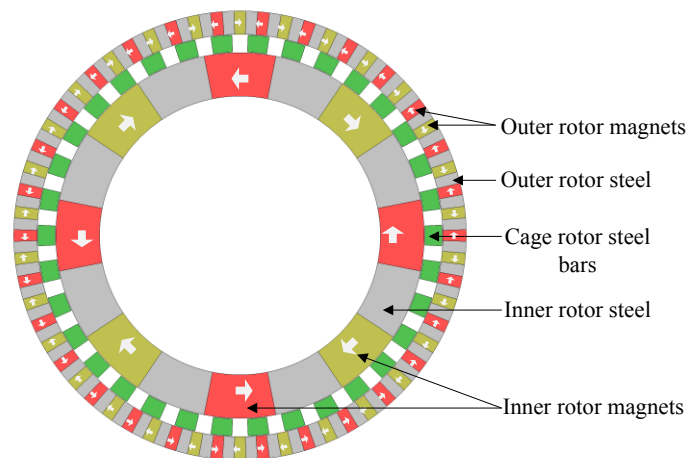
Figure 4-5: MG with a gear ratio of 8.5:1, inner radius r_{i1} = 90 mm, cage rotor thickness l_2 = 11 mm and no stator

Table 4.1.
FINAL GEOMETRIC PARAMETERS OF THE 8.5:1 MG

Description		Value	Unit
Inner rotor (high speed)	Inner radius, r_{i1}	90	mm
	Outer radius, r_{o1}	118	mm
Cage rotor (low speed)	Inner radius, r_{i2}	118.5	mm
	Outer radius, r_{o2}	129.5	mm
Outer rotor (stationary)	Inner radius, r_{i3}	130	mm
	Outer radius, r_{o3}	145	mm
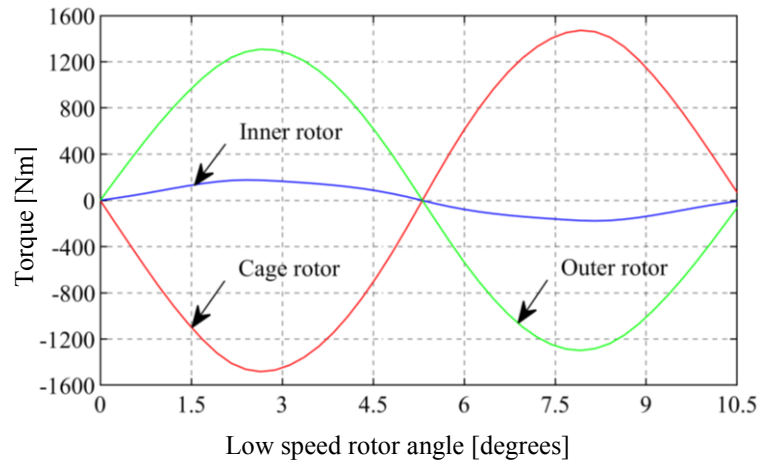
Figure 4-6: Torque as a function of low speed rotor angle for MG
without a stator

TABLE 4.2.
TORQUE AND TORQUE DENSITY VALUES OF 8.5:1 MG
WITHOUT STATOR

Description		Values	Units
Peak torque	Inner rotor	174	Nm
	Cage rotor	1482	Nm
	Outer rotor	1308	Nm
Volume torque density		292	Nm/L
Mass torque density		68	Nm/kg
Torque per kg magnet mass		162	Nm/kg

In the following sections, both the fractional slot winding and an integral slot winding for the inner stator MGM have been studied.

4.2.1   Fractional Slot Inner Stator MGM Design

The stator which uses windings where, the number of slots per pole per phase q is not an integer is called a fractional slot stator [9, 91]. The value of q is calculated using (4.1) where, m denotes the number of phases of the current applied to the stator and n_s denotes the number of stator slots. To achieve the fractional value of q, with the value of $p_1 = 4$ the number of stator slots chosen is $n_s = 30$. This gives the number of slots per pole per phase, $q = 1.25$.

$$q = \frac{n_s}{m(2p_1)} \qquad (4.1)$$

In order to fit the stator inside the MG, the outer radius of the stator is matched to the inner radius of the inner rotor with an air gap of 0.5 mm in between. To decide on the inner radius, r_{is} of the stator, a quick parametric sweep analysis has been performed by varying r_{is} and keeping all other geometric parameters fixed. The thickness of the stator back iron was fixed at 15 mm and the volume torque density of the MG with stator fitted inside is plotted for each variation of r_{is}. The plot is shown in Figure 4-7.

From Figure 4-7, the value of r_{is} was chosen to be 35 mm. One of the reasons being there was no significant compromise with the achievable volume torque density. Also, considerably less material would be required to build the stator compared to designs with lower value of r_{is}. The final values of the geometric parameters of the stator, obtained after the analysis, are specified in Table 4.3. The final geometric design of the MGM is shown in Figure 4-8.
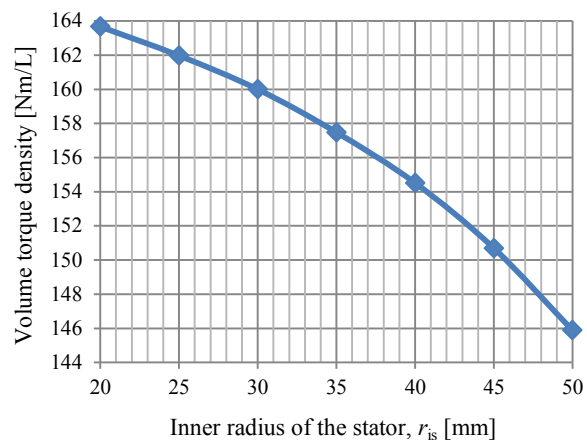
Figure 4-7: Variation of the volume torque density with the
inner radius of stator fitted inside the 8.5:1 MG

TABLE 4.3.
FINAL GEOMETRIC PARAMETERS OF THE STATOR
OF 8.5:1 MGM

	Description	Value	Unit
Stator	Inner radius of stator, r_{is}	35	mm
	Outer radius of stator, r_{os}	89.5	mm
	Back iron thickness, t_s	15	mm
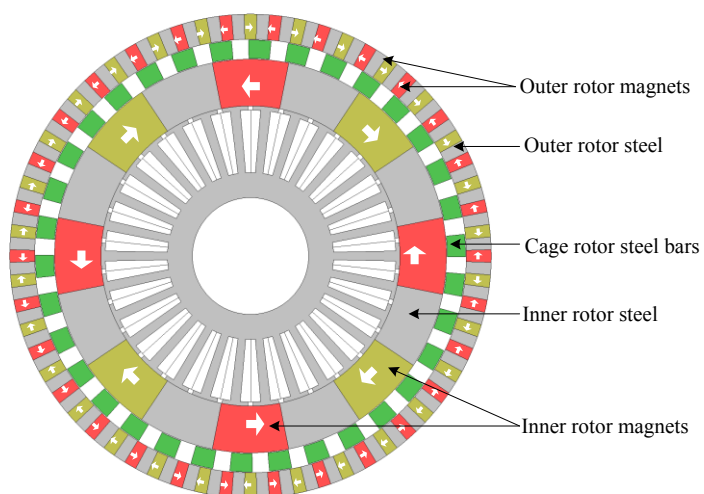
Figure 4-8: Inner stator MGM with a gear ratio of 8.5:1

The MGM was at first simulated using 2D-FEA without adding current excitation to the stator. Figure 4-9 shows the plot of the pole slipping torque obtained as a function of low speed rotor angle.
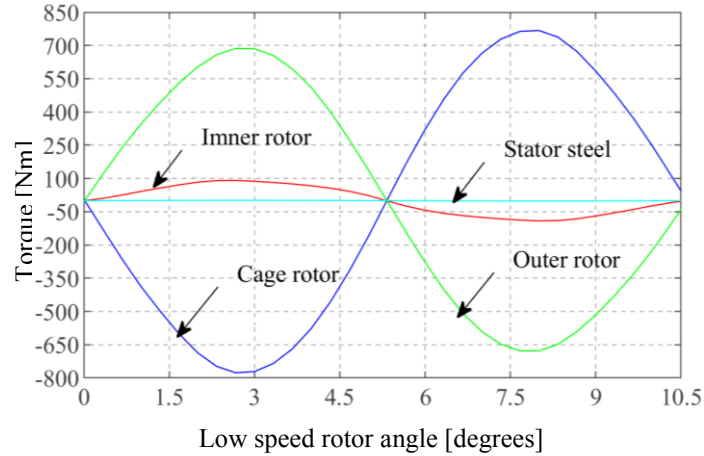
Figure 4-9: Torque produced when stator is added into the 8.5:1 MG and no current excitation is added to the stator windings

The volumetric torque density value and the torque per kg magnet mass were calculated using (2.65) and (2.67) respectively. The mass torque density is obtained using (4.2). The torque and the calculated torque density values are specified in Table 4.4.

$$T_m = \frac{T_2}{\left[\rho_s\left[\pi\left(r_{o2}^2 - r_{i2}^2\right) + \alpha_s\right] + (\rho_s + \rho_m) \times 0.5\left[\pi\left\{\left(r_{o3}^2 - r_{i3}^2\right) + \left(r_{o1}^2 - r_{i1}^2\right)\right\}\right]\right]d} \tag{4.2}$$

where, α_s is the surface area of the stator obtained from JMAG.

TABLE 4.4.
TORQUE AND TORQUE DENSITY VALUES OF 8.5:1 MG WITH
INTERNAL STATOR AND NO CURRENT EXCITATION

Description		Values	Units
Peak torque	Inner rotor	93	Nm
	Cage rotor	768	Nm
	Outer rotor	710	Nm
Volume torque density		154	Nm/L
Mass torque density		29	Nm/kg
Torque per kg magnet mass		86	Nm/kg

The torque and the torque density values reduced significantly when stator was added to the MG, with no current excitation. With the addition of current excitation, the torque will reduce further. One of the main criteria in designing the MGM was to build a machine with high torque density values, higher than that specified in Table 4.4. To enhance the torque and consequently the torque densities, two rings of Halbach magnets were embedded in the steel, placed between the circumferentially magnetized magnets of the inner rotor. The Halbach magnets increase the flux concentration in the air gap, thereby increasing the torque and the torque densities. Such a design is shown in Figure 4-10. The magnets were designed to have a radial thickness of about 7 mm and spaced 3 mm apart from the inner and outer radii of the inner rotor. This design was simulated using 2-D FEA and the pole slipping torque produced as a function of the low speed rotor angle is shown in Figure 4-11.
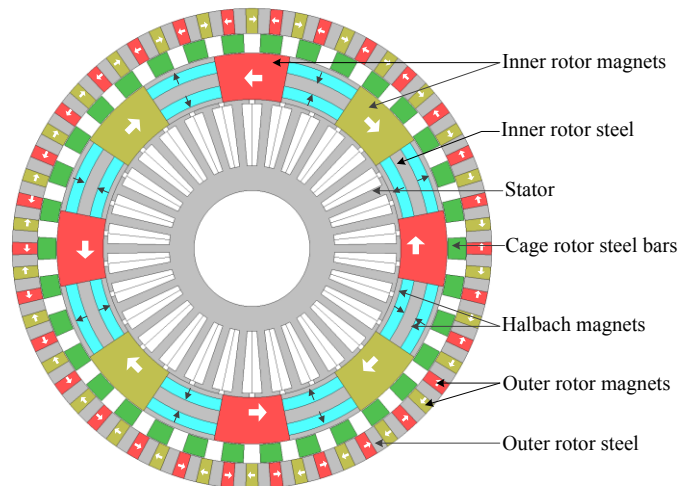
Figure 4-10: Inner stator MGM with a gear ratio of 8.5:1 and Halbach magnets embedded on the inner rotor
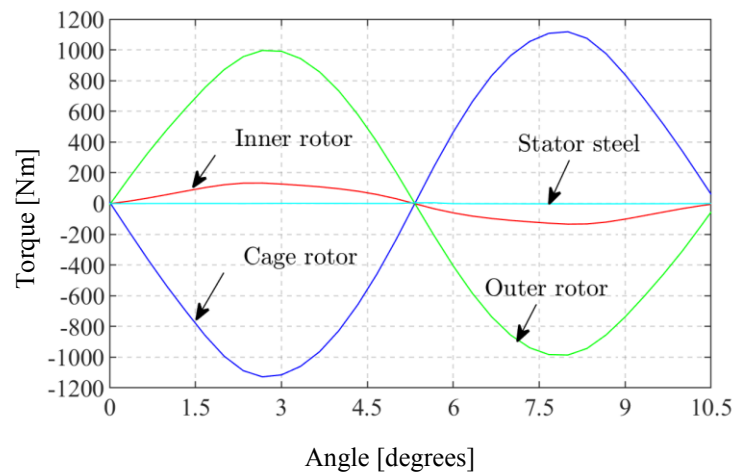
Figure 4-11: Torque produced by the inner stator MGM with Halbach magnets on the inner rotor

The volumetric torque density was calculated using (2.65). The mass torque density and the torque per kg magnet mass are calculated using (4.3) and (4.4). The torque and the torque density values are specified in Table 4.5.

$$T_m = \frac{T_2}{\left[\rho_s\left[\pi\left(r_{o2}^2 - r_{i2}^2\right) + \alpha_s\right] + \left[\pi(\rho_s + \rho_m) \times 0.5\left\{\left(r_{o3}^2 - r_{i3}^2\right) + \left(r_{o1}^2 - r_{i1}^2\right)\right\}\right] + \left[\rho_m\alpha_m - \rho_s\alpha_m\right]\right]d} \qquad (4.3)$$

where, α_m is the total surface area of the Halbach magnets.

$$T_{mm} = \frac{T_2}{\left[0.5\pi\left\{\left(r_{o3}^2 - r_{i3}^2\right) + \left(r_{o1}^2 - r_{i1}^2\right)\right\} + \alpha_m\right]\rho_m d} \qquad (4.4)$$

TABLE 4.5.
TORQUE AND TORQUE DENSITY VALUES OF 8.5:1 MG WITH
STATOR AND HALBACH MAGNETS

Description		Values	Units
Peak torque	Inner rotor	133	Nm
	Cage rotor	1127	Nm
	Outer rotor	996	Nm
Volume torque density		227	Nm/L
Mass torque density		43	Nm/kg
Torque per kg magnet mass		98	Nm/kg

Comparing the torque and the torque density values shown in Table 4.4 and Table 4.5, it can be concluded that with the addition of the Halbach magnets, the torque and volume torque density increased by 47%. However, the torque and the torque density values are still low when compared to the MG design without the stator. Thus it can be inferred that the torque and the torque densities of the MG with the stator fitted inside is considerably lower than what obtained without the stator. This lower torque density of the MGM was improved further by using Halbach magnets on the inner rotor.

4.2.1.1 *Stator Winding Design for Fractional Slot Stator*

In order to design the fractional slot winding, the star of slots method [92] has been adopted. This method uses a graphical representation to determine the winding distribution. The method focuses on finding the proper coil connections in order to maximize the main harmonics of the EMF induced in the windings. It can be utilized not only for the analysis of the main EMF waveform but also its harmonics as well as the harmonics of the air gap MMF distribution. The star of slots is formed by n_s phasors. These phasors are distributed such that, the main EMF harmonic induced in the coil sides of each slot is characterized by n_s/t spokes, t being the periodicity of the machine and is given by

$$t = GCD(n_s, p_1) \tag{4.5}$$

where, GCD is the greatest common divisor.

Again, the required number of slots per pole is given by

$$\text{Slots-per-pole} = \frac{n_s}{2p_1} = \frac{15}{4} \tag{4.6}$$

This implies that 4 poles must be distributed over 15 slots and the 3 phase winding pattern will then be repeated after 4 poles are wound.

The number of slots per phase can be obtained from

$$\text{Slots-per-phase} = \frac{n_s}{m} = 10 \tag{4.7}$$

The electrical phase angle between each slot is calculated as

$$Q_s = \frac{2p_1 \times 180}{n_s} = 48 \qquad (4.8)$$

A coil span should be chosen such that the electrical phase angle between two sides of the coil is as close to 180^0 electrical as possible. Thus the coil span chosen is 4 since $48^0 \times 4 = 192^0$ is the closest to 180^0 elctrical. So, a coil coming out of slot 1 will enter slot 5 i.e.(coil span + 1). The star of slots is illustrated in Figure 4-12(a) and the winding distribution achieved using the star of slots technique is shown in Figure 4-12(b). The winding layout is realized by representing the coil connections in a linear arrangement for each of the three phases. This is followed by the turns function and the winding function for each of the three phases. The resultant MMF wave is obtained subsequently by combining the winding functions for each of the three phases. The winding layout based on the winding distribution is shown in Figure 4-13. The turns function is shown in Figure 4-14.
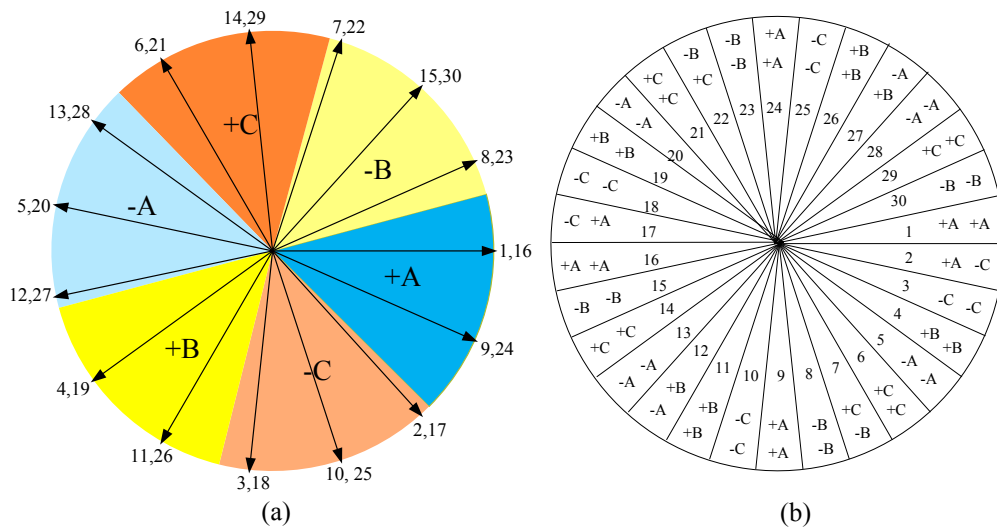
Figure 4-12: (a) Star of slots phasor diagram and (b) winding distribution of a 30 slots 8 poles
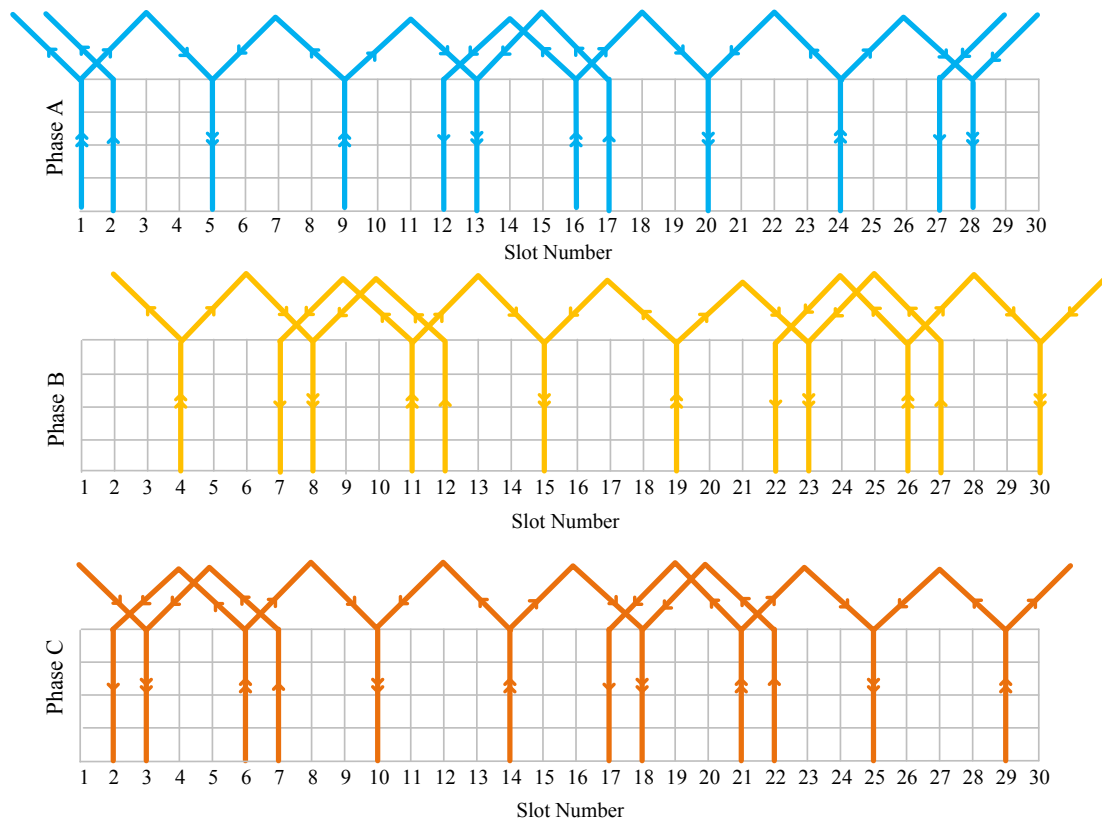
Figure 4-13: Winding layout of a 3 phase stator with 30 slots and generating 4 pole pairs
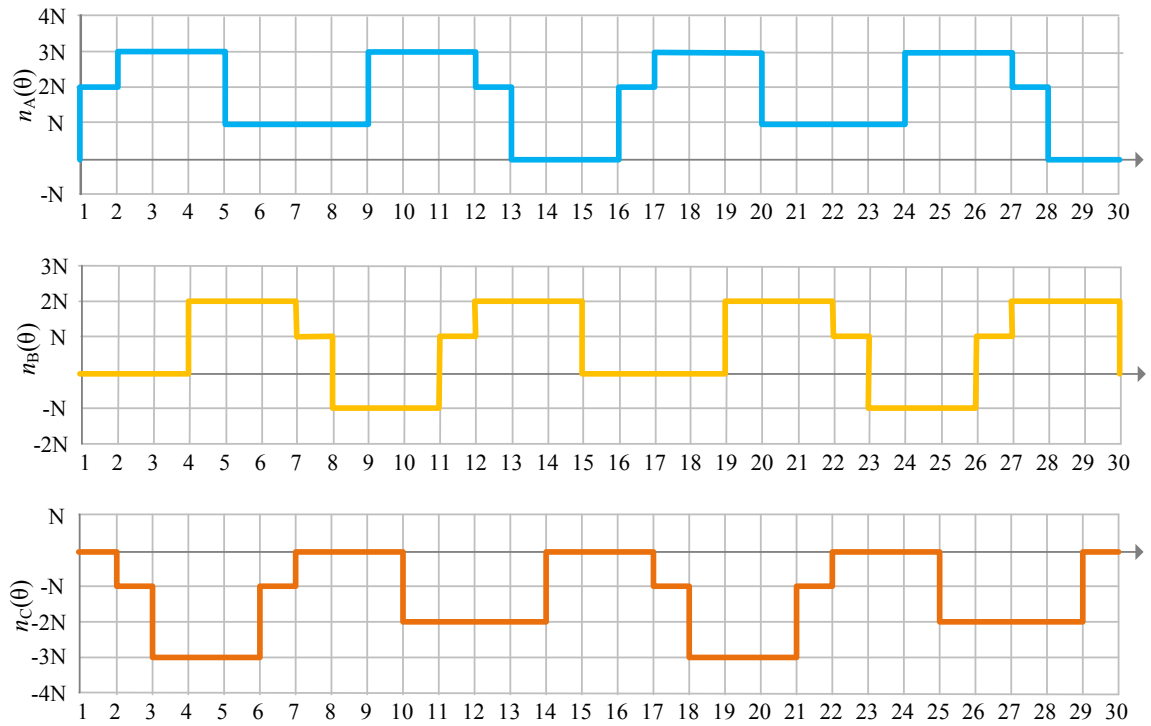
Figure 4-14: Turns function of a 3 phase stator with 30 slots and generating 4 pole pairs

The winding function i.e. the MMF per unit current for each of the 3 phases can be calculated from the turns function using

Winding function = Turns function - average value of turns function

$$\text{or,} \qquad N(\theta) = n(\theta) - \langle n(\theta) \rangle \tag{4.9}$$

The average value of a waveform can be computed using

Average of a waveform = (Area under the waveform over full cycle) / (period of cycle) (4.10)

The winding function obtained using (4.9) is shown in Figure 4-15.
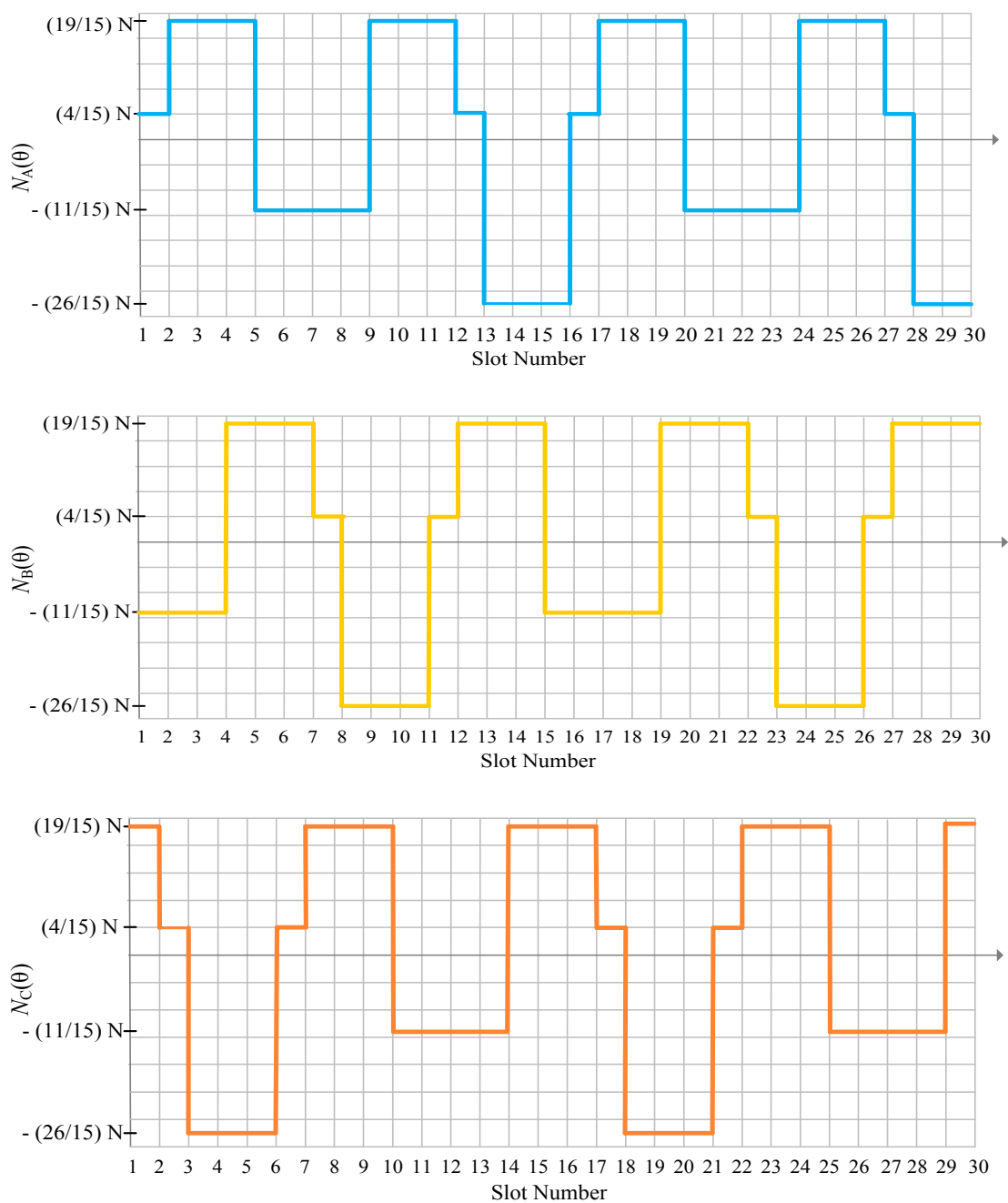
Figure 4-15: Winding function of a 3 phase stator with 30 slots and generating 4 pole pairs

To obtain the resultant MMF, the winding functions should be multiplied by the instantaneous values of the phase currents. Since the three phase currents are phase shifted by 120 degree electrical, at time t = 0,

$$i_A = 1A, \ i_B = i_C = -0.5A \qquad (4.11)$$

The resultant MMF wave could be obtained by multiplying the winding functions with the instantaneous values of the phase currents and summing them up. This is represented mathematically in (4.12). Substituting (4.11) in (4.12) we get (4.13).

$$MMF(\theta) = N_A(\theta)i_A(t) + N_B(\theta)i_B(t) + N_C(\theta)i_C(t) \qquad (4.12)$$

$$MMF(\theta) = N_A(\theta) - 0.5N_B(\theta) - 0.5N_C(\theta) \qquad (4.13)$$

The combined winding function is shown in Figure 4-16. It confirms the formation of 4 pole pairs using the stator winding design. Thus it can be stated that with the coil connections obtained using the star of slots method, same number of pole pairs as the inner rotor is achieved.
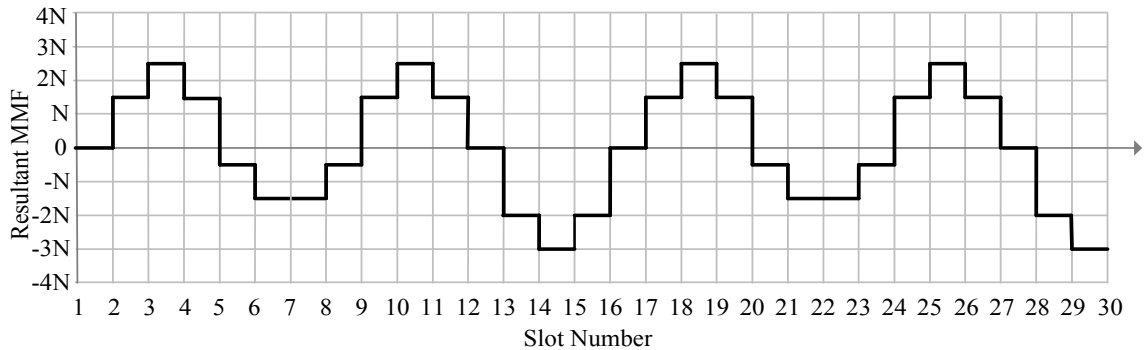
Figure 4-16.Combined winding function of the 30 slots, 3 phase 4 pole pair

In order to simulate the MGM design using 2D FEA analysis method, the circuit parameters should be computed. This includes calculating the number of winding turns, N; the winding resistance, R; and the maximum value of the current, I_{max} required for stator excitation. A summary of the other parameters used for the calculation are as shown in Table 4.6. The geometric parameters required are illustrated in Figure 4-17.

TABLE 4.6
PARAMETERS FOR THE CALCULATION OF STATOR COIL RESISTANCE
AND NUMBER OF TURNS

Parameters	Description	Value	Unit
A_{sl}	Slot cross sectional area	170	mm^2
Φ_d	Coil diameter	1	mm
A_c	Coil cross sectional area	0.785	mm^2
ξ_p	Packing factor	0.5	-
d	Stack length	75	mm
ρ	Copper resistivity	1.68x10^{-5}	Ω-mm
I	Current density,	2.5	Amp/ mm^2
b_{st}	Stator teeth width	6	mm
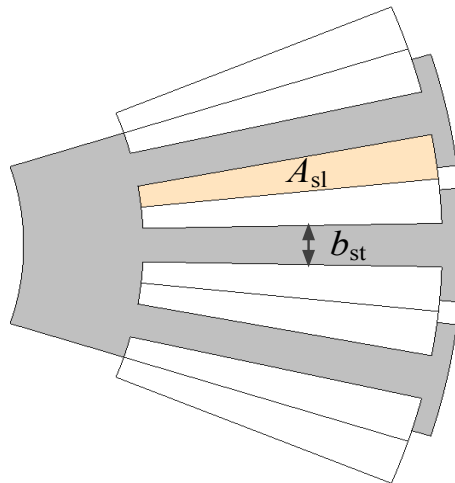
Figure 4-17:Geometry parameter definition
of stator

Using a packing factor of ξ_p= 0.5, the slot surface area used by the coil conductors is given by

$$A_s = \xi_p \times A_{sl} \tag{4.14}$$

or,
$$A_s = 85 \ mm^2 \tag{4.15}$$

The number of turns for each coil in the slot

$$N = \frac{A_s}{A_c} \tag{4.16}$$

or,
$$N = 109 \tag{4.17}$$

The resistance of the coil is calculated from [93]

$$R = \frac{\rho L}{A_c} \tag{4.18}$$

where, L *is* the length of the coil and ρ is the resistivity of the coil material. The length of the coil considering the stack length, d of the machine and the stator teeth width b_{st} can be obtained from,

$$L = 2(d + 4b_{st}) \tag{4.19}$$

or,
$$L = 198 \ mm \tag{4.20}$$

The resistance of the coil obtained using (4.18) is

$$R = 0.00423 \ \Omega \tag{4.21}$$

The rms value of the current I_{rms} is calculated from the current density, area of slots and the number of turns N using (4.22). The area of each slot as calculated from JMAG is 170 mm^2.

$$\frac{N \times I_{rms}}{Area} = 2.5 \tag{4.22}$$

Using the value of $N = 109$, we obtain,

$$I_{rms} = 3.9 \text{ A} \tag{4.23}$$

or,
$$I_m = 5.52 \text{ A} \tag{4.24}$$

The frequency of the current applied used is $f = 113.33$, calculated from the speed and the number of pole pairs of the inner rotor.

The final design for the fractional slot inner stator MGM is shown in Figure 4-18. The three phase windings are marked in three different colors. The direction of current for phase A is marked as shown in Figure 4-18.

Figure 4-18:A 8.5:1 fractional slot inner stator MGM with Halbach magnets and direction of current marked for phase A

4.2.1.2 *Harmonic Analysis*

The harmonic analysis has been conducted in two stages. In the first stage, the analysis has been performed on the magnetic flux density produced by the stator windings when three phase excitation was added. This was done to ensure that the stator produces the harmonic corresponding to the number of pole pairs that it was designed for. In the next stage, the analysis has been performed on the radial magnetic flux densities produced in the three air gaps existing between the stator and inner rotor; between the inner rotor and cage rotor and between the cage rotor and the outer rotor. This was done to find the dominant harmonics that would contribute to the torque transmission between the rotors.

The magnetic flux density produced when the stator excitation is applied and no other rotor is present is shown in Figure 4-19. A harmonic analysis conducted on the magnetic flux density established the 4th harmonic as the dominant harmonic and is shown in Figure 4-20.
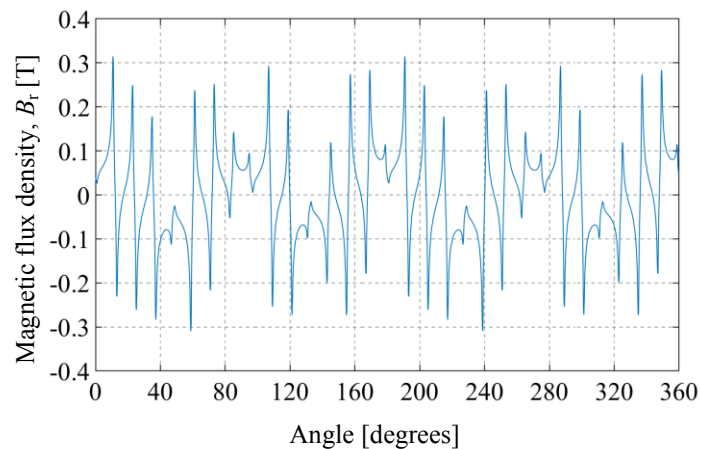
Figure 4-19: Radial magnetic flux density, B_r in the air gap between the stator and the inner rotor
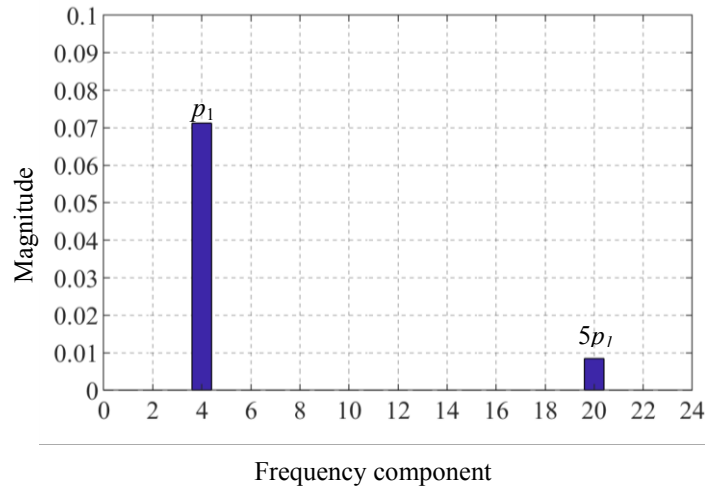
Figure 4-20: Harmonic components of the magnetic flux density, B_r at 89.5 mm radius when three phase excitation is applied to the stator

The radial flux density at the air gap between the stator and the inner rotor and its harmonic components are shown in Figure 4-21(a) and (b) respectively. It shows the production of p_1= 4 pole pairs in the air gap between the stator and the inner rotor. The radial flux density waveform in the air gap adjacent to the outer rotor due to p_1= 4 pole pairs on the the inner rotor, both with and without the cage rotor steel pieces is shown in Figure 4-22(a). The associated harmonic analysis is shown in Figure 4-22 (b). It shows that the introduction of the n_2=34 steel pieces of the cage rotor results in a dominant 30th harmonic in the air gap adjacent to the outer rotor. This harmonic field interacts with the p_3= 30 pole pairs of the outer rotor and transmit torque.
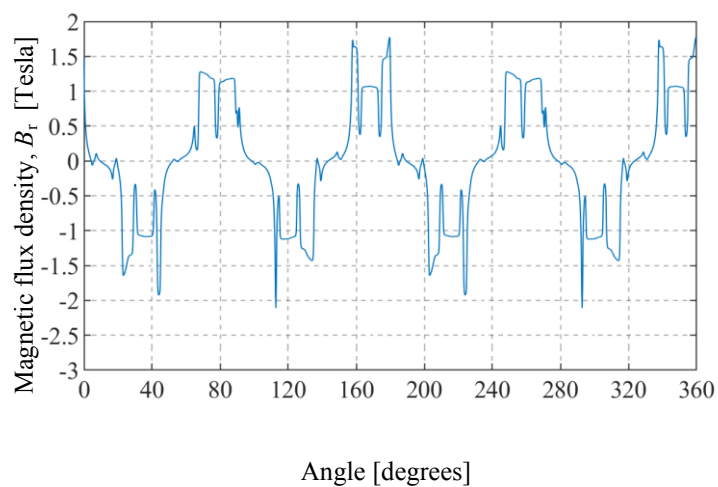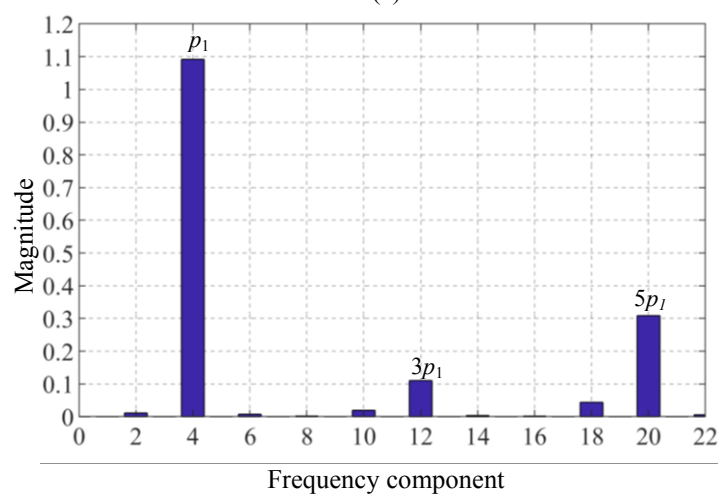
Figure 4-21: (a) Radial flux density in the air gap between stator and inner rotor, (b) harmonic analysis of the radial flux density at the inner air gap
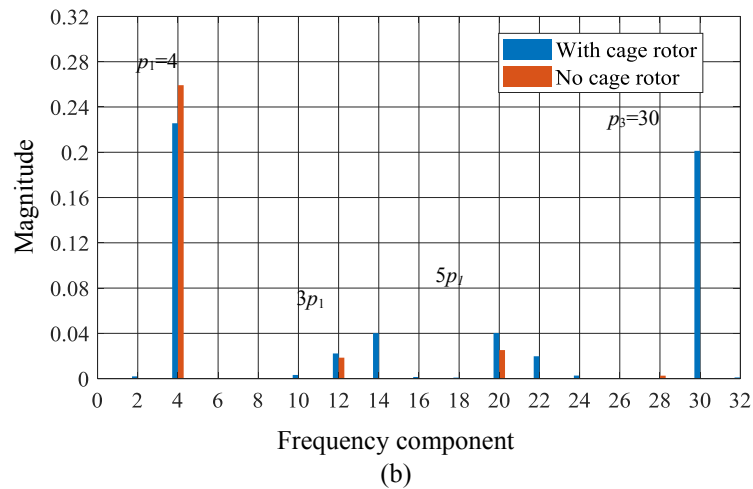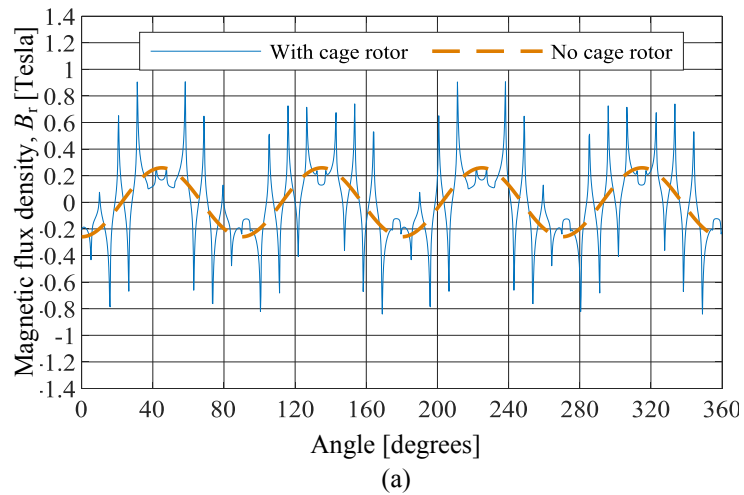
Figure 4-22: (a) Radial flux density and(b) harmonic analysis of the radial flux density due to permanent magnets on the inner rotor in the outer air gap

Similarly, Figure 4-23(a) and (b) shows the radial magnetic flux density and its harmonics due to $p_3=30$ pole pairs of the outer rotor, in the air gap adjacent to the inner rotor, with and without $n_2=34$ steel pieces of the cage rotor. It shows that the addition of the steel pieces of the cage rotor results in 4 pole pairs which interacts with the $p_1=4$ pole pairs of the inner rotor.
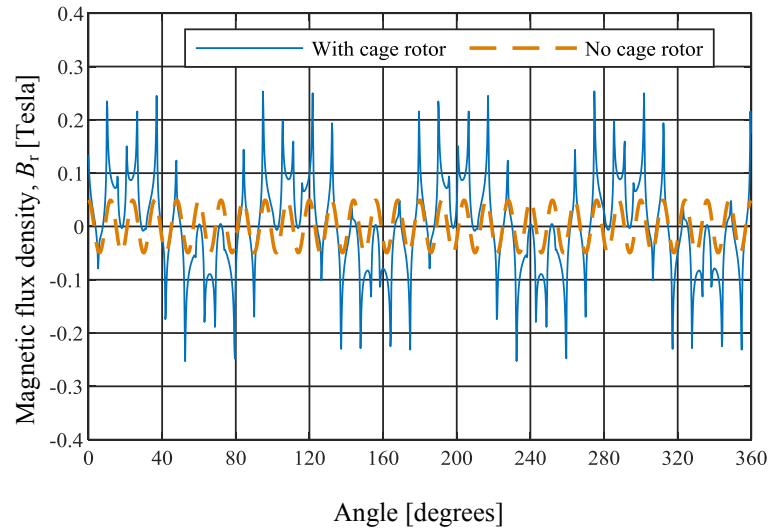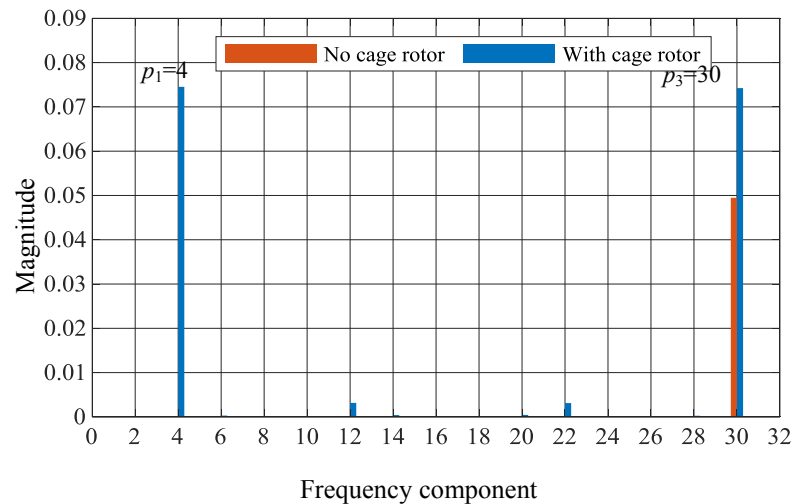
Figure 4-23:(a) Radial flux density and(b) harmonic analysis of the radial flux density due to permanent magnets on the outer rotor in the inner air gap

The fractional slot inner stator MGM design was simulated using 2D FEA with the three phase current applied to the stator. The steady state torque produced by the machine as a function of low speed rotor angle is shown in Figure 4-24. The torque and the torque density values are mentioned in Table 4.7. Whilst the torque density magnitude is high, the torque ripple is high. The torque ripple is 50 Nm i.e. 4% for the low speed cage rotor and 150 Nm i.e. 13% for the high speed inner rotor.
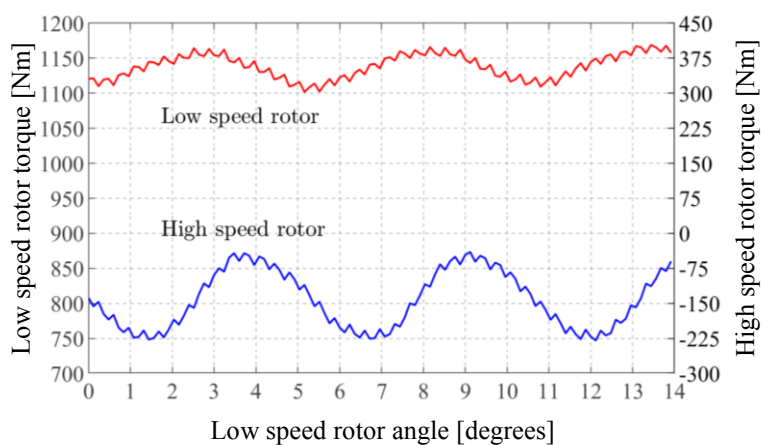
Figure 4-24**:** Torque produced by an 8.5:1 fractional slot inner stator MGM when three phase current is applied to the stator windings.

TABLE 4.7
TORQUE AND TORQUE DENSITY VALUES WITH
CURRENT APPLIED TO THE STATOR

	Description	Values	Units
Average torque	Inner rotor	143	Nm
	Cage rotor	1138	Nm
	Outer rotor	1004	Nm
	Stator steel	7.8	Nm
Volume torque density		229	Nm/L
Mass torque density		40	Nm/kg
Torque per kg magnet mass		126	Nm/kg

4.2.2   Integer Slot Inner Stator MGM Design

In this section the MGM performance is studied when using an integral slot stator rather than a fractional slot stator. A stator where the number of slots per pole per phase, q is an integer. is known as an integral slot stator [94]. The number of slots $n_s = 24$ is chosen such that an integer value of $q =1$ is obtained using (4.1) . This stator with 24 slots should be fitted on the inside of the MG presented in section 4.2. The outer radius of the stator is constrained by the inner radius of the inner rotor with an air gap of 0.5 mm in between. In order to select the inner radius of the stator, a parametric sweep analysis similar to that used in the case of the fractional slot inner stator design has been adopted. The variation of the volumetric torque density with the inner radius of the stator thus obtained, is shown in Figure 4-25. The inner radius of the stator was chosen to be $r_{is} = 45$ mm. The MGM design achieved after finalizing the stator geometry and integrating it with the MG shown in Figure 4-26.
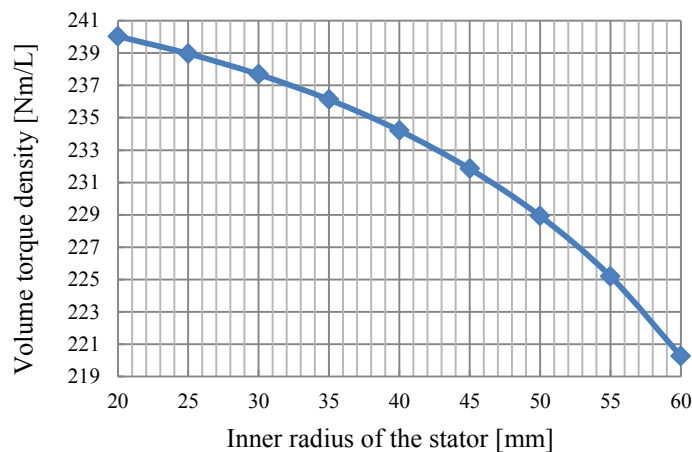
Figure 4-25: Variation of the volumetric torque density with the inner radius of the stator of an 8.5:1 integral slot inner stator MGM design
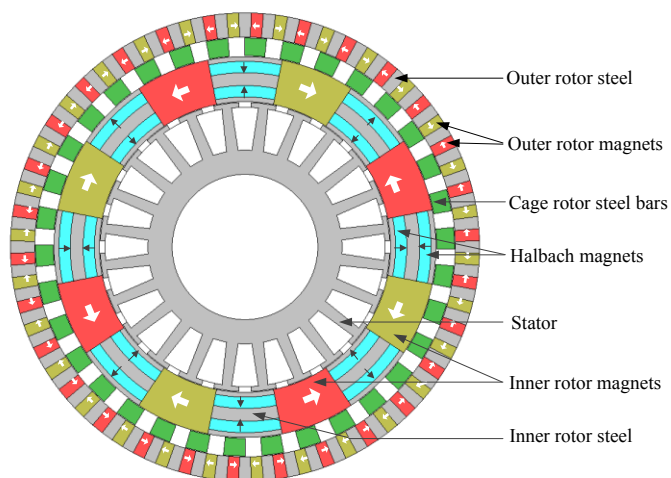
Figure 4-26: Integral slot inner stator MGM with a gear ratio of 8.5:1

The design was first simulated without any stator excitation. The steady state torque as a function of the low speed rotor angle is plotted in Figure 4-27. The 2D FEA calculated peak torque and the torque density values are shown in Table 4.8.
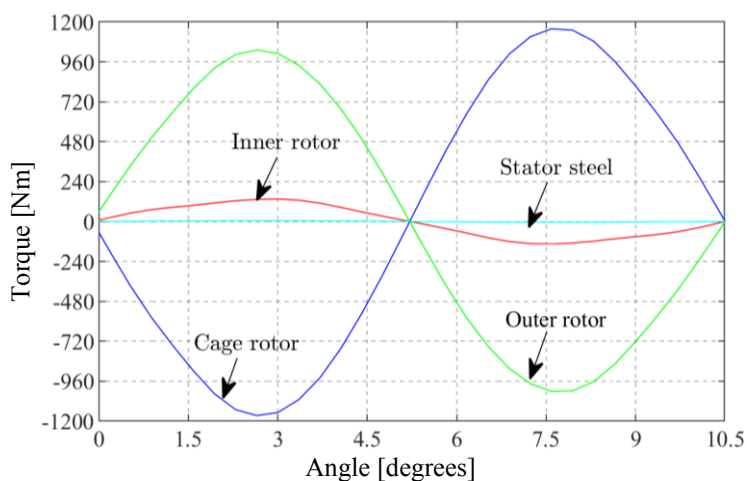
Figure 4-27: Torque produced in an 8.5:1 integral slot inner stator MGM when no current is applied to the stator windings

Comparing Table 4.5 and Table 4.8, it can be inferred that the torque and the torque density values are almost the same when fractional slot inner stator and integral slot inner stator designs are simulated without current excitation added to it.

TABLE 4.8.
TORQUE AND TORQUE DENSITY VALUES OF 8.5:1
INTEGRAL STATOR MGM WITHOUT CURRENT

Description		Values	Units
Peak torque	Inner rotor	136	Nm
	Cage rotor	1160	Nm
	Outer rotor	1030	Nm
Volume torque density		226	Nm/L
Mass torque density		40	Nm/kg
Torque per kg magnet mass		127	Nm/kg

The stator winding is designed for the production of 4 pole pairs, using the same procedure of star of slots used in the case of designing the fractional slot stator windings. The number of slots per pole is $n_s/(2p_1) = 3$. As we have m=3 phases, the number of slots per phase is $n_s/m = 8$. The electrical phase angle calculated between each slot is given by $\theta_e = (180 \times 8)/24 = 60^0$ electrical. Since each pole spans 180^0 electrical, the coil span chosen is 3. So, a coil coming out of slot 1 will enter slot 4 i.e. (coil span + 1). The star of slots of the winding design is illustrated in Figure 4-28(a) and the winding layout obtained is shown in Figure 4-28(b). The winding function obtained for the 3 phases is shown in Figure 4-29. The winding functions with the application of 3 phase current is shown in Figure 4-30. The resultant MMF waveform is shown in Figure 4-31.

(a)   (b)
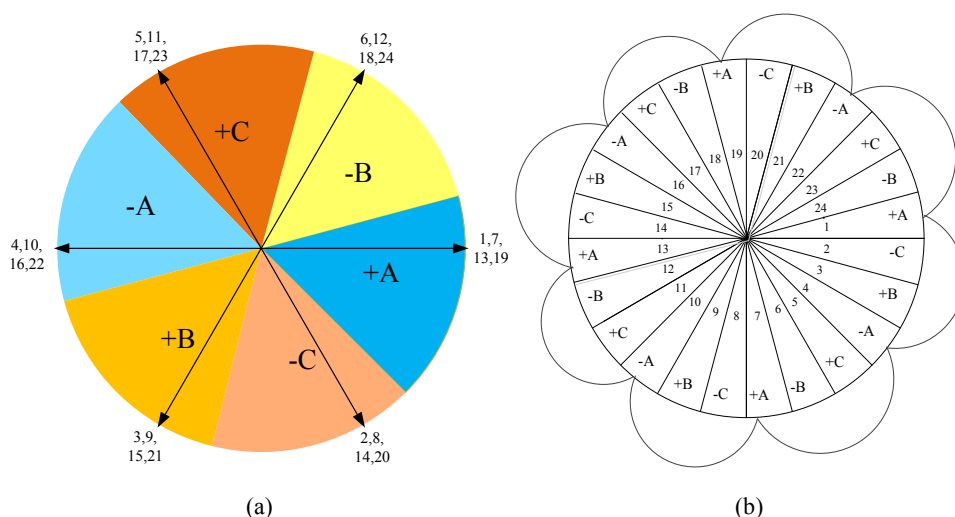
Figure 4-28 : (a) Star of slots phasor diagram and (b) winding distribution of a 24 slots 8 poles
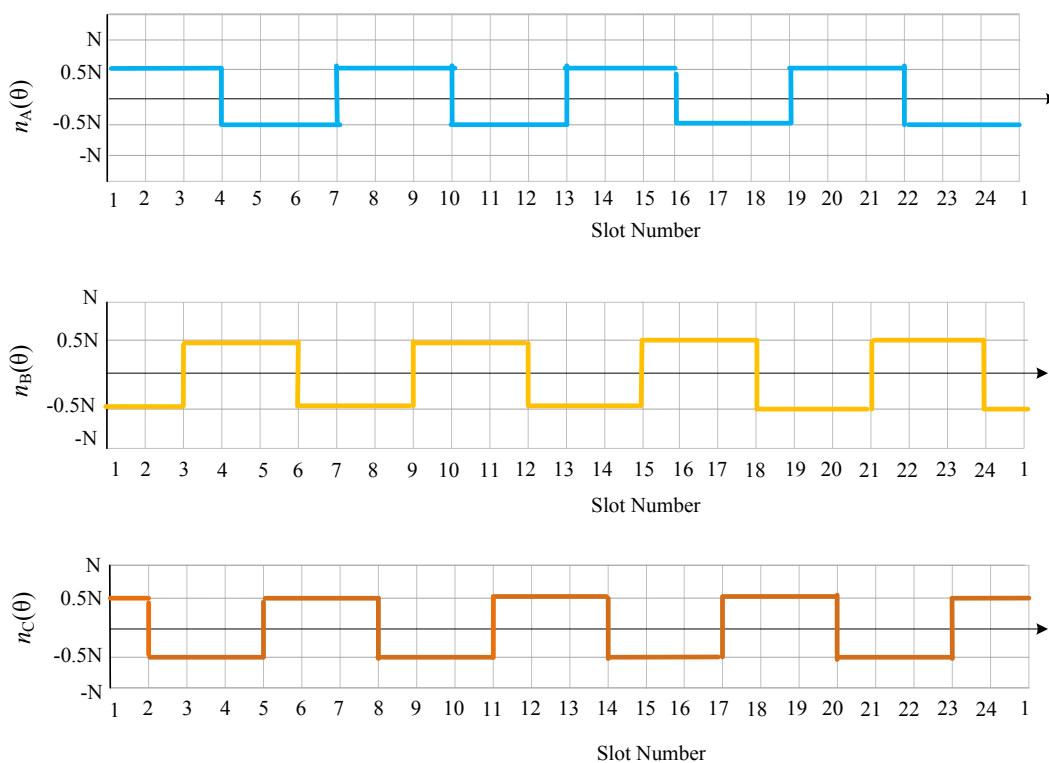
Figure 4-29: Turns function for 24 slots 4 pole pair design
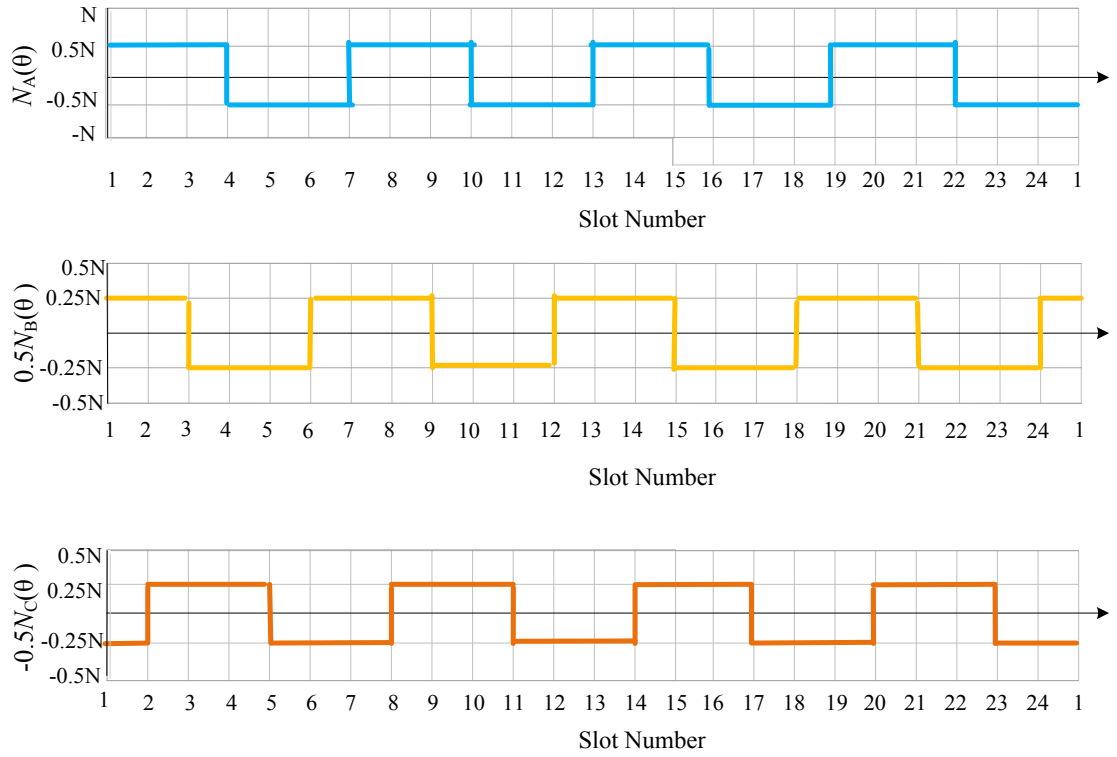
Figure 4-30: Winding function for 24 slots 4 pole pair design with the application of current
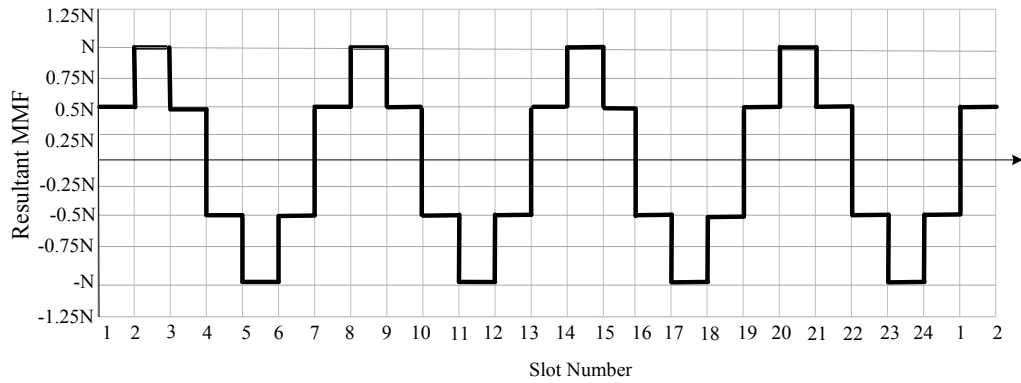
Figure 4-31:Combined winding function of the 24 slots, 3 phase 4 pole pair

4.2.2.1 *Harmonic Analysis*

A harmonic analysis of the waveform shown in Figure 4-31 using the Fourier series [96] defined in (4.25) was conducted.

$$MMF(\theta) = a_v + \sum_{n=1}^{\infty} \left[a_n \cos(nk_0\theta) + b_n \sin(nk_0\theta) \right] \tag{4.25}$$

where, a_v is the average value,

a_n and b_n are the Fourier coefficients and

$$k_0 = \frac{2\pi}{T} \tag{4.26}$$

where nk_0 are called the harmonic frequencies and T is the period of the waveform.

Since each of the waveforms have quarter wave odd symmetry,

$$a_v = 0$$
$$a_n = 0 \tag{4.27}$$

The Fourier coefficients are evaluated using

$$b_n = \frac{1}{T} \int_0^T MMF(\theta) \sin(\frac{2n\pi\theta}{T}) d\theta \tag{4.28}$$

where, $T = \frac{\pi}{2}$

Evaluating yields

$$b_n = \frac{N}{2n\pi} \left(1 - \cos n\pi + \cos\frac{n\pi}{3} - \cos\frac{2n\pi}{3} \right) \tag{4.29}$$

The values of Fourier coefficients, b_n and harmonic frequencies, nk_0 computed for each n are specified in Table 4.9. From the table it is evident that the 4th, the 20th and the 28th harmonics are the dominant components.

TABLE 4.9
FOURIER COEFFICIENTS AND
HARMONICS

n	b_n	nk_0
1	$3N/2\pi$	4
2	0	8
3	0	12
4	0	16
5	$3N/10\pi$	20
6	0	24
7	$3N/14\pi$	28
8	0	32
9	0	36

The Fourier series as shown in can be written as

$$MMF(\theta) = \frac{3N}{2\pi}\left[\sin(4\theta) + \frac{1}{5}\sin(20\theta) + \frac{1}{7}\sin(28\theta) + \ldots\ldots\right] \tag{4.30}$$

Or,
$$MMF(\theta) = \frac{3N}{2\pi}\sin(p\theta) + \sum_{n=3}^{\infty}\left[\sin(2n-1)p\theta\right] \tag{4.31}$$

The resultant MMF regenerated in Matlab using (4.30) is shown in Figure 4-32.
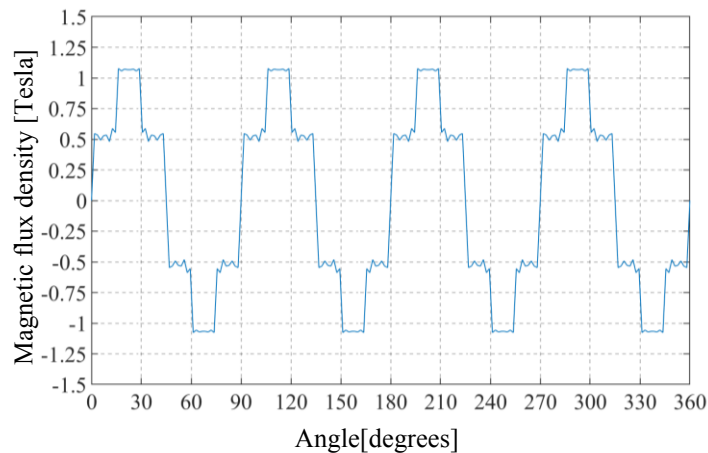
Figure 4-32:Resultant MMF regenerated by Matlab using
Fourier series analysis

A harmonic analysis was performed on the radial magnetic flux density produced by the stator windings using the field data obtained from the 2D FEA simulation. The radial magnetic flux density in the air gap and the corresponding harmonic analysis terms are shown in Figure 4-33. This agrees with the winding function.
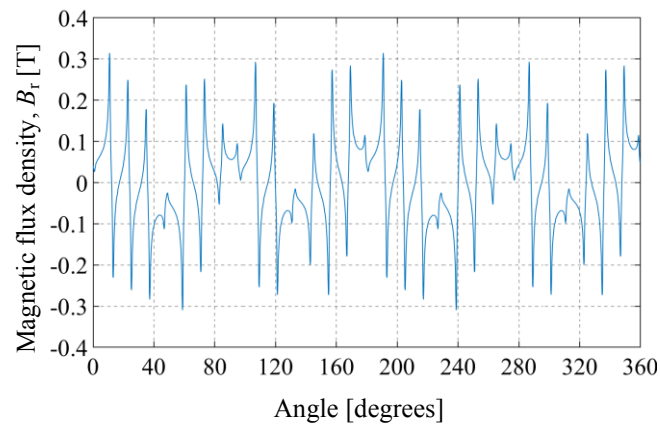
(a)
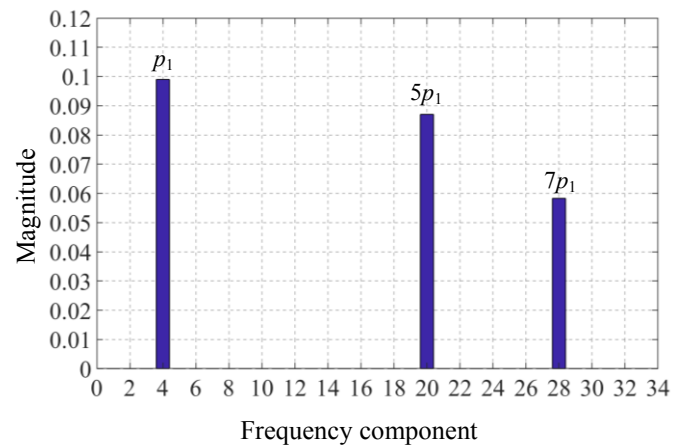
(b)

Figure 4-33: (a) Radial magnetic flux density at the air gap between the stator and the inner rotor and (b) the harmonic components of the flux density

Similar analyses performed on the radial magnetic flux density at the air gaps adjacent to the inner rotor and the outer rotor are shown in Figure 4-34 and Figure 4-35. As expected, it shows that the 4th harmonic and its odd multiples along with the 30th harmonic are dominant.

(a)

Frequency component
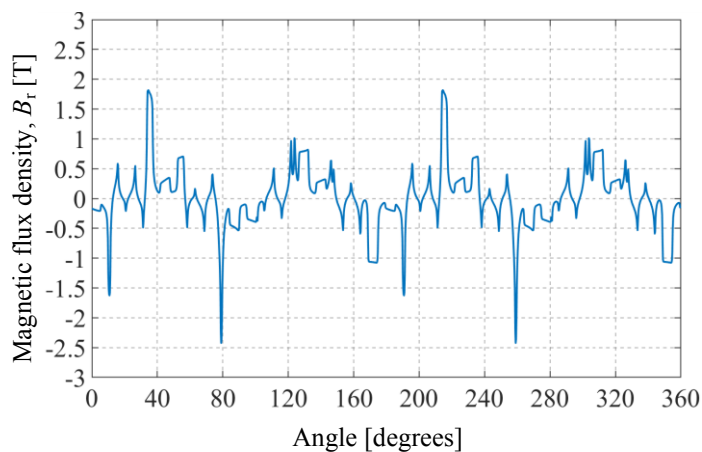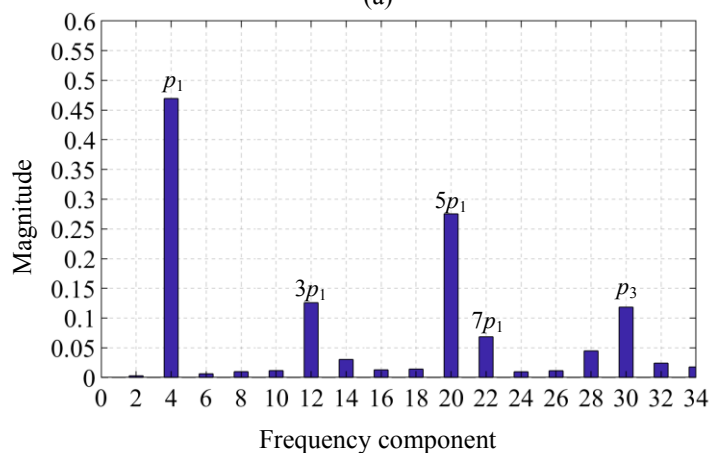
Figure 4-34:(a) Radial magnetic flux density at the air gap between the inner rotor and the cage rotor (b) the harmonic components of the flux density
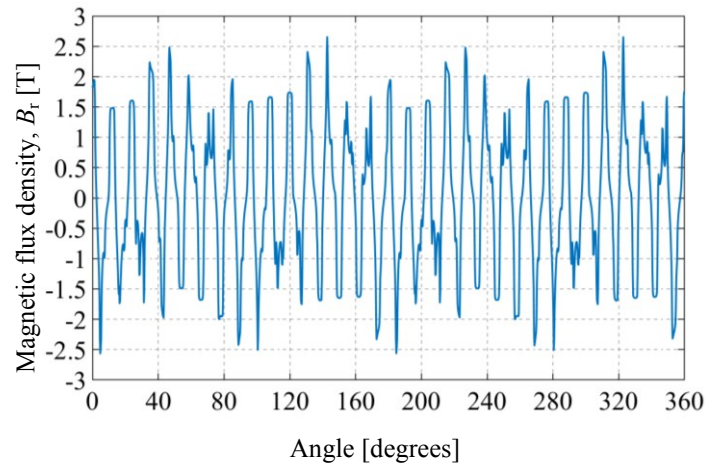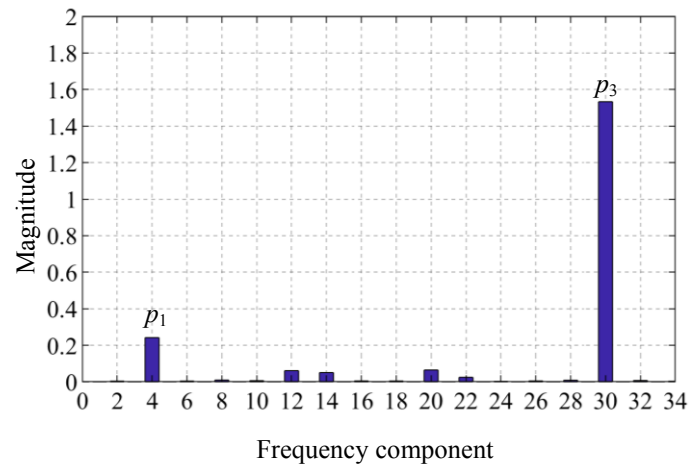
Figure 4-35:(a) Radial magnetic flux density at the air gap between the cage rotor and the outer rotor and (b) the harmonic components of the flux density

4.2.2.2 *Simulation Parameters Calculation*

The number of turns, the winding resistance and the rms and maximum values of the current required for stator excitation are calculated using the same procedure as used for the fractional slot winding design. Most of the parameters used are the same as that of the fractional slot inner stator design and are specified in Table 4.6. with the exception of the slot cross sectional area which is $A_{sl} = 556$ mm^2 for the current stator design. The geometric parameters required are illustrated in Figure 4-36.
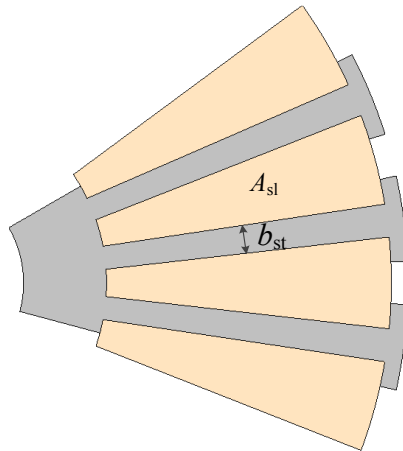
Figure 4-36: Geometry parameter
definition of stator

Using a packing factor of $\xi_p = 0.5$, the slot surface area, A_s used by the coil conductors is obtained using (4.14).

$$A_s = 148 \text{ mm}^2 \tag{4.32}$$

The number of turns, N for each coil in the slot is calculated using (4.16) . Thus $N=189$. The resistance of the coil is calculated from (4.18) where; L is the length of coil is given by

$$L = 2(d + 3b_{st}) \tag{4.33}$$
$$\text{or,} \quad L = 198 \text{ mm} \tag{4.34}$$

The resistance of the coil obtained is

$$R = 0.0045 \, \Omega \tag{4.35}$$

The rms value of the current I_{rms} is calculated from the current density, area of slots and the number of turns N. Using the values from Table 4.6, the maximum value of current obtained is

$$\text{or,} \quad \therefore I_m = 5.52\,\text{A} \tag{4.36}$$

The design of the integral slot inner stator MGM with the direction of current applied to each of the three phases is shown in Figure 4-37. With the parameter values finalized, the MGM design is simulated with current excitation applied to the stator. The 2D FEA calculated steady state torque generated as a function of the low speed rotor angle is shown in Figure 4-38. The calculated torque and the torque density values are shown in Table 4.10.
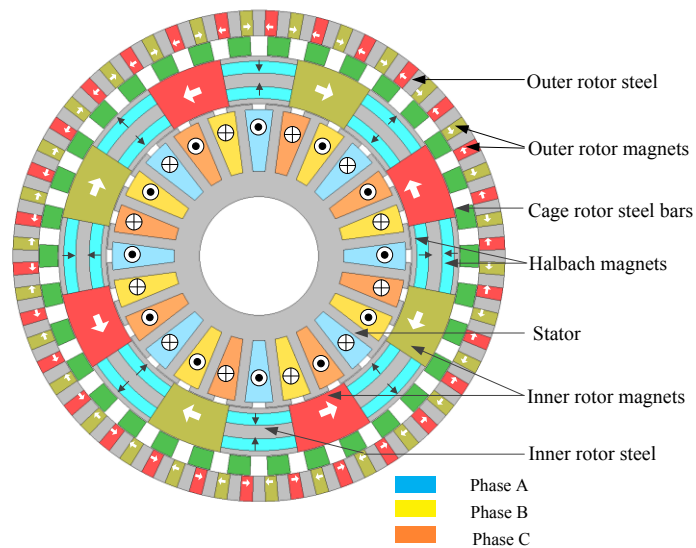
Figure 4-37: An 8.5:1 integral slot inner stator MGM with current excitation added to the stator windings
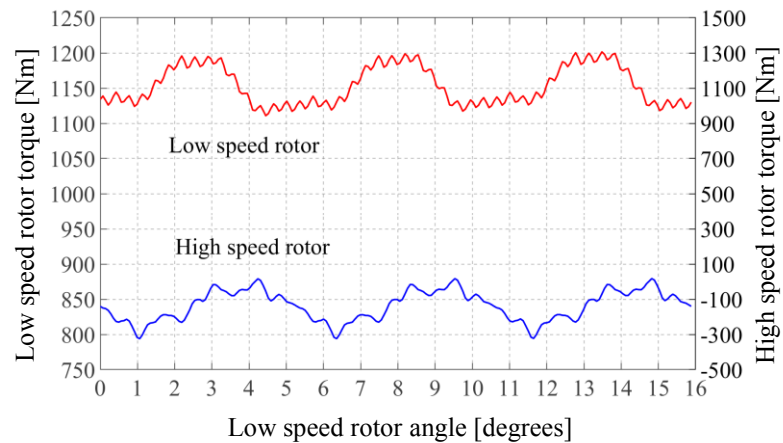
Figure 4-38: Steady peak torque produced in an 8.5:1 integral slot inner stator MGM when current excitation is applied to the stator windings

TABLE 4.10.
TORQUE AND TORQUE DENSITY VALUES OF 8.5:1 INTEGRAL
STATOR MGM WITHOUT CURRENT

Description		Values	Units
Average torque	Inner rotor	137	Nm
	Cage rotor	1153	Nm
	Outer rotor	1017	Nm
Volume torque density		224	Nm/L
Mass torque density		40	Nm/kg
Torque per kg magnet mass		126	Nm/kg

Figure 4-38 shows that this design produced a very high torque ripple of 100 Nm i.e. 8% on the low speed cage rotor and 200 Nm i.e. 16 % on high speed inner rotor. This high torque ripple makes the design not viable. In order to reduce the torque ripple, a two layer winding distribution approach was considered where each slot was radially divided into two layers, the top layer and the bottom layer. The winding of each phase was distributed between the top layer of one slot and the bottom layer of the adjacent slot i.e., each phase winding was shifted by one slot. Such a design is shown in Figure 4-39.
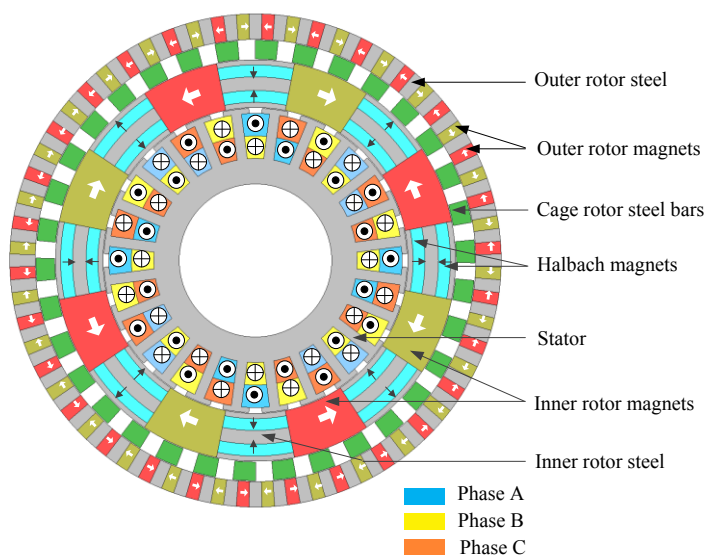
Figure 4-39: An 8.5:1 integral stator MGM with stator having 24
slots and each phase winding shifted by 1 slot

Using the simulation parameters obtained in section 4.2.2.2 and 2D FEA, this design was
simulated. The peak torque produced as a function of the angle is shown in Figure 4-40
and the torque and torque density values are shown in Table 4.11. The use of two layer
windings reduced the torque ripple by 75% from 100 Nm to 25 Nm for the low speed
cage rotor and by 81% from 200 Nm to 38 Nm for the high speed inner rotor. The torque
density only reduced by 6%.
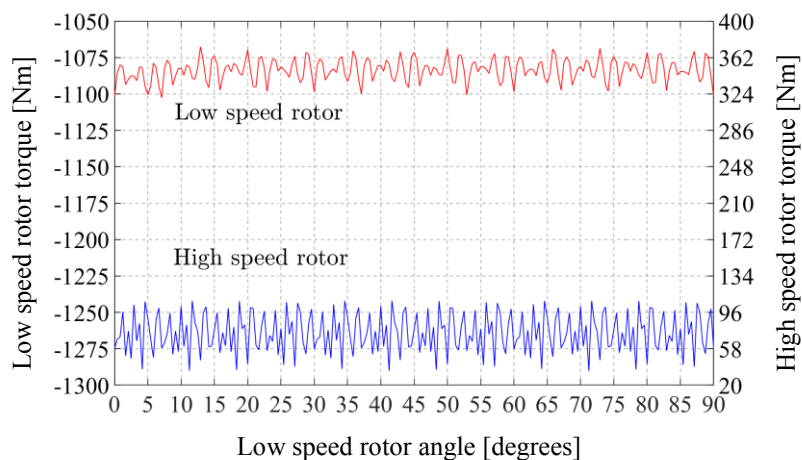
Figure 4-40: Torque as a function of low speed rotor angle
produced by an 8.5:1 internal stator MGM with each phase
winding shifted by one slot

TABLE 4.11.
TORQUE AND TORQUE DENSITY VALUES OF 8.5:1 INTEGRAL
STATOR MGM WITHOUT CURRENT

Description		Values	Units
Average torque	Inner rotor	77	Nm
	Cage rotor	1087	Nm
	Outer rotor	1010	Nm
Volume torque density		211	Nm/L
Mass torque density		37	Nm/kg
Torque per kg magnet mass		118	Nm/kg

4.2.3   Conclusion

In this chapter an inner stator MGM with a fractional slot winding and an integral slot winding was studied. Both the fractional and integral slot MGM designs produced comparable torque and torque densities of 1138 Nm, 1153 Nm and 222 Nm/L and 224 Nm/L respectively. The torque ripple produced by both designs was high, the maximum being 200 Nm on the inner rotor of the integral slot stator design. The torque ripple was mitigated by using a two layer integral slot winding design with one slot chording. This reduced the torque ripple by 80%. Thus this two layer winding design was considered a feasible design.

5   OUTER STATOR MAGNETICALLY GEARED MOTOR

5.1   Introduction

In chapter 4, different MGM designs with the stator on the inside of the high speed inner rotor were studied. These designs have the advantage of having a compact structure but, there is always a risk of a high temperature rise and demagnetization of the PMs, due to inadequate dissipation of heat generated by the inner stator. An alternate approach to drive the high speed inner rotor of the MG is to add the stator on the outside of the MG [9]. The PMs of the stationary outer rotor are mounted on the inner surface of the fixed outer stator. This outer stator MGM can be regarded as the combination of an MG and a large air gap PM machine wherein, the inner rotor is shared by both. The performance of an outer stator MGM with different rotor designs has been investigated by several authors. Huang *et al.* studied the performance of an MGM with Halbach consequent poles on the slot openings of the outer stator [101]. Penzkofer and Atallah modeled an MGM for large wind turbines with Halbach magnets on the outer rotor and surface mounted magnets on the inner rotor [102]. Glynn and Atallah integrated an MG with a brushless PM machine and investigated alternative winding configurations on the outer stator [103].And recently Zhang considered putting a stator on the outside of a flux focusing outer rotor MG design [104]. Many other MGM designs have also been investigated for different applications in wind power generation and flight control surface actuation [57, 58, 61-63]. In this chapter the design and comparison of two different outer stator MGMs with a rectangular and circular cage rotor steel design is investigated. Both rotors use Halbach magnet arrays on the high speed inner and stationary outer rotors. The MGMs were designed in three steps – the first step involved simulating the MG without

the stator. In the second step the stator was designed and simulated to interact only with the inner rotor as in a PM motor. In the final third step the MG and the PM motor were coupled magnetically to achieve the final MGM design. There is no load connected to the high speed inner rotor of the MGM. This produces a net zero torque on the high speed inner rotor. This net torque is the sum of the torque produced by the MG and that produced by the PM motor. To obtain a zero torque on the inner rotor of the MGM, an equal and opposite torque must be produced by the MG and by the PM motor when simulated separately.

5.2 Step 1: Magnetic Gear with Rectangular and Circular Steel Lamination Supports on the Cage Rotor

The first step in designing the outer stator MGM was to simulate the performance of the MGM without the stator. The MGs being utilized were designed by H.Y Wong [47] . The rectangular slot MG with a 5.66:1 gear ratio design is shown in Figure 5-1.The rectangular steel pieces on the cage rotor are connected by a 1 mm bridge. The Halbach rotor magnet arrays have been used on the inner high speed and the outer stationary rotor. The geometric parameters and material properties used for the design are mentioned in Table 5.1. The design was simulated to obtain the specific angular position of the cage rotor that produced peak torque on all the three rotors. This was achieved by rotating only the cage rotor to obtain the pole slipping torque. 2D FEA method has been used for the simulation. The pole slipping torques for the three rotors as a function of the low speed cage rotor angle is shown in Figure 5-2. It can be seen from Figure 5-2, that at the initial cage rotor position, a positive maximum torque was produced on the inner and the outer

rotor while a negative maximum torque was produced on the cage rotor. The calculated torque and the torque density values are shown in Table 5.2. The geometric parameters required to calculate the torque density, are defined in Figure 5-3. The torque densities are calculated using (2.65) ,(5.1) and (5.5).
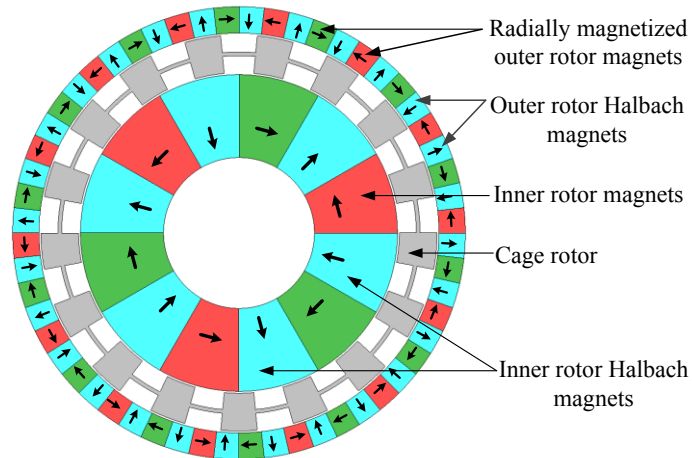
Figure 5-1: A 5.66:1 MG with rectangular steel laminations on the cage rotor [47]

TABLE 5.1
GEOMETRIC PARAMETERS AND MATERIAL PROPERTIES
OF 5.66:1 MG DESIGN

	Description	Value	Unit
Inner rotor (high speed)	Pole pairs, p_1	3	-
	Inner radius, r_{i1}	20	mm
	Outer radius, r_{o1}	42	mm
	Steel pole span, θ_{s1}	$\pi/(2p_1)$	radians
Cage rotor	Steel poles, n_2	17	-
	Cage bar thickness, l_2	10	mm
	Pole span, θ_{s2}	10.588	degrees
	Bridge inner radius, r'_{i2}	47	mm
	Bridge outer radius, r'_{o2}	48	mm
Outer rotor (stationary)	Pole pairs, p_3	14	-
	Inner radius, r_{i3}	53	mm
	Outer radius, r_{o3}	60	mm
	Steel pole span, θ_{s3}	$\pi/(2p_3)$	radians
Material	M19 steel resistivity	57	μΩ-cm
	M19 steel density, ρ_S	7402	kg/m³
	NdFeB magnet N40H, B_r	1.28	T
	NdFeB magnet density, ρ_m	7600	kg/m³
Air gap, g		0.5	mm
Active region stack length, d		75	mm
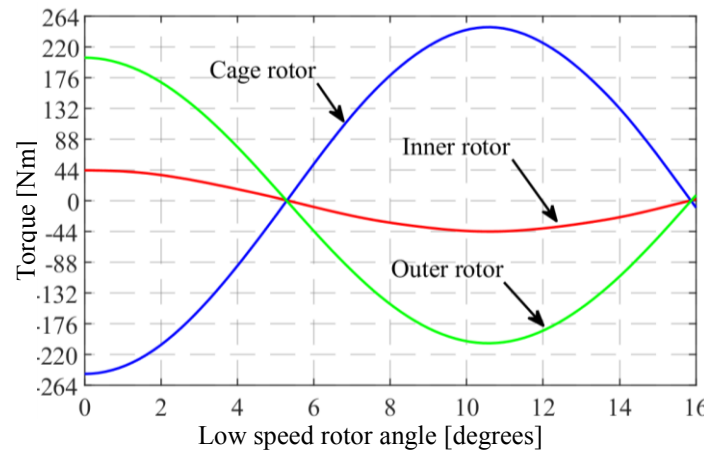
Figure 5-2: Pole slipping torque obtained by rotating the cage rotor with rectangular steel laminations
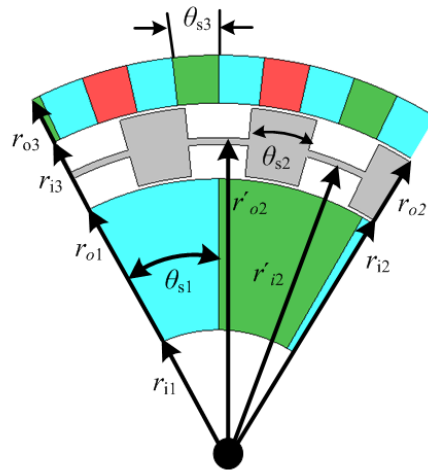
Figure 5-3: Geometric parameters of 5.66:1 MG with rectangular steel laminations on the cage rotor

The active region volumetric torque density of the MG can be computed by using (2.65)

The mass torque density T_m is defined as

$$T_m = \frac{T_2}{m_m + m_s}$$

(5.1)

where, m_s and m_m are the mass of the ferromagnetic steel and magnet mass respectively.

The magnet mass m_m is computed from

$$m_m = [(r_{o3}^2 - r_{i3}^2) + (r_{o1}^2 - r_{i1}^2)]\rho_m \pi d \tag{5.2}$$

The mass of the ferromagnetic steel pieces on the cage rotor is calculated from

$$m_s = \left[(r_{o2}^2 - r_{i2}^2) + \left(\left(r_{o2}' \right)^2 - \left(r_{i2}' \right)^2 \right) \right] \gamma_2 \rho_s \pi d \tag{5.3}$$

where, γ_2 is the percentage of modulator steel in the cage rotor calculated using

$$\gamma_2 = \frac{n_2 \theta_2}{360} \tag{5.4}$$

The torque per kilogram of magnet mass is computed using

$$T_{mm} = \frac{T_2}{\rho_m \left[\pi \left\{ (r_{o3}^2 - r_{i3}^2) + \left(r_{o1}^2 - r_{i1}^2 \right) \right\} \right] d} \tag{5.5}$$

TABLE 5.2
TORQUE AND TORQUE DENSITY VALUES OF MG DESIGN
WITH RECTANGULAR SLOT CAGE ROTOR

	Description	Value	Unit
	Inner rotor	44	Nm
Maximum torque	Cage rotor	248	Nm
	Outer rotor	204	Nm
Volume torque density		292	Nm/L
Mass torque density		50	Nm/kg
Torque per kg magnet mass		128	Nm/kg

The cage rotor of the MG design studied in the previous section is modified by replacing the rectangular slots with circular slots. The design is shown in Figure 5-4. This MG design was also investigated earlier by H.Y Wong. Other than the cage rotor, the same geometric parameters and the material properties mentioned in Table 5.1 have been used. The design, when simulated using 2D FEA, the pole slipping torque generated as a function of the low speed rotor angle is shown in Figure 5-5.
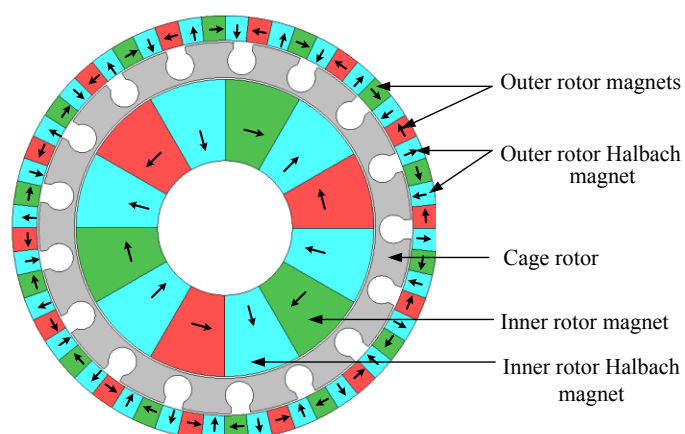
Figure 5-4: A 5.66:1 MG with circular steel laminations on the cage rotor [47]
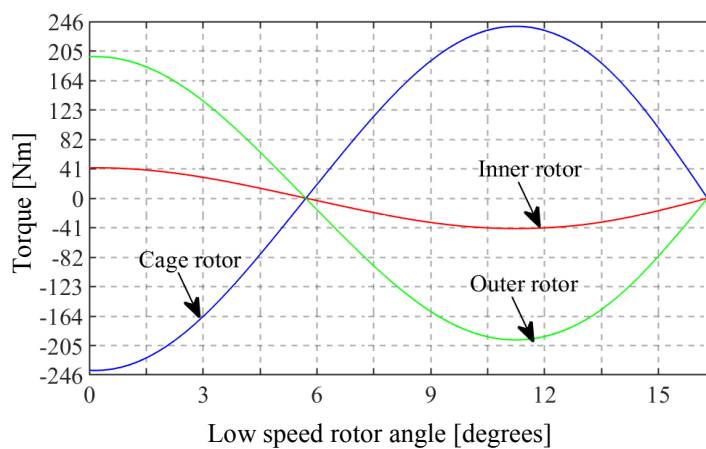
Figure 5-5: Pole slipping torque obtained by rotating the cage rotor with circular steel laminations

The mass of the cage rotor is calculated using (5.6). The torque and the torque density values calculated using (2.65), (5.1) and (5.5) are mentioned in Table 5.3.

$$m_s = \rho_m \alpha d \qquad (5.6)$$

where, α is the surface area of the modulator obtained from JMAG.

TABLE 5.3
TORQUE AND TORQUE DENSITY VALUES OF
MGM DESIGN WITH CIRCULAR SLOT CAGE ROTOR

	Description	Value	Unit
	Inner rotor	41	Nm
Maximum torque	Cage rotor	246	Nm
	Outer rotor	220	Nm
Volume torque density		290	Nm/L
Mass torque density		47	Nm/kg
Torque per kg magnet mass		127	Nm/kg

As both the circular and the rectangular cage rotor designs produced similar torque, only the analysis for the rectangular slot cage rotor design is described in detail when designing the stator.

5.3   Step 2: Designing the stator for the MGM

In step 2, the stator for the MGM is designed by eliminating the outer rotor and the cage rotor of the MG and adding a stator on the outside of the design and is shown in Figure 5-6. Thus a large air gap is created between the inner rotor and the stator. The magnetic field generated by the stator coil excitation, interacts with the field produced by the inner rotor and generates electromagnetic torque T_{em}. The parameters of the three phase excitation are adjusted such that T_{em} produced on the inner rotor is equal and opposite to that produced by the MG. The geometric parameters of the inner rotor of this design are the same as that specified in Table 5.1 and the stator parameters are specified in Table 5.4. The calculations required to design the stator winding for producing 6 poles, are discussed in the following section.
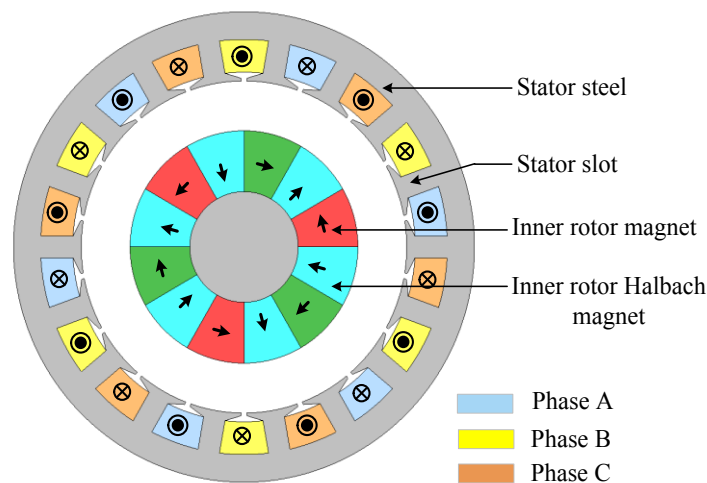
Figure 5-6: A large air gap PM motor

TABLE 5.4
GEOMETRIC PARAMETERS OF THE STATOR OF
THE PM MACHINE

	Description	Value	Unit
	No. of slots, n_s	18	-
	Inner radius, r_{i4}	60	mm
Stator	Outer radius, r_{o4}	85	mm
	Back iron thickness	10	mm

In this section, a three phase integral slot stator with n_s =18 slots and p_1= 6 poles

was designed.

The number of slots per pole per phase is

$$q = \frac{18}{3 \times 6} = 1 \tag{5.7}$$

The phase shift in electrical degrees between each slot can be calculated as

$$\theta_e = \frac{180 \times 6}{18} = 60^0 \text{ electrical.} \tag{5.8}$$

So, a coil coming out of slot 1 must enter slot 4 i.e.(coil span + 1).The distribution of the

three phases around the stator slots for one pole pair is shown in Figure 5-7. The same

sequence is repeated for the remaining 12 slots. The winding layout for the 18 slots is

shown in Figure 5-8.
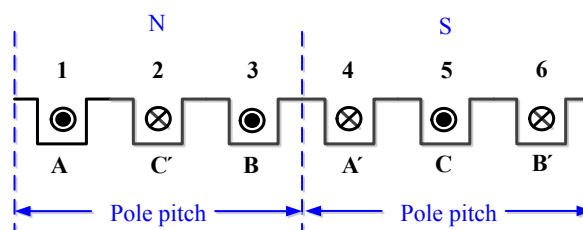
Figure 5-7: Coil connections in 6 slots for generating 1 pole pair
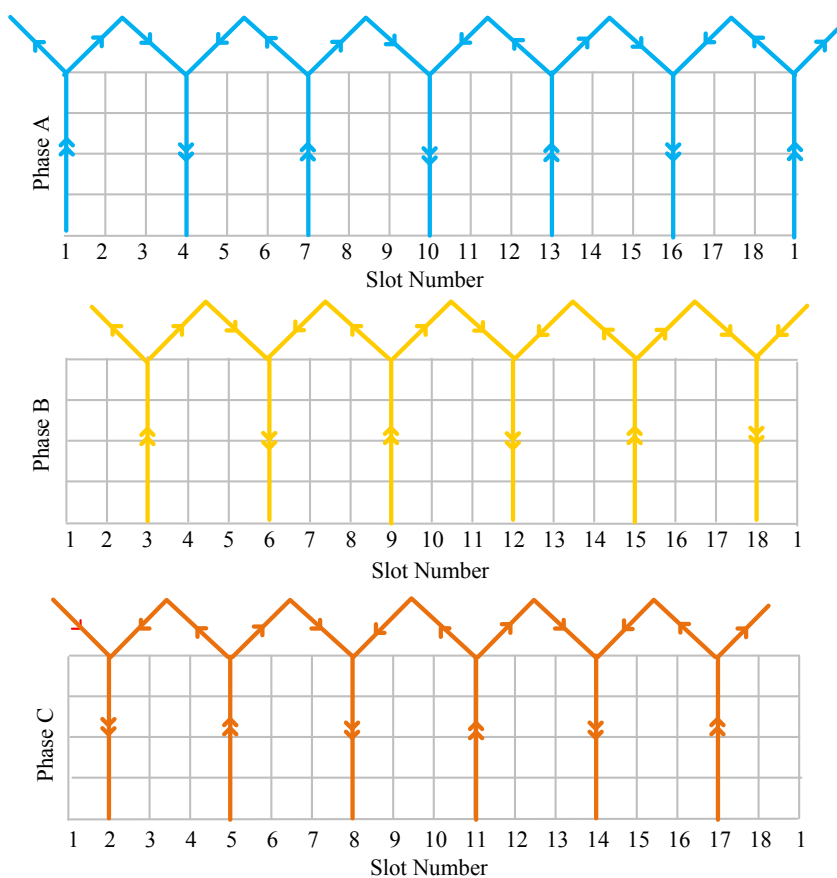
Figure 5-8: Winding layout of a 3 phase stator with 18 slots and generating 3 pole pairs

The turns function and the winding function are derived and are shown in Figure 5-9, Figure 5-10.The winding function is multiplied by the instant values of the phase currents at time $t = 0$ and are shown in Figure 5-11. The resultant wave obtained by summing up the MMF phase distribution is shown in Figure 5-12.
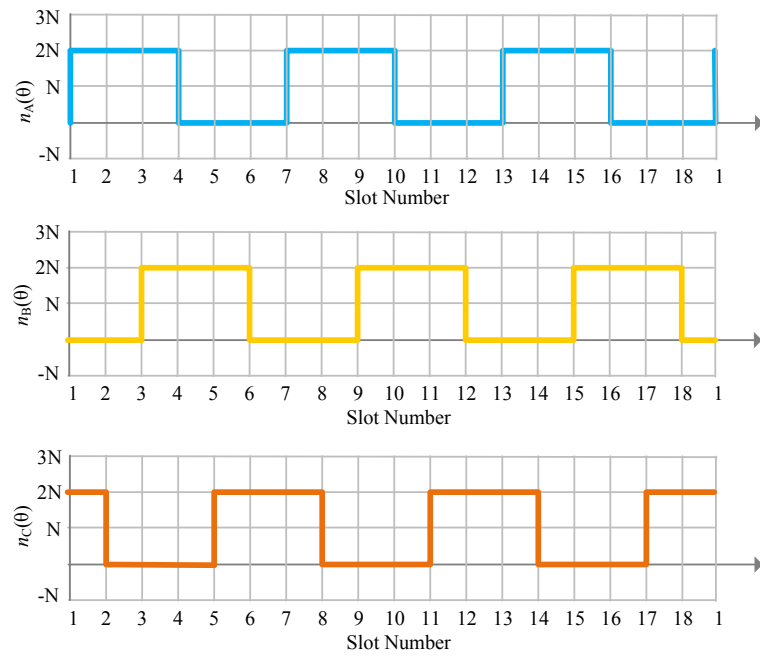
Figure 5-9: Turns function of a 3 phase stator with 18 slots generating 3 pole pairs
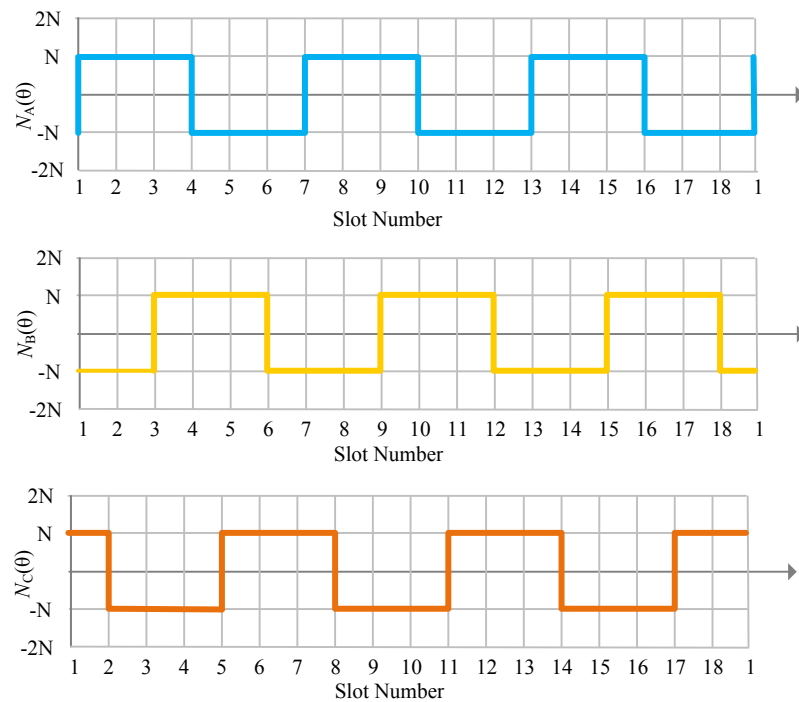
Figure 5-10: Winding function of a 3 phase stator with 18 slots generating 3 pole pairs
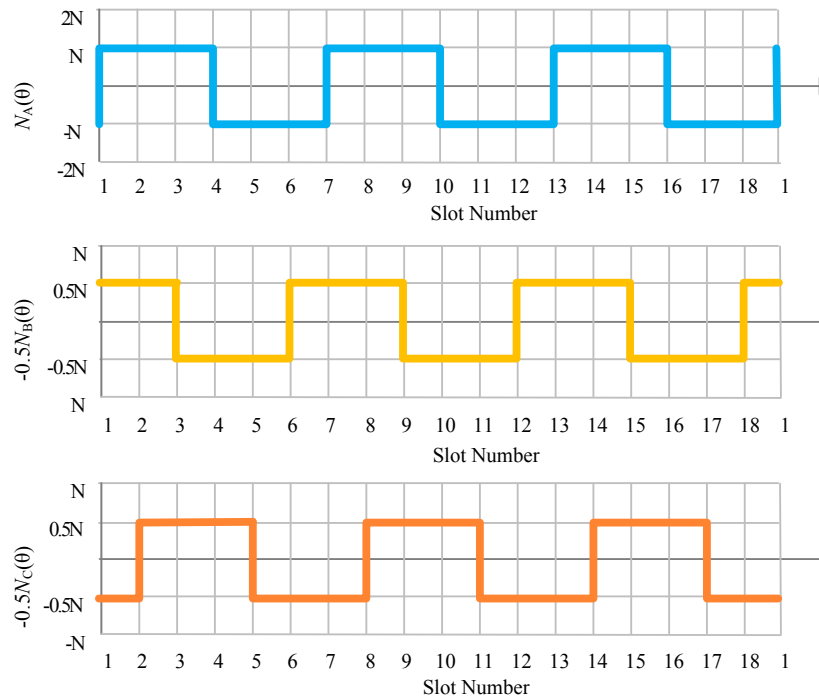
Figure 5-11: Winding function multiplied by the instantaneous value of current at $t = 0$
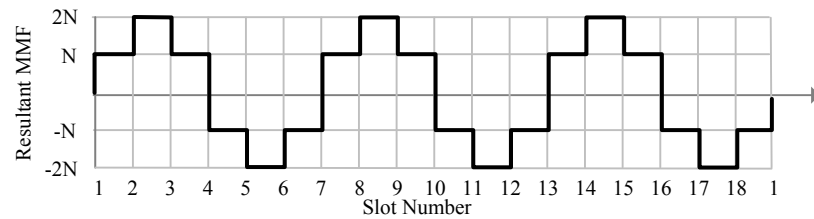
Figure 5-12: Resultant MMF wave produced by the stator windings when 3 phase excitation is added to the windings

A harmonic analysis using Fourier series was performed on the resultant MMF waveform obtained in Figure 5-12 [95]. Using Fourier series defined by (4.25) and evaluating using (4.28) , b_n can be written as,

$$b_n = \frac{2N}{n\pi}\left(1 - \cos n\pi + \cos\frac{n\pi}{3} - \cos\frac{2n\pi}{3}\right) \tag{5.9}$$

The values of Fourier coefficients, b_n and harmonic frequencies, nk_0 computed for each n are mentioned in Table 5.5. It is evident from the table that only the 3rd, 15th and 21st harmonics are dominant.

TABLE 5.5
FOURIER COEFFICIENTS AND
HARMONICS

n	b_n	nk_0
1	$6N/\pi$	3
2	0	6
3	0	9
4	0	12
5	$6N/5\pi$	15
6	0	18
7	$6N/7\pi$	21
8	0	24
9	0	27

The Fourier series using (5.9) can be written as

$$MMF(\theta) = \frac{2p_1 N}{\pi}\left[\sin(p_1\theta) + \sum_{n=3}^{\infty}\frac{\sin\left[(2n-1)p_1\theta\right]}{2n-1}\right] \tag{5.10}$$

Using (5.10), the resultant MMF waveform has been regenerated in Matlab and is shown in Figure 5-13. The resultant MMF confirms that the coil connections used would produce 3 pole pairs when excitation is added to it. This ensures that the winding design used is accurate.
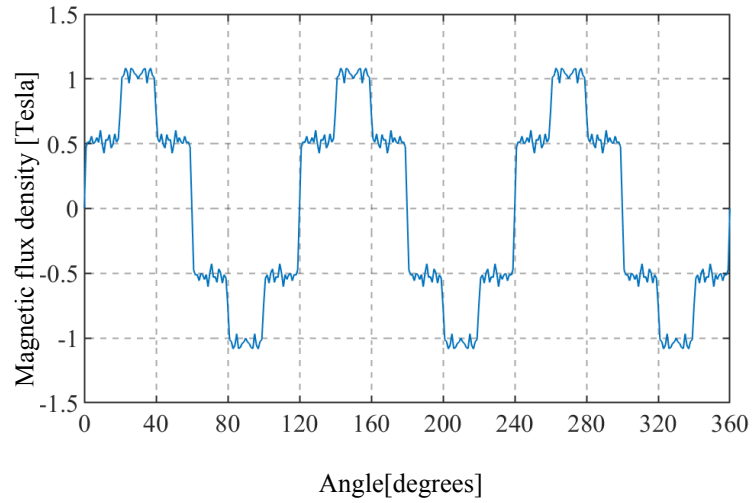
Figure 5-13: Resultant MMF waveform regenerated in Matlab
using 57 harmonics

The geometric parameters and the material properties required to calculate the circuit parameters for simulation are defined in Figure 5-14. and mentioned in Table 5.6.
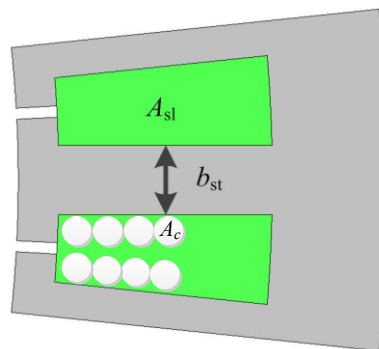
Figure 5-14: Stator parameters
definition

TABLE 5.6
PARAMETERS FOR THE CALCULATION OF STATOR COIL RESISTANCE
AND NUMBER OF TURNS

Parameters	Description	Value	Unit
A_{sl}	Slot cross sectional area	190	mm^2
Φ_d	Coil diameter	1	mm
A_c	Coil cross sectional area	0.785	mm^2
ξ_p	Packing factor	0.5	-
d	Stack length	75	mm
ρ	Copper resistivity	1.68x10^{-5}	Ω-mm
r	Center radius of the slot	70	mm
τ	Coil pitch	3	-

Using the value of the packing factor ξ_p and the slot cross sectional area A_{sl} in (4.14) the slot surface area used by the conductors is

$$A_s = 95 \text{ mm}^2 \tag{5.11}$$

And evaluating (4.16), the number of turns, N of each phase coil is

$$N = 121 \tag{5.12}$$

The resistance of each coil is calculated using (4.18). In order to calculate the resistance, the geometric parameters required to calculate the coil length need to be evaluated considering Figure 5-15.
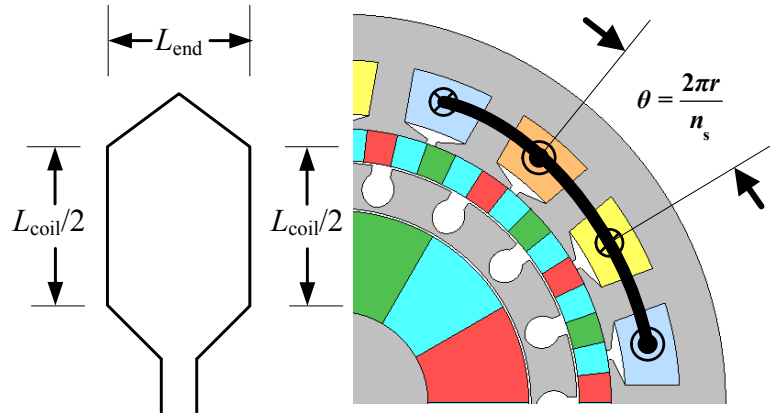
Figure 5-15: Geometric parameters definition for coil length calculation

The coil length L is calculated as

$$L = L_{end} + L_{coil} \tag{5.13}$$

$$L_{end} = \frac{2\pi r}{n_s} \times \tau \times 2 \tag{5.14}$$

$$L_{coil} = d \times 2 \tag{5.15}$$

$$L = 297 \text{ mm} \tag{5.16}$$

Using (4.18) , the resistance of each coil obtained is

$$R = 0.00635 \ \Omega \tag{5.17}$$

With the winding and the circuit designed, the PM motor is simulated using 2D FEA. The pole slipping torque produced by the motor as a function of time is plotted in Figure 5-16. It can be verified by comparing Figure 5-2 with Figure 5-16 that the torque produced on the inner rotor of the PM motor during pole slipping is equal and opposite to that produced on the inner rotor of the MG.
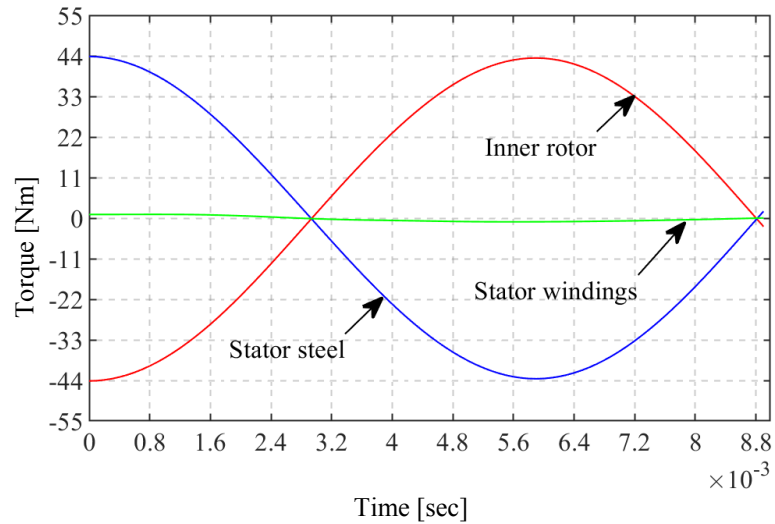
Figure 5-16:Torque produced by the PM motor with a current density of 16 A/mm^2

To obtain the required torque, the current and the initial phase angle were adjusted. The maximum current required was I_{max} = 25A. This corresponds to a peak current density of

$$I_{density} = \frac{N \times I_{max}}{A_{sl}} \qquad (5.18)$$

$$I_{density} = 16A/mm^2 \qquad (5.19)$$

5.4 Step 3: Magnetically Geared Motor with Rectangular Modulator Lamination Supports

In this section, the cage rotor and the outer rotor were added back in between the stator and the inner rotor. The fully designed MGM is shown in Figure 5-17. The inner rotor and the cage rotor are rotated at speeds conforming to the gear ratio of the MG to generate steady state torques on the rotors and the stator. Figure 5-18 shows the generated torque as a function of time at the peak torque condition. To attain zero torque on the inner rotor, the maximum current value was further adjusted to 21A. This corresponds to a current density of 13 A/mm^2.
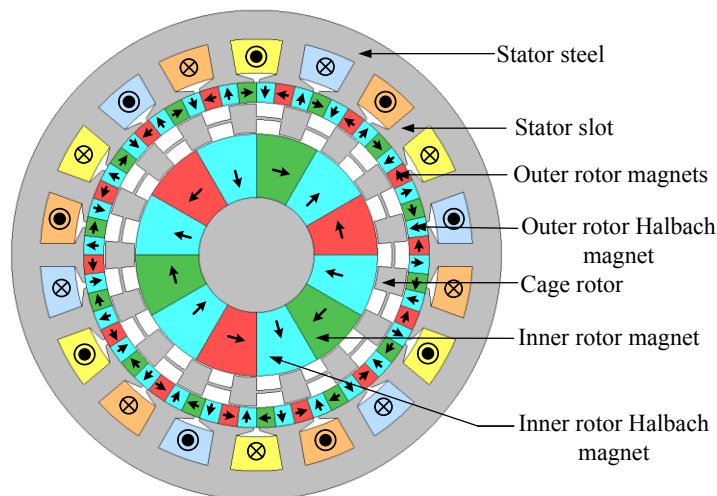
Figure 5-17: MGM with rectangular slot cage rotor design

:
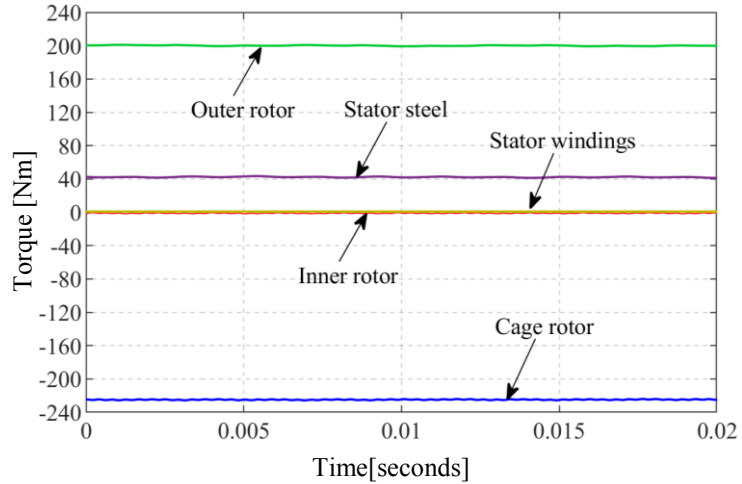
Figure 5-18: Steady peak torque generated using a current density
13 A/mm² in an MGM with rectangular slot cage rotor design

The torque density values have been calculated with the stator taken into consideration.

The volume torque density T_d has been calculated using

$$T_v = \frac{T_2}{\pi r_{o4}^2 d}$$ (5.20)

where, d is the axial length of the MG, T_2 is the torque obtained on the cage rotor and r_{o4}

is the outer radius of the stator.

The mass torque density T_m is computed by equation (5.1) where, the magnet mass m_m is

as obtained from equation (5.2). However, the steel mass, m_s should also include the mass

of the stator steel. The modified m_s is calculated using

$$m_s = \left[\gamma_2 \pi \left((r_{o2}^2 - r_{i2}^2) + \left((r_{o2}')^2 - (r_{i2}')^2 \right) \right) + \alpha_s \right] \rho_s d$$ (5.21)

where, α_s is the stator steel surface area obtained from JMAG.

The torque per kilogram of magnet mass is computed by using (5.5). The torque and the torque density values are mentioned in Table 5.7. A torque ripple analysis has been conducted to ensure that the MGM design is viable unlike the inner stator MGM designs studied in chapter 3. Figure 5-19 shows the torque ripple produced on the high speed inner rotor and the low speed cage rotor.

TABLE 5.7
TORQUE AND TORQUE DENSITY VALUES OF THE
RECTANGULAR SLOT MGM DESIGN

	Description	Value	Unit
Average torque	Inner rotor	-0.3	Nm
	Cage rotor	-227	Nm
	Outer rotor	199	Nm
	Stator steel	39	Nm
	Stator windings	1.7	Nm
Volume torque density		132	Nm/L
Mass torque density		24	Nm/kg
Torque per kg magnet mass		117	Nm/kg
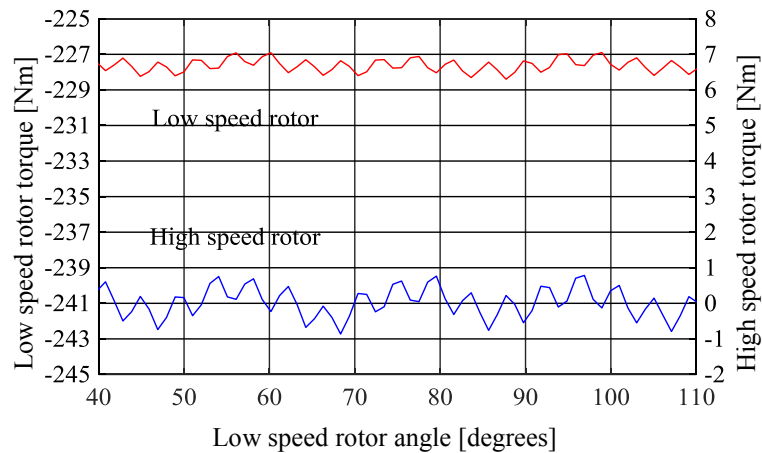
Figure 5-19: Torque ripple generated by the MGM with rectangular slot cage rotor design

It shows that a torque ripple of 1 Nm (100%) is produced on the inner rotor, a torque ripple of 3 Nm (1.3%) is produced on the cage rotor. The torque ripple produced on both the rotors is quite low compared to the inner stator MGM design. This designed MGM cannot operate at its peak designed torque value continuously due to the high current density.The stator geometry was modified to operate the MGM at a maximum current density of 5A/mm^2. The outer radius of the stator was increased to 105 mm. The thickness of the stator teeth, b_{st} was increased from 8 mm to 10 mm to prevent saturation. The slot surface area increased to 559 mm. The design is shown in Figure 5-20. The steady state torque generated using 2D FEA is shown in Figure 5-21.
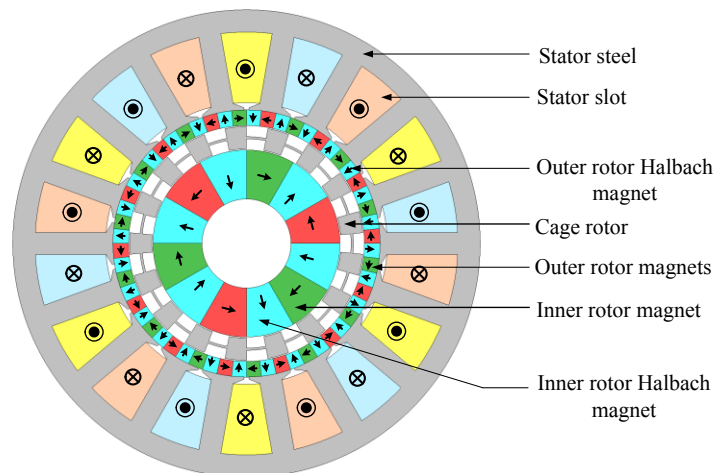
Figure 5-20: MGM with rectangular slot cage rotor designed to operate with a current density of 4.5A/mm^2
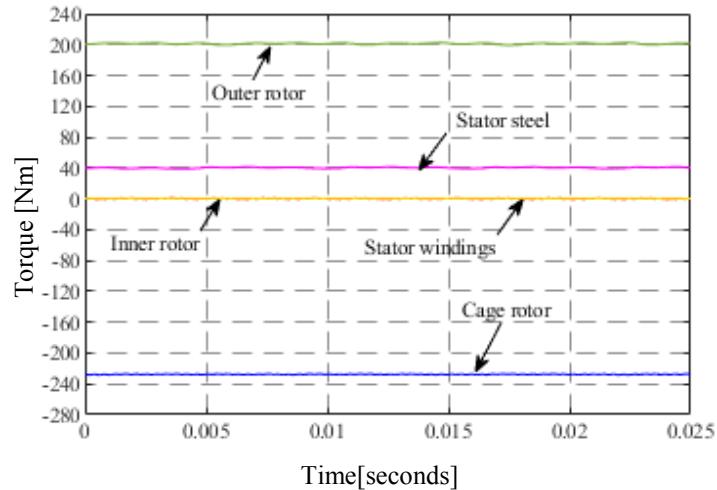
Figure 5-21: Steady peak torque generated using a current density 4.5 A/mm^2 in an MGM with rectangular slot cage rotor design

The torque and the torque density values are mentioned in Table 5.8. It is evident from Table 5.7 and Table 5.8 that the volume torque density decreased by 33% while the mass torque density decreased by 17%. The radial component of the flux density, B_r plotted in Figure 5-22 shows that the stator steel is unsaturated. The torque ripple produced on the cage rotor and the inner rotor is shown in Figure 5-23. A torque ripple of 1 Nm (0.4%) is produced on the low speed cage rotor and a torque ripple of 1.5 Nm is produced on the high speed inner rotor.

TABLE 5.8
TORQUE AND TORQUE DENSITY VALUES OF THE RECTANGULAR
SLOT MGM DESIGN WITH REDUCED CURRENT DENSITY

	Description	Value	Unit
Average torque	Inner rotor	0.3	Nm
	Cage rotor	-227	Nm
	Outer rotor	201	Nm
	Stator steel	40	Nm
	Stator windings	0.5	Nm
Volume torque density		88	Nm/L
Mass torque density		20	Nm/kg
Torque per kg magnet mass		118	Nm/kg
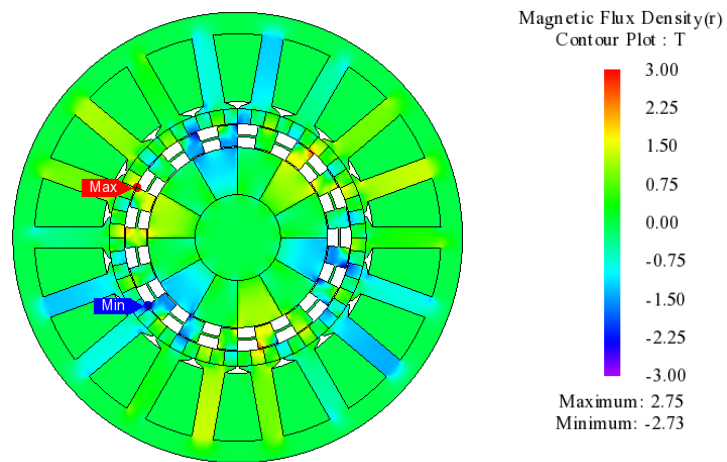
Figure 5-22: Radial component of the magnetic flux density, B_r obtained with a current density of 4.5 A/mm^2
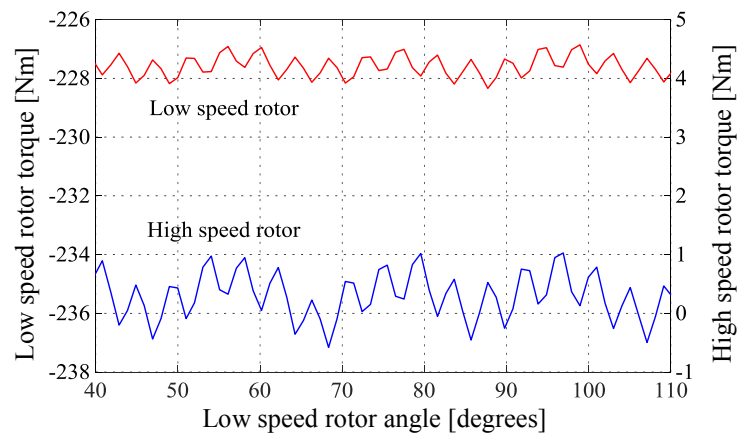
Figure 5-23: Torque ripple generated by the MGM with rectangular slot cage rotor design operating at a current density of 4.5 A/mm^2

5.5   Magnetically Geared Motor with Circular Modulator Lamination Supports

The MGM with circular modulator on cage rotor is shown in Figure 5-24. A three phase current excitation with a maximum value of 25 A is applied to the stator. The steady state torques generated as a function of time is shown in Figure 5-25. In order to get a zero torque on the inner rotor, the maximum current per phase were adjusted to a value of 20 A. This gives a current density of 14 A/mm^2.
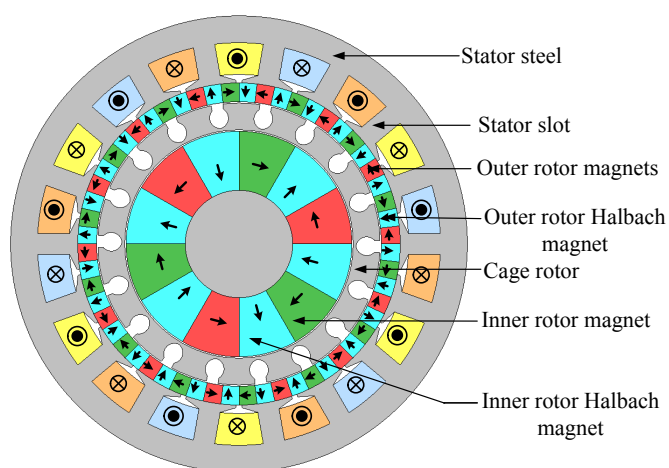
Figure 5-24:MGM with circular slot cage rotor designed to operate with a current density of 14 A/mm^2
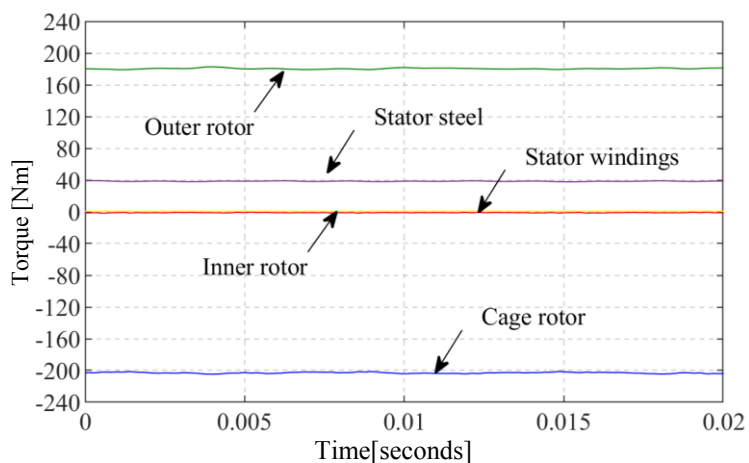

Figure 5-25: Steady peak torque generated using a current density 14 A/mm^2 in an MGM with circular slot cage rotor design

The torque and the torque density values of the MGM are mentioned in Table 5.9. The volume torque density and the torque per kg magnet mass are obtained from (5.20), (5.5). The mass torque density is obtained using (5.1) where the magnet mass m_m is the same as before. The mass of the steel m_s is modified to

$$m_s = \rho_s d \left(\alpha + \alpha_s \right) \tag{5.22}$$

TABLE 5.9
TORQUE AND TORQUE DENSITY VALUES OF THE CIRCULAR
SLOT MGM DESIGN

	Description	Value	Unit
	Inner rotor	-0.1	Nm
	Cage rotor	-203	Nm
Average torque	Outer rotor	175	Nm
	Stator steel	34	Nm
	Stator windings	1.5	Nm
Volume torque density		119	Nm/L
Mass torque density		13	Nm/kg
Torque per kg magnet mass		105	Nm/kg

Figure 5-26 shows the torque ripple present on the high speed inner rotor and the low speed cage rotor of the MGM. This is 2.5 Nm (1.1%) for the cage rotor and 1 Nm (200%) for the inner rotor.
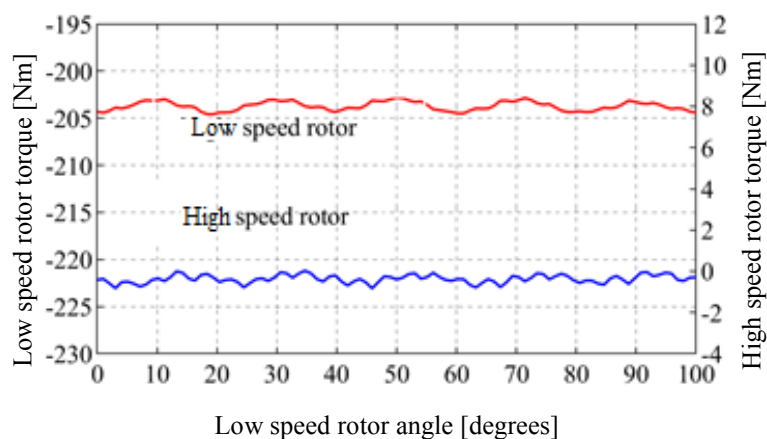
Figure 5-26: Torque ripple generated by the MGM with circular slot cage rotor design at a current density of 14 A/mm^2

The outer stator of the circular slot MGM design when modified to operate at a lower current density is shown in Figure 5-27. The steady state torque generated by the MGM is shown in Figure 5-30. The current density required to produce a zero torque on the inner rotor is 5A/mm^2. The torque and the torque density values are mentioned in Table 5.10 and the contour plot of the radial flux density is shown in Figure 5-29.
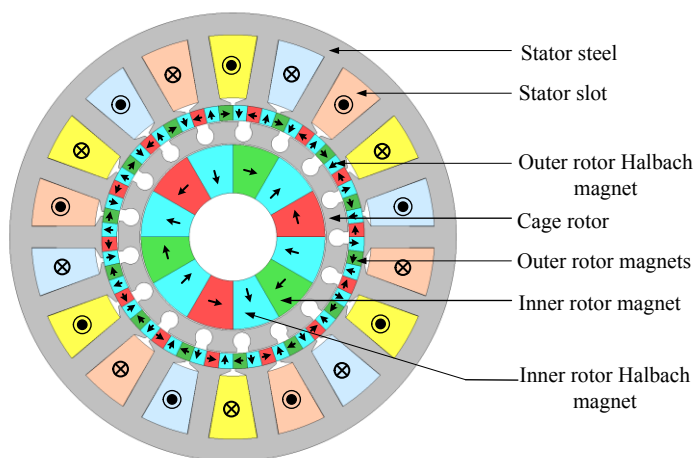
Figure 5-27: MGM with circular slot cage rotor designed to operate with a current density of 5A/mm^2
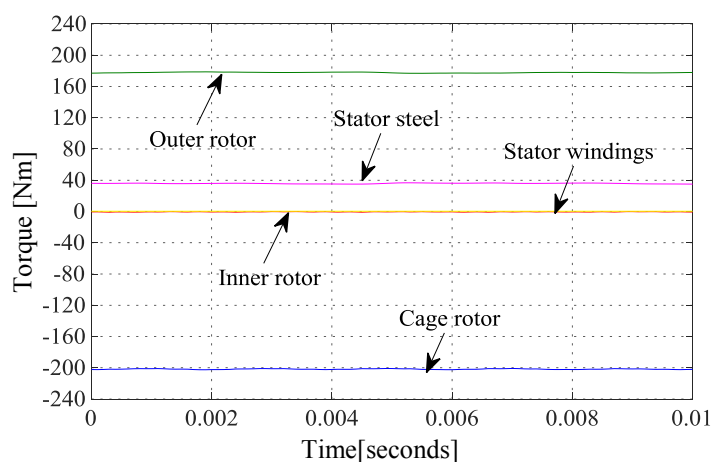
Figure 5-28: Steady state torque generated by the MGM with a current density of 5A/mm^2

TABLE 5.10
TORQUE AND TORQUE DENSITY VALUES OF THE CIRCULAR SLOT MGM DESIGN WITH REDUCED CURRENT DENSITY

	Description	Value	Unit
Average torque	Inner rotor	-0.5	Nm
	Cage rotor	-202	Nm
	Outer rotor	177	Nm
	Stator steel	36	Nm
	Stator windings	0.3	Nm
Volume torque density		78	Nm/L
Mass torque density		11	Nm/kg
Torque per kg magnet mass		105	Nm/kg
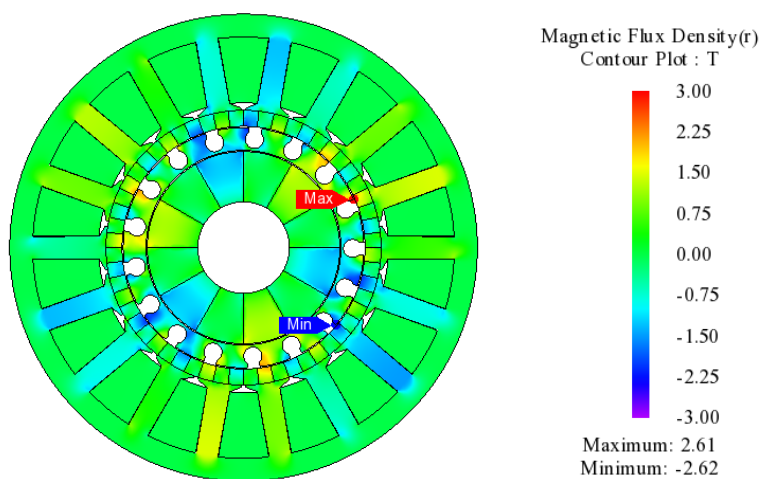
Figure 5-29: Radial component of the magnetic flux density, B_r obtained with a current density of 5 A/mm^2

The torque ripple present on the high speed inner rotor and the low speed cage rotor of the MGM is shown in Figure 5-30. This is 2 Nm (1%) for the cage rotor and 0.5 Nm (100%) for the inner rotor. The torque densities for all the four designs are summarized in Table 5.11.
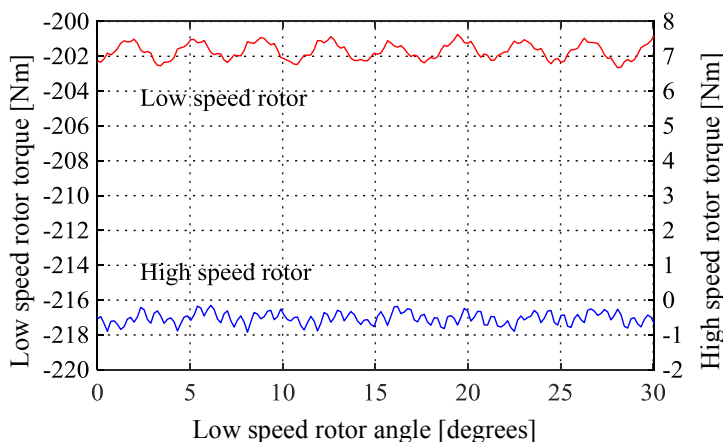
Figure 5-30: Torque ripple generated by the MGM with original cage rotor design

TABLE 5.11
TORQUE AND TORQUE DENSITY VALUES OF RECTANGULAR SLOT AND CIRCULAR SLOT MGM DESIGN WITH ORIGINAL AND REDUCED CURRENT DENSITIES

	Rectangular slot design		Circular slot design		
	16 A/mm^2	4.5 A/mm^2	14 A/mm^2	5A/mm^2	Unit
Inner rotor	-0.3	0.3	-0.1	-0.5	Nm
Cage rotor	-227	-227	-203	-202	Nm
Outer rotor	199	201	175	177	Nm
Stator steel	39	40	34	36	Nm
Stator windings	1.7	0.5	1.5	0.3	Nm
Volume torque density	132	88	119	78	Nm/L
Mass torque density	24	20	13	11	Nm/kg
Torque per kg magnet mass	117	118	105	105	Nm/kg

5.6   Conclusion

An MGM with a gear ratio of 5.66:1 has been studied. The torque and the torque densities obtained for the rectangular slot cage rotor design is higher than the circular slot cage rotor design by 10%. The torque ripple produced by the two designs does not show a significant difference. The torque density would further decrease when the designs are simulated using 3D FEA. Thus the rectangular slot cage rotor design will be further considered for proof of principle prototyping.

6 CONCLUSIONS AND FUTURE WORK

6.1 Introduction

The aim of this research was to design a high torque density MG by studying different typologies and integrating the MG design with an electrical machine to achieve high torque density MGM and with low torque ripple. The main conclusion of the research has been summarized in section 6.2 while the research contributions are discussed in section 6.3. The scope of future work is mentioned in section 6.4.

6.2 Conclusions

MGs with different typologies and gear ratios have been studied and simulated. The designs with flux focusing magnets on both the inner and outer rotor produced the maximum torque. When the gear ratio of this typology is increased from 4.25:1 to 8.5:1, higher speed is obtained at the output rotor with an 11% reduction in torque. The cage rotor when designed as the outermost rotor reduced the torque by 61%. Hence converting the cage rotor to an outer stator for designing MGMs is not a feasible idea. When the outer rotor of the 8.5:1 idealized flux focusing design was replaced by a rotor with consequent poles, the torque was reduced by 34%. Thus the idealized design with flux focusing magnets on both the inner and outer rotor and a gear ratio of 8.5:1 was considered the most suitable typology for designing MGMs.

A flux concentration Halbach rotor MG was designed, simulated and experimentally validated. The simulated design produced a higher torque density compared to the prototype built. The use of ferromagnetic flux concentration poles within the Halbach type structure made the assembly process more complicated which is considered as a reason for the reduction in the torque density. Thus the flux concentration

design is considered to be best implemented when less number of poles are used to design the MG.

MGMs have high torque densities compared to PM motors. It is evident from Table 1.4 that the torque per kg magnet mass is higher in case of PM motor when compared to the MGMs. However, the torque per kg steel and the torque per kg copper is higher in MGMs compared to PM motors. This makes the MGMs more cost effective than the PM machines.

In this dissertation, MGM obtained by coupling PM machine with a flux modulated MG with a gear ratio of 8.5:1 were simulated and studied at first with internal stator design. Due to the internal stator design, the outer radius of the MGM is same as the MG design. Both integral slot winding design and fractional slot winding design were studied. These winding designs produced a high torque ripple. To mitigate this, a two layered stator slot with one slot chording was used. This reduced the torque ripple by 80%. The internal stator design however requires three air gaps which make the design complex to construct. The inner stator MGM design would have thermal limitations as heat dissipation would be an issue. To avoid overheating, outer stator design was studied. Integral slot winding design was used to design the outer stator to produce a zero torque on the inner rotor at no load condition. The design was simulated with both rectangular and circular modulator steel designs. The stator of the design is oversized to make the current density low which in turn reduced the torque density. However, the torque ripple obtained was quite low.

6.3   Research Contributions

The research contributions are summarized as

- Different MG design typologies using 2D FEA analysis have been studied and compared. The parametric sweep analysis was conducted in 2D FEA to finalize the design parameters. The MG design with a high torque density was chosen for designing MGM.

- An inner stator has been designed to build an MGM with both integral slot and fractional slot windings. The winding design considerations to reduce the torque ripple have been studied and implemented to mitigate the high torque ripple generated in the inner stator MGM.

- A flux concentration MG with Halbach magnets have been studied and designed to replace the retaining sleeves used for holding the Halbach magnets. The design was studied using both 2D and 3D FEA. The design has been built and experimentally tested.

- An outer stator MGM with integral slot winding has been designed to operate at a low current density, using 2D FEA analysis. The MGM was designed to produce a zero torque The design produced a low torque ripple

6.4   Future Work

The future work would include

- Simulating the outer stator integral slot MGM design in 3D using FEA.

- Conducting the loss study and modifying the design to reduce the losses

- Building the prototype and experimentally validating it.

BIBLIOGRAPHY

[1]   R. Wiser and B. M., "2013 Wind Technologies Market Report," U.S.Department of Energy2014.

[2]   Available: http://ipg-co.com/images/blog/1/windTurbineLabels.png

[3]   F. Rasmussen and *e. al.*, "The Gearbox Problem Revisited," in *Riso fact Sheet AEDRB-17(EN)*, ed. Roskilde, DK, : Riso National Laboratory, 2004.

[4]   W. Musial and *e. al.*, "Improving Wind Turbine Gearbox Reliability," 2007.

[5]   J. Puigcorbe and A. Beaumont, "Wind Turbine GearboxReliability : The impact of rotor support. RenewableEnergyWorld," 2010.

[6]   C. Bratiloveanu and I. Boldea, "A comparative investigation of three PM-less MW power range wind generator topologies," presented at the Optimization of Electrical and Electronic Equipment (OPTIM), 2012 13th International Conference 2012.

[7]   Renewable Technologies. (2012). *Direct Drive Generator by Goldwind*. Available: https://yes2renewables.org/2012/03/06/rare-earth-magnets-not-all-new-turbines-are-using-them/

[8]   S. Mezani, T. Hamiti, L. Belguerras, T. Lubin, M. Rashed, and C. Gerada, "Magnetically Geared Induction Machines," presented at the IEEE Transactions on Magnetics, 2015.

[9]   K. Atallah, J. Rens, S. Mezani, and D. Howe, "A Novel Pseudo Direct-Drive Brushless Permanent Magnet Machine," presented at the IEEE Transactions on Magnetics, 2008.

[10]   P. O. Rasmussen, T. V. Frandsen, K. K. Jensen, and K. Jessen, "Experimental Evaluation of a Motor-Integrated Permanent-Magnet Gear," presented at the IEEE Transactions on Industry Applications, 2013.

[11]   P. O. Rasmussen, H. H. Mortensen, T. N. Matzen, T. M. Jahns, and H. A. Toliyat, "Motor integrated permanent magnet gear with a wide torque-speed range," in *ECCE*, 2009, pp. 1510–1518.

[12]   L. L. Wang, J. X. Shen, P. C. K. Luk, W. Z. Fei, C. F. Wang, and H. Hao, "Development of a Magnetic-Geared Permanent-Magnet Brushless Motor," presented at the IEEE Transactions on Magnetics, 2009.

[13]   L. Jian, K. T. Chau, and J. Z. Jiang, "A Magnetic-Geared Outer-Rotor Permanent-Magnet Brushless Machine for Wind Power Generation," presented at the IEEE Transactions on Industry Applications, 2009.

[14]   D. Jones, "A new buried magnet brushless PM motor for a traction application," in *Elec. Insu. conf. and Elect. Man. and Coil Wind. Tech. Conf.*, 2003, pp. 421-429.

[15]   N. W. Frank and H. A. Toliyat, "Gearing ratios of a magnetic gear for marine applications," presented at the IEEE Electric Ship Technologies Symposium, Baltimore, MD, USA, 2009.

[16]   S. Gerber and W. Rong-Jie, "Design and Evaluation of a Magnetically Geared PM Machine," presented at the IEEE Transactions on Magnetics, 2015.

[17]   K. Hwang and *e. al.*, "A Study on Optimal Pole Design of Spoke-Type IPMSM With Concentrated Winding for Reducing the Torque Ripple by Experiment Design Method," presented at the IEEE Trans. on Magnetics, 2009.

[18]   H. Polinder, A. Abrahamsen, and K. Atallah, "Trends in Wind Turbine Generator Systems," *IEEE JOURNAL OF EMERGING AND SELECTED TOPICSIN POWER ELECTRONICS,* vol. 1, 2013.

[19]   E. Morimoto, K. Hirata, N. Niguchi, and Y. Ohno, "Design and Analysis of Magnetic-Geared Motor with Field Windings," 2014.

[20]   P. S. Wiak, N. Niguchi, and K. Hirata, "Magnetic-geared motors with high transmission torque density," *COMPEL - The international journal for computation and mathematics in electrical and electronic engineering,* vol. 34, pp. 428-438, 2015.

[21]   C. J. Ifedi, B. C. Mecrow, J. D. Widmer, G. J. Atkinson, S. T. M. Brockway, and D. Kostic-Perovic, "A high torque density, direct drive in-wheel motor for electric vehicles," presented at the 6th IET International Conference on Power Electronics, Machines and Drives (PEMD 2012), Bristol, UK, 2012.

[22]   T. Burress, S. Campbell, C. Coomer, C. Ayers, A. Wereszczak, J. Cunningham, L. Marlino, L. Seiber, and H. Lin. (2011, Evaluation of the 2010 Toyota Prius Hybrid Synergy Drive System.

[23]   Frandsen and T. Vestergaard, "Motor Integrated Permanent Magnet Gear," Doctor of Philosophy, Aalborg University, 2016.

[24]   K. T. Chau, D. Zhang, J. Z. Jiang, C. Liu, and Y. Zhang, "Design of a magnetic-geared outer-rotor permanent-magnet brushless motor for electric vehicles," presented at the IEEE Trans. Magn, 2007.

[25]   S. Gerber and R. J. Wang, "Design of a Magnetically Geared PM Machine," presented at the 4th International Conference on Power Engineering, Energy and Electrical Drives, Istanbul, Turkey, 2013.

[26]   L. Jian and K. T. Chau, "Design and Analysis of a Magnetic-Geared Electronic-Continuously Variable Transmission System Using Finite Element Method," presented at the Progr. Electrmagn. Res, 2010.

[27]   J. Wang, K. Atallah, and S. D. Carvley, "A Magnetic Continuously Variable Transmission Device," presented at the IEEE Trans. Mag, 2011.

[28]   K. Atallah, J. Wang, S. D. Calverley, and S. Duggan, "Design and Operation of a Magnetic Continuously Variable Transmission," presented at the IEEE Trans. Ind. Appl, 2012.

[29]   X. Zhu, L. Chen, L. Quan, Y. Sun, W. Hua, and Z. Wang, "A new magnetic-planetary-geared permanent magnet brushless machine for hybrid electric vehicle," presented at the IEEE Trans. Magn, 2012.

[30]   P. Pamanathan, "Design of a Continuously Variable Magnetic Gear," Master of Science, Electrical Engineering, The University of North Carolina at Charlotte, 2013.

[31]   W. N. Fu and S. L. Ho, "A Quantitative Comparative Analysis of a Novel Flux-Modulated Permanent-Magnet Motor for Low-Speed Drive," presented at the IEEE Transactions on Magnetics, 2010.

[32]   C. H. Lee, "Vernier Motor and Its Design," pp. 343 - 349, June 1963 1963.

[33]   S. Gerber and R. J. Wang, "Torque capability comparison of two magnetically geared PM machine topologies," presented at the 2013 IEEE International Conference 2013.

[34]   K. K. Uppalapati, "An Investigation into the Torque Density Capabilities of Flux-Focusing Magnetic Gearboxes," Ph.D., Electrical Engineering, The University of North Carolina at Charlotte, 2015.

[35]   T. B. Martin, "Magnetic Transmission," USA Patent, 1968.

[36]   L. Yong, X. Jingwei, P. Kerong, and L. Yongping, "Principle and simulation analysis of a novel structure magnetic gear," presented at the Electrical Machines and Systems, 2008. ICEMS 2008. International Conference, Wuhan, China, 2009.

[37]   M. Popescu, "Prediction of the electromagnetic torque in synchronous machines through Maxwell stress harmonic filter (HFT) method," presented at the Electrical Engineering, 2006.

[38]   W. Zhu, S. Pekarek, and B. Fahimi, "Investigation of Force Generation in a Permanent Magnet Synchronous Machine," *IEEE Transactions on Energy Conversion,* vol. 22, pp. 557 - 565, 2007.

[39]   D. J. Griffiths, *Introduction to Electrodynamics*: Prentice Hall, 1999.

[40]   J. D. Jackson, *Classical Electrodynamics*, 1999.

[41]   C. M. Spargo, B. C. Mecrow, and J. D. Widmer, "A Seminumerical Finite Element Postprocessing Torque Ripple Analysis Technique for Synchronous Electric Machines Utilizing the Air-Gap Maxwell Stress Tensor," presented at the Magnetics IEEE Transactions, 2014.

[42]   H. H. Woodson and J. R. Melcher, *Electromechanical Dynamics Part II: Fields Forces and Motion*: John Wiley & Sons, 1968.

[43]   K. J. Messen, J. J. H. Paulides, and E. A. Lomonova, "Force Calculations in 3-D Cylindrical Structures Using Fourier Analysis and the Maxwell Stress Tensor," presented at the IEEE Trans. Mag, 2013.

[44]   K. Atallah, S. D. Calverley, and D. Howe, "Design, analysis and realisation of a high-performance magnetic gear," in *IEE Proc.-Electr. Power Appl*, 2004, pp. 135-143.

[45]   K. Atallah and D. Howe, "A novel high-performance magnetic gear," presented at the IEEE Transactions on Magnetics, 2001.

[46]   J.-X. Shen, H.-Y. Li, H. Hao, and M.-J. Jin, "A coaxial magnetic gear with consequent-pole rotors," presented at the IEEE Trans. Energy Convers, 2017.

[47]   H. Y. Wong, J. Z. Bird, D. Barnett, and W. Williams, "A High Torque Density Halbach Rotor Coaxial Magnetic Gear," presented at the IEEE International Electric Machines & Drives Conference (IEMDC), San Diego, CA, USA, 2019.

[48]   K. T. Chau, Z. Dong, J. Z. Jiang, L. Chunhua, and Z. Yuejin, "Design of a magnetic-geared outer-rotor permanent-magnet brushless motor for electric vehicles," presented at the IEEE Trans. Magn, 2007.

[49]   D. Z. Abdelhamid and A. M. Knight, "Performance of a high torque density induction motor with an integrated magnetic gear," presented at the Electr.Mach. (ICEM2016), Int. Conf., 2016.

[50]   M. Aoyama, Y. Kubota, and T. Noguchi, "Proposal of self-excited wound-field magnetic geared motor for HEV application," presented at the Energy Convers. Congr. Expo. (ECCE 2015), 2015.

[51]   T. V. Frandsen, P. O. Rasmussen, and K. K. Jensen, "Improved motor integrated permanent magnet gear for traction applications," presented at the Energy Convers. Congr. Expo. (ECCE 2012), 2012.

[52]   T. V. Frandsen, L. Mathe, N. I. Berg, R. K. Holm, T. N. Matzen, P. O.Rasmussen, and K. K. Jensen, "Motor integrated permanent magnet gear in a battery electrical vehicle " presented at the Energy Convers. Congr. Expo. (ECCE 2013), 2013.

[53]   T. V. Frandsen and P. O. Rasmussen, "Loss investigation of motor integrated permanent magnet gear," presented at the Elec. Mach. Syst. (ICEMS 2014), IEEE Int. Conf., 2014.

[54]   T. V. Frandsen and P. O. Rasmussen, "Slip torque investigation and magnetic redesign of motor integrated permanent magnet gear " presented at the Elec.Mach. Syst. (ICEMS 2015), IEEE Int. Conf, 2015.

[55]   S. Gerber and R. J. Wang, "Analysis of the end-effects in magnetic gears and magnetically geared machines," presented at the Elec. Mach. Syst. (ICEMS 2014),IEEE Int. Conf., 2014.

[56]   C. T. Liu, H. Y. Chung, and C. C. Hwang, "Design assessments of a magnetic-geared double-rotor permanent magnet generator " presented at the IEEE Trans.Magn.

[57]   J. Wang and K. Atallah, "Modeling and control of 'pseudo' direct-drive brushless permanent magnet machines," presented at the Electr. Mach. Drives (IEMDC 2009), IEEE Int. Conf, 2009.

[58]   E. K. Hussain, K. Atallah, M. O. R. S. Dragan, R. E. Clark, and M. S. Sheffield, "Pseudo direct drive electrical machines for flight control surface actuation," presented at the Power Electron. Mach. Drives (PEMD 2016), IEEE Int. Conf. on, Apr. 2016. , 2016.

[59]   L. L. Wang, J. X. Shen, and M. J. Jin, "Design of a multi-power-terminals permanent magnet machine with magnetic field modulation," presented at the Elec.Mach. Syst. (ICEMS 2011), IEEE Int. Conf, 2011.

[60]   L. Jian, W. Gong, G. Xu, J. Liang, and W. Zhao, "Integrated magnetic-geared machine with sandwiched armature stator for low-speed large-torque applications," presented at the IEEE Trans. Magn., 2012.

[61]   P. M. Tlali, S. Gerber, and R. J. Wang, "Optimal design of an outer-stator magnetically geared permanent magnet machine," presented at the IEEE Trans. Magn, 2016.

[62]   D. J. Evans and Z. Q. Zhu, "Optimal torque matching of a magnetic gear within a permanent magnet machine," presented at the Electr. Mach. Drives (IEMDC 2011), IEEE Int. Conf., 2011.

[63]   S. L. Ho, S. Niu, and W. N. Fu, "Transient analysis of a magnetic gear integrated brushless permanent magnet machine using circuit-field-motion coupled time-stepping finite element method," presented at the IEEE Trans. Magn, 2010.

[64]   L. L. Wang, J. X. Shen, Y. Wang, and K. Wang, "A novel magnetic-geared outer-rotor permanent-magnet brushless motor," presented at the Power Electron. Mach. Drives (PEMD 2008), IEEE Int. Conf, 2008.

[65]   L. L. Wang, J. X. Shen, P. C. K. Luk, W. Z. Fei, C. F. Wang, and H. Hao, "Development of a magnetic-geared permanent-magnet brushless motor," presented at the IEEE Trans. Magn, 2009.

[66]   Y. Fan, H. Jiang, M. Cheng, and Y. Wang, "An improved magnetic-geared permanent magnet in-wheel motor for electric vehicles," presented at the Vehicle Power Propulsion (VPPC 2010), IEEE Int. Conf, 2010.

[67]   P. Zheng, J. Bai, C. Tong, J. Lin, and H. Wang, "Research on electromagnetic performance of a novel radial magnetic-field-modulated brushless double-rotor machine," presented at the Elec. Mach. Syst. (ICEMS 2011) IEEE Int. Conf, 2011.

[68]   J. M. Crider and S. D. Sudhoff, "An inner rotor flux-modulated permanent magnet synchronous machine for low-speed high-torque applications," presented at the IEEE Trans. Energy Convers., vol. 30, no. 3, pp., 2015.

[69]   Y. Fan, X. Han, Z. Xue, and H. Jiang, "Design, analysis and control of a permanent magnet in-wheel motor based on magnetic-gear for electric vehicle," presented at the Elec. Mach. Syst. (ICEMS 2011), IEEE Int. Conf, 2011.

[70]   P. Zheng, J. Bai, C. Tong, Y. Sui, Z. Song, and Q. Zhao, "Investigation of a novel radial magnetic-field-modulated brushless double-rotor machine used for HEVs," presented at the IEEE Trans. Magn, 2013.

[71]   J. Bai, P. Zheng, C. Tong, Z. Song, and Q. Zhao, "Characteristic analysis and verification of the magnetic-field-modulated brushless double-rotor machine," presented at the IEEE Trans. Ind. Electron., 2015.

[72]   L. Sun, M. Cheng, and H. Jia, "Analysis of a novel magnetic-geared dual-rotor motor with complementary structure," presented at the IEEE Trans. Ind.Electron, 2015.

[73]   L. Sun, M. Cheng, J. Zhang, and L. Song, "Analysis and control of complementary magnetic-geared dual-rotor motor," presented at the IEEE Trans. Ind.Electron, 2016.

[74] L. Sun, M. Cheng, H. Wen, and L. Song, "Motion control and performance evaluation of a magnetic-geared dual-rotor motor in hybrid powertrain," presented at the IEEE Trans. Ind. Electron, 2017.

[75] L. Sun, M. Cheng, and M. Tong, "Key issues in design and manufacture of magnetic-geared dual-rotor motor for hybrid vehicles," presented at the IEEE Trans.Energy Convers, 2017.

[76] Y. Wang, S. L. Ho, W. N. Fu, and J. X. Shen, "A novel brushless doubly fed generator for wind power generation," presented at the IEEE Trans. Magn, 2012.

[77] Y. Chen, W. N. Fu, and X. Weng, "A concept of general flux-modulated electric machines based on a unified theory and its application to developing a novel doubly-fed dual-stator motor.," presented at the IEEE Trans. Ind.Electron, 2017.

[78] Z. Q. Zhu and D. Evans, "Overview of recent advances in innovative electrical machines-with particular reference to magnetically geared switched flux machines " presented at the Elec. Mach. Syst. (ICEMS 2014), IEEE Int.Conf., 2014.

[79] Z. Q. Zhu, Z. Z. Wu, D. Evans, and W. Q. Chu, "Novel electrical machines having separate PM excitation stator," presented at the IEEE Trans. Magn., vol., 2015.

[80] Z. Z. Wu and Z. Q. Zhu, "Partitioned stator flux reversal machine with consequent-pole PM stator," presented at the IEEE Trans. Energy Convers, 2015.

[81] Z. Z. Wu, Z. Q. Zhu, and J. T. Shi, "Novel doubly salient permanent magnet machines with partitioned stator and iron pieces rotor," presented at the IEEE Trans. Magn, 2015.

[82] Z. Q. Zhu, H. Hua, D. Wu, J. T. Shi, and Z. Z. Wu, "Comparative study of partitioned stator machines with different PM excitation," presented at the IEEE Trans.Ind. Appl., 2016.

[83] Z. Z. Wu, Z. Q. Zhu, and H. L. Zhan, "Comparative analysis of partitioned stator flux comparative analysis of partitioned stator flux reversal PM machines having fractional-slot nonoverlapping and integer-slot overlapping windings," presented at the IEEE Trans. Energy Convers, 2016.

[84] Z. Z. Wu and Z. Q. Zhu, "Analysis of magnetic gearing effect in partitioned stator switched flux PM machine," presented at the IEEE Trans. Energy Convers, 2016.

[85] C. C. Awah, Z. Q. Zhu, Z. Z. Wu, H. L. Zhan, J. T. Shi, D. Wu, and X. Ge, "Comparison of partitioned stator switched flux permanent magnet machines having single- or double-layer winding," presented at the IEEE Trans. Magn, 2016.

[86] D. J. Evans, Z. Q. Zhu, H. L. Zhan, Z. Z. Wu, and X. Ge, "Flux-weakening control performance of partitioned stator switched flux PM machines," presented at the IEEE Trans. Ind. Appl, 2016.

[87] Z. Q. Zhu, Z. Z. Wu, D. J. Evans, and W. Q. Chu, "A wound field switched flux machine with field and armature windings separately wound in double stators," presented at the IEEE Trans. Energy Convers, 2015.

[88]   Z. Q. Zhu, Z. Z. Wu, and X. Liu, "A partitioned stator variable flux reluctance machine," presented at the IEEE Trans. Energy Convers., 2016.

[89]   H. Hua and Z. Q. Zhu, "Novel hybrid excited switched flux machine having separate field winding stator," presented at the IEEE Trans. Magn, 2016.

[90]   K. T. Chau, Z. Dong, J. Z. Jiang, L. Chunhua, and Z. Yuejin, "Design of a magnetic-geared outer-rotor permanent-magnet brushless motor for electric vehicles " presented at the IEEE Trans. Magn, 2007.

[91]   J. Pritchard, P. Padmanathan, and J. Z. Bird, "Designing a Continuously Variable Magnetic Gear," presented at the PEMD 2016, 8th IET International Conference, Glasgow,UK, 2016.

[92]   N. Bianchi and M. D. Pre, "Use of the star of slots in designing fractional-slot single-layer synchronous motors," presented at the IEE Proc. - Electr. Power Appl, 2006.

[93]   Resistance and Resistivity. Available: https://opentextbc.ca/physicstestbook2/chapter/resistance-and-resistivity/

[94]   S. I. Shahl. ELECTRICAL MACHINES II Available: https://uotechnology.edu.iq/dep-eee/lectures/3rd/Electrical/Machines%202/I_Introduction.pdf

[95]   K. Weltner, W. J. Weber, J. Grosjean, and P. Schuste, *Mathematics for Physicists and Engineers*: Springer, 2009.

[96]   *Fourier Series*. Available: https://brilliant.org/wiki/fourier-series/

[97]   B. D. Hibbs and D. X. Phan, "Flux Concentrator for ironless motors," USA Patent US 2010/0181858 A1, Jul. 22 2010.

[98]   W. N. Fu and L. Li, "Optimal Design of Magnetic Gears With a General Pattern of Permanent Magnet Arrangement," *IEEE Trans. Applied Super.,* vol. 26, pp. 1-5, 2016.

[99]   A. Toyota, T. Shikayama, and M. Kakihara, "Periodic magnetic field generation device, and linear motor and rotary motor using the same," USA Patent US 2011/0012440 A1, Jan 20 2011.

[100]   K. Uppalapati, K. J., J. Wright, L. K., J. Z. Bird, and W. Williams, "A low assembly cost coaxial magnetic gearbox," presented at the South. Power Elec. Conf., Auckland, NZ, Dec 5-8, 2016.

[101]   H. Huang, D. Li, W. Kong, and R. Ku, "Torque Performance of Pseudo Direct-drive Machine with Halbach Consequent Pole," presented at the 2018 IEEE Energy Conversion Congress and Exposition (ECCE), 2018.

[102]   A. Penzkofer and K. Atallah, "Analytical Modeling and Optimization of Pseudo-Direct Drive Permanent Magnet Machines for Large Wind Turbines," presented at the IEEE Transactions on Magnetics 2015.

[103]   G. Cooke and K. Atallah, "Pseudo direct drive electrical machines with alternative winding configurations," presented at the IEEE Transactions on Magnetics, 2017.

[104]   X. Zhang, X. Liu, Y. Zhao, and Z. Chen, "A Novel Magnetic-Geared Machine with Dual Flux Modulators," presented at the IECON 2018 - 44th Annual Conference of the IEEE Industrial Electronics Society, Washington, DC, USA, 2018.

[105]   *Even and Odd Functions*. Available: https://ocw.mit.edu/courses/mathematics/18-03sc-differential-equations-fall-2011/unit-iii-fourier-series-and-laplace-transform/operations-on-fourier-series/MIT18_03SCF11_s22_2text.pdf